

# N-rich electron acceptors: triplet harvesting in multichromophoric pyridoquinoxaline and pyridopyrazine-based organic emitters

Bahadur Sk,<sup>a</sup> Samarth Sharma,<sup>a</sup> Anto James,<sup>a,b</sup> Subhankar Kundu,<sup>a</sup> and Abhijit Patra\*<sup>a</sup>

<sup>a</sup>Department of Chemistry, Indian Institute of Science Education and Research Bhopal, Bhopal Bypass Road, Bhauri, Bhopal 462066, Madhya Pradesh, India

<sup>b</sup>Department of Chemistry, Indian Institute of Science Education and Research Thiruvananthapuram, Maruthamala PO, Vithura, Kerala 695551, India

[abhijit@iiserb.ac.in](mailto:abhijit@iiserb.ac.in)

## Contents

|   |     |
|---|-----|
| I. Materials and Methods  | S1  |
| 1.1 Chemicals:  | S1  |
| 1.2 Instrumentation:  | S1  |
| II. Design Strategy   | S3  |
| III. Synthesis and Characterization   | S6  |
| 3.1 Synthesis of precursor compounds:   | S6  |
| 3.2 Synthesis of donor-acceptor compounds:                                      | S8  |
| IV. Spectroscopic characterization  | S12 |
| 4.1 Electronic absorption:  | S12 |
| 4.2 Absorption analysis:  | S13 |
| 4.3 Electronic Emission:  | S14 |
| 4.4 Lippert-Mataga plot:  | S16 |
| 4.5 Fluorescence quantum yield and time-resolved spectroscopy:                  | S18 |
| 4.6 Spectroscopic data table:   | S19 |
| V. Time resolved Emission Spectra (TRES): LE vs. ICT                            | S20 |
| VI. Low-temperature emission measurements                                       | S22 |
| 6.1 Steady-state emission spectra:  | S22 |
| 6.2 Phosphorescence Spectra:  | S24 |
| 6.3 Experimental calculation of singlet-triplet energy gap ( $\Delta E_{ST}$ ): | S24 |
| VII. Delayed Fluorescence   | S26 |
| 7.1 Delayed fluorescence in degassed toluene:                                   | S26 |
| 7.2 Oxygen free condition: The delayed-to-prompt fluorescence ratio:            | S27 |
| VIII. Film Photophysics   | S28 |
| 8.1 Steady-state and time-resolved spectroscopy:                                | S28 |
| IX. Laser power dependent study   | S33 |
| X. Temperature-dependent decay  | S35 |
| XI. Computational investigations  | S37 |
| 11.1 TDDFT Calculations:  | S37 |
| 11.2 Dihedral angles:   | S39 |
| 11.3 Singlet-triplet energy gap ( $\Delta E_{ST}$ ):                            | S41 |
| XII. Crystal structure analysis   | S46 |
| XIII. Security Encryption   | S49 |
| XIV. Summary  | S50 |
| XV. References  | S51 |
| XVI. Characterization: <sup>1</sup> H, <sup>13</sup> C NMR and Mass Spectra     | S54 |

# I. Materials and Methods

## 1.1 Chemicals:

All chemicals were used as received unless otherwise stated. 9,10-phenanthrenequinone (99%), 4,4'-dibromobenzil (90%), 2,3-diamino-5-bromopyridine (97%), *N*-bromosuccinimide (99%), palladium(II) acetate (99.9%), carbazole (99%), phenoxazine (99%), tris(dibenzylideneacetone) dipalladium(0) (99%), X-Phos (99%), potassium tert-butoxide (99%), dimethyl sulfoxide (99%) and toluene (99.85%) were received from Sigma-Aldrich. Sodium hydroxide (99%), potassium carbonate, acetic acid, concentrated sulphuric acid, 1,4-dioxane, chloroform, and hexane were received from Merck. bromine (99%), THF (99%), ethanol (99.8%) from Spectrochem, Tri-tert-butylphosphine (96%) was received from Alfa aesar.

## 1.2 Instrumentation:

**NMR Spectroscopy:**  $^1\text{H}$  and  $^{13}\text{C}$ -NMR spectra were recorded on Bruker Avance III 500 and 700 MHz NMR spectrometer and the chemical shifts ( $\delta$ ) are reported in parts per million (ppm) using residual solvent signals as internal standards.

**High-resolution mass spectrometry (HRMS):** High-resolution mass spectrometry (HRMS) data were obtained on Bruker MicrOTOF-Q-II mass spectrometer instrument. Chloroform was used as the solvent.

**Matrix-Assisted Laser Desorption Ionization (MALDI-ToF):** Matrix-assisted laser desorption ionization-time of flight mass spectrometry was performed with Bruker Daltonics UltrafleXtreme, using software flex Control version 3.4.

**Melting point measurements:** Melting points of the D<sub>3</sub>-A compounds were measured using Digital Melting Point Apparatus (Jyoti: AN ISO: 9001:2000, India). Compounds were loaded in the capillary glass tubes.

**Steady-state absorption spectroscopy:** The UV-Vis absorption spectra were recorded on a Cary 100 spectrophotometer.

**Diffuse Reflectance UV-Vis Spectroscopy (DR UV-Vis):** DR UV-Vis spectra were recorded using an Agilent Cary 100 spectrometer equipped with a diffuse reflectance integrating sphere attachment (DRA).

**Steady-state fluorescence spectroscopy:** Steady-state fluorescence measurements were carried out on a Jobin Yvon Horiba Model Fluorolog-3-21.

**Time-resolved fluorescence Spectroscopy:** Time-resolved fluorescence measurements were carried out using time-correlated single-photon counting (TCSPC) spectrometer (Delta Flex-01-DD/HORIBA). Delta diode laser 410, 440, and 468 nm were used as the excitation source. The SpectraLED 417 and 461 nm light source directly connected with DeltaHub was used for the measurement of delayed fluorescence and phosphorescence lifetimes. Picosecond photon detection module with photomultiplier tube (PMT) was used as a detector. The instrument response function was recorded by using an aqueous solution of Ludox. Decay curves were analyzed by nonlinear least-squares iteration using Horiba EzTime decay analysis software. The quality of the fit was assessed by the fitting parameters ( $\chi^2$ ) as well as the visual inspection of the residuals. Time-resolved emission spectra (TRES) were recorded using 468 nm diode

laser and 461 nm SpectraLED. The emission spectra were collected at different delay times with the wavelength range from 480 to 800 nm at 5 nm interval.

**Excited-state decay kinetics:** The laser power-dependent emission spectra and decays were measured with LP980 laser flash-photolysis spectrometer (Edinburgh Instruments, UK). The emission decay and time gated spectra were recorded by inserting samples ( $1.5 \times 5$  cm D<sub>3</sub>-A compounds doped PMMA thin films on quartz plates) at a 30°-45° angle into a film sample holder. The samples were purged 15 min with N<sub>2</sub> before measurement. The samples were excited with a nanosecond pulsed laser (Opolette™ nanosecond pulsed laser, OPOTEK, USA) combined with wavelength tunable OPO crystal (410-2400 nm) integrated into Edinburgh LP980 laser flash photolysis spectrometer system. White light probe pulses generated by a pulsed 150 W Xe lamp were passed through the sample, focused into the spectrometer, then detected by intensified Andor iStar CCD camera and PMT. The signal was digitized with a Tektronix TDS3012C oscilloscope, and the data were analysed with LP900 software. Single wavelength kinetic data were the result of averaging 10 laser shots.

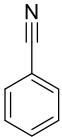
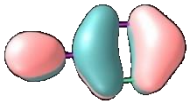
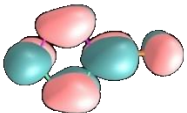
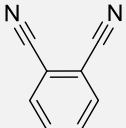
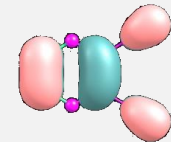
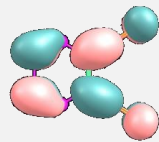
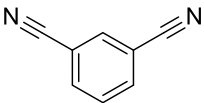
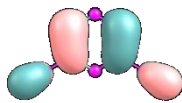
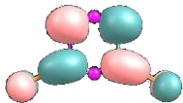
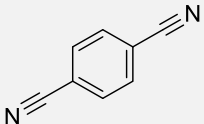
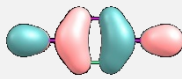
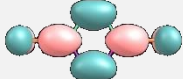
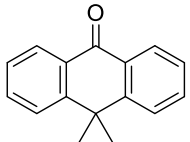
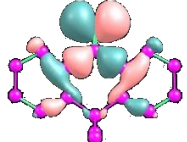
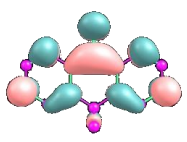
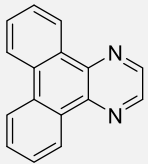
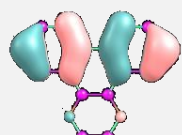
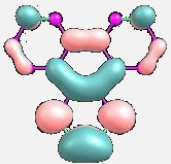
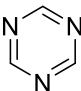
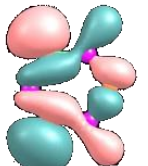
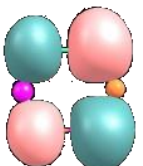
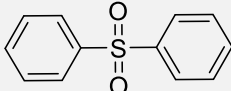
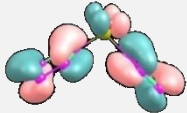

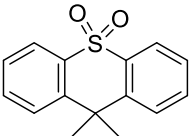
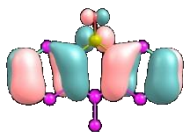
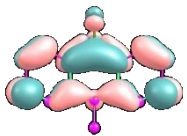
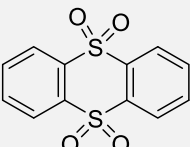
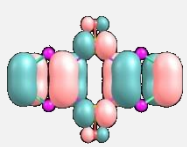
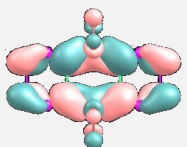
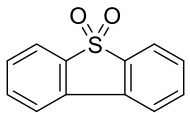
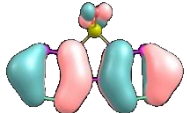
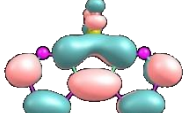
## II. Design Strategy

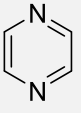
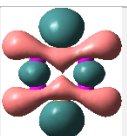
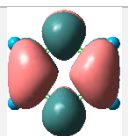
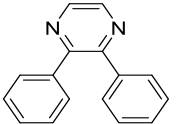
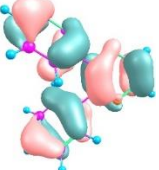
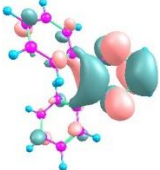
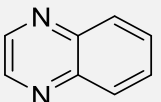
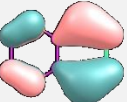
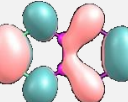
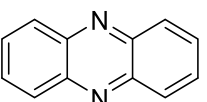
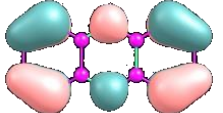
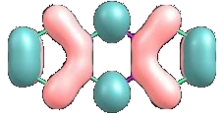
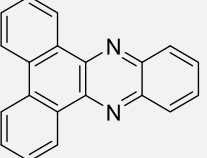
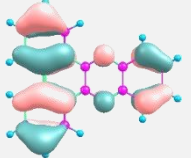
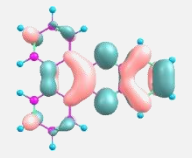
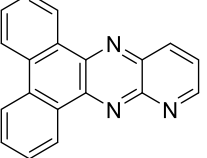
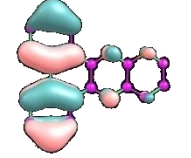
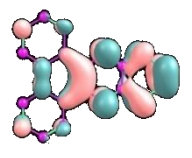
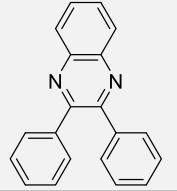
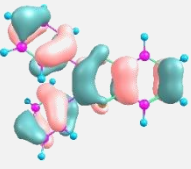
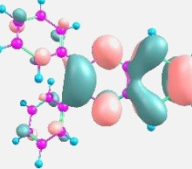
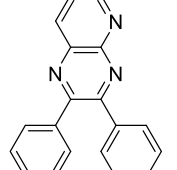
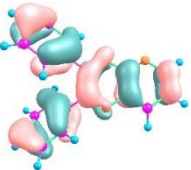
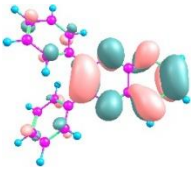
The intramolecular charge transfer (ICT) from the donor (D) to the acceptor (A) in the excited state is crucial for triplet harvesting by thermally activated delayed fluorescence (TADF) and/ or room temperature phosphorescence (RTP). A suitable D-A pair is essential for tuning the charge transfer to achieve the TADF or RTP. The presence of multiple electron-withdrawing cyano or imine groups on a phenyl ring leads to a strong acceptor unit. 4-(dimethylamino)benzotrile (DMABN) having a single cyano group is the most studied D-A molecule for charge transfer. Adachi and coworkers reported ICT molecules based on dicyanobenzene, a relatively stronger electron-withdrawing acceptor unit for highly efficient TADF emission.<sup>1</sup> Bryce and coworkers studied the effect of molecular geometry for the tuning of TADF and RTP emission based on benzophenone,<sup>2,3</sup> 9,9-dimethyl-9H-thioxanthene 10,10-dioxide,<sup>4</sup> and dibenzothiophene-5,5-dioxide,<sup>5-7</sup> containing acceptor units. Xie *et al.* reported delayed emission with high quantum efficiency in the red region ( $\lambda_{em} = 600$  nm) with rigid planar dibenzo[*a,c*]phenazine as the acceptor core.<sup>8</sup> TADF active dibenzo[*a,c*]phenazine-11,12-dicarbonitrile based D-A materials with red and near-infrared electroluminescent characteristics were reported by several groups.<sup>9,10</sup> Quinoxaline based D-A-D molecules for dual mechanochromism was reported by Grazulevicius and coworkers.<sup>11</sup> Jiang and coworkers reported RTP and TADF emitters based on diphenylquinoxaline acceptor units.<sup>12</sup>

Phenazine and quinoxaline-based D-A architectures are well explored in optoelectronics.<sup>12-16</sup> But, their application is limited due to the low charge transfer efficiency.<sup>9</sup> To augment the electron-withdrawing capabilities in comparison to quinoxaline and phenazine, incorporation of an additional nitrogen-containing heterocycle to the quinoxaline unit is a facile alternative. Herein, we describe N-rich dibenzo[*f,h*]pyrido[2,3-*b*]quinoxaline (PQ) and 2,3-diphenylpyrido[2,3-*b*]pyrazine (PZ) as novel acceptor units and a versatile design platform to construct a series of fascinating D-A compounds. Both the acceptor cores have better electron-withdrawing abilities due to the presence of the multiple numbers of electronegative nitrogen atoms (Fig. 1a). The difference between PQ and PZ core is in the  $\pi$ -spacer groups.

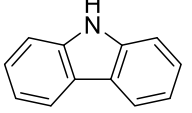
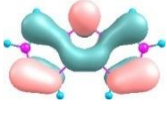
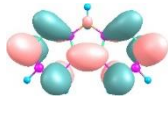
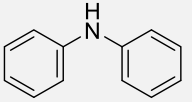
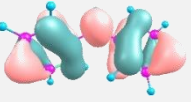
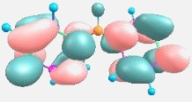
The computational calculations of the HOMO/LUMO distribution and HOMO/LUMO levels of various reported donor and acceptor units are shown in Fig. 1a and Table S1, S2. The calculations were carried out using the density functional theory (DFT) with B3LYP 6-31G (d,p) basis set in the Gaussian 09W program package.<sup>9,17</sup> The electron-donating capability of the donor cores were estimated from the electronic distribution of the HOMO.<sup>17</sup> The LUMO levels of the acceptors reflect the electron-accepting characters.<sup>17</sup> Phenoxazine and phenothiazine are the known examples of the strong donor moieties, whereas carbazole is a comparatively weaker donor.<sup>17</sup> On the other hand, PQ and PZ are the stronger acceptor units as compared to that of the other commonly used acceptors depicted in Fig. 1a. Thus, we choose weak carbazole and strong phenoxazine donor to construct a series of new D<sub>3</sub>-A compounds for the tuning of the charge transfer based on rigid PQ and flexible PZ acceptor cores.

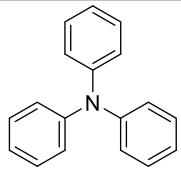
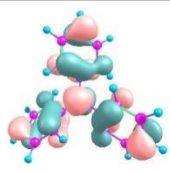
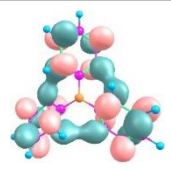
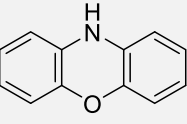
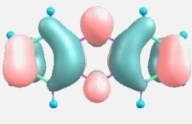
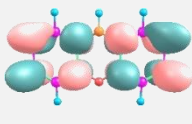
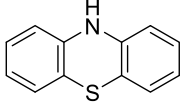
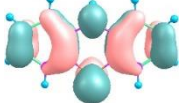
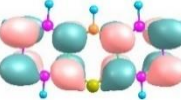
**Table S1** HOMO-LUMO distribution and energy values of various acceptor units used for the triplet harvesting, estimated by DFT at the B3LYP/6-31G(d,p) level.

| Sl. No | Structure   | MOs   |  | Energy (- eV) |      |
|--------|---|---|--|---------------|------|
|        |   | HOMO  | LUMO   | HOMO          | LUMO |
| 1      |    |    |    | 7.27          | 1.42 |
| 2      |    |    |    | 7.77          | 2.36 |
| 3      |    |    |    | 7.84          | 2.25 |
| 4      |    |    |    | 7.74          | 2.54 |
| 5      |   |   |   | 6.62          | 1.75 |
| 6      |  |  |  | 6.15          | 1.74 |
| 7      |  |  |  | 7.60          | 1.59 |
| 8      |  |  |  | 7.12          | 1.38 |
| 9      |  |  |  | 7.04          | 1.27 |
| 10     |  |  |  | 7.73          | 2.26 |
| 11     |  |  |  | 6.67          | 1.82 |

|                |   |   |  |      |      |
|----------------|---|---|--|------|------|
| 12             |    |    |    | 6.82 | 1.43 |
| 13             |    |    |    | 6.06 | 1.38 |
| 14             |    |    |    | 6.71 | 1.94 |
| 15             |    |    |    | 6.09 | 2.42 |
| 16             |    |    |    | 6.03 | 2.21 |
| This work (PQ) |   |   |   | 6.18 | 2.46 |
| 17             |  |  |  | 6.07 | 1.90 |
| This work (PZ) |  |  |  | 6.18 | 2.18 |

**Table S2** Comparison of the intrinsic electron-donating capability (HOMO level) of various donor units used for the triplet harvesting, estimated by DFT at the B3LYP/6-31G(d,p) level.

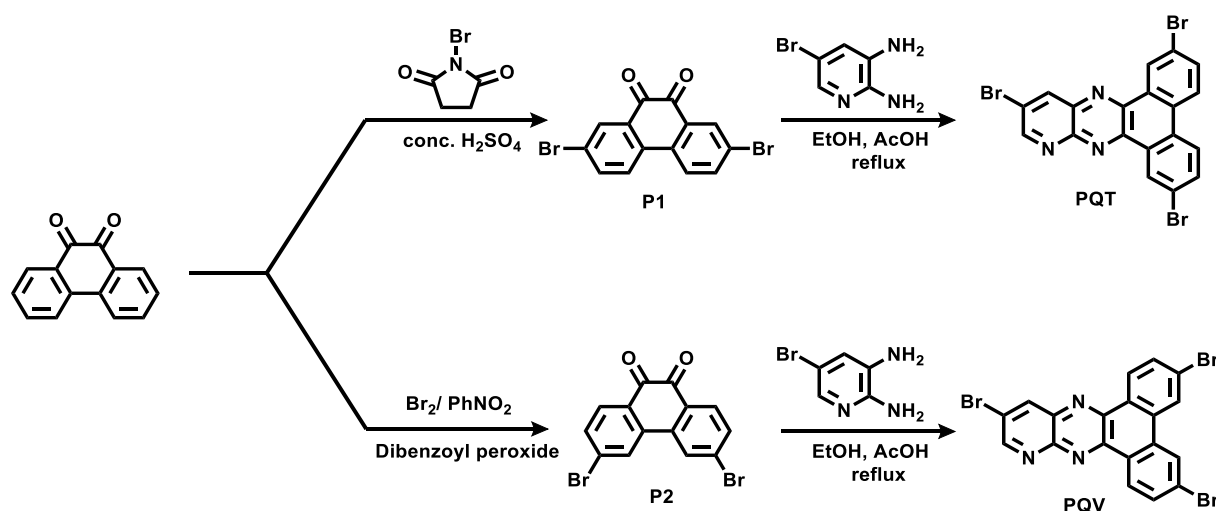
| Sl. No         | Structure   | MOs   |  | Energy (- eV) |      |
|----------------|---|---|--|---------------|------|
|                |   | HOMO  | LUMO   | HOMO          | LUMO |
| This work (Cz) |  |  |  | 5.46          | 0.66 |
| 2 (DPA)        |  |  |  | 5.09          | 0.14 |

|                   |   |   |  |      |      |
|-------------------|---|---|--|------|------|
| 3 (TPA)           |  |  |  | 4.95 | 0.32 |
| This work<br>(PO) |  |  |  | 4.69 | 0.24 |
| 5 (PS)            |  |  |  | 4.68 | 0.45 |

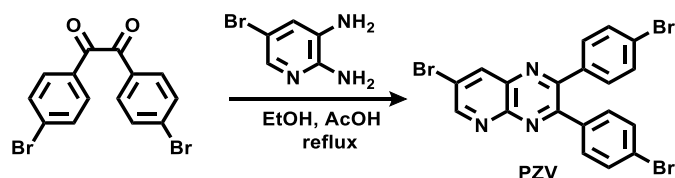
### III. Synthesis and Characterization

#### 3.1 Synthesis of precursor compounds:

Pyridoquinoxaline (PQ) and pyridopyrazine (PZ) based precursor compounds were synthesized following reported procedures with minor modifications.<sup>18</sup> The bromination of phenanthraquinone at 2,7 and 3,6-positions resulted in 2,7-dibromophenanthrene-9,10-dione (**P1**) and 3,6-dibromophenanthrene-9,10-dione (**P2**). Further, Schiff-base condensation of **P1** and **P2** with 5-bromopyridine-2,3-diamine yielded derivatives of 2,7,12-tribromodibenzo[*f,h*]pyrido[2,3-*b*]quinoxaline (**PQT**) and 3,6,12-tribromodibenzo[*f,h*]pyrido[2,3-*b*]quinoxaline (**PQV**) as the central acceptor cores (Scheme S1). The pyridopyrazine core (**PZV**) was synthesized by Schiff base condensation between 1,2-bis(4-bromophenyl)ethane-1,2-dione and 5-bromopyridine-2,3-diamine following a similar synthetic protocol (Scheme S2).



**Scheme S1** Synthetic routes of 2,7,12-tribromodibenzo[*f,h*]pyrido[2,3-*b*]quinoxaline (PQT) and 3,6,12-tribromodibenzo[*f,h*]pyrido[2,3-*b*]quinoxaline (PQV).



**Scheme S2** Synthetic route for 7-bromo-2,3-bis(4-bromophenyl)pyrido[2,3-*b*]pyrazine (PZV).

**Synthesis of 2,7-dibromophenanthrene-9,10-dione (P1):** To a solution of phenanthrene-9,10-dione (500 mg, 1 eqv.) in 98% H<sub>2</sub>SO<sub>4</sub>, *N*-bromosuccinimide (1 g, 2.5 eqv.) was added while stirring. The stirring was continued for 3 h at room temperature. Subsequently, the reaction mixture was poured onto crushed ice to quench the unreacted acid as well as precipitation of the desired product. The orange product was filtered off, washed with cold water, and recrystallized in DMSO to obtain 2,7-dibromophenanthrene-9,10-dione with yield 72% (Scheme S1).

<sup>1</sup>H NMR (500 MHz in DMSO-*d*<sub>6</sub>, δ<sub>H</sub>): 8.26 (2 H, d, *J* = 8.5 Hz), 8.09 (2 H, d, *J* = 2.3 Hz), 7.97 (2 H, dd, *J* = 8.5, 2.3 Hz). <sup>13</sup>C NMR (176 MHz in DMSO-*d*<sub>6</sub>, δ<sub>C</sub>): 177.24, 137.86, 134.05, 133.62, 131.47, 127.38, 123.29.

**Synthesis of 3,6-dibromophenanthrene-9,10-dione (P2):** A mixture of (1g, 1 eqv.) of 9,10-phenanthrenequinone, (94 mg, 0.08 eqv.) dibenzoyl peroxide and 0.1 mL bromine in 20 mL nitrobenzene was refluxed at 130 °C. After initiation of the reaction additional 0.45 mL of bromine was added dropwise. The reaction mixture was stirred for 6 h at 130 °C and then was allowed to cool to room temperature. The product precipitated out upon addition of hexane. After filtration and washing with copious amounts of hexane, 3,6-dibromophenanthrene-9,10-quinone was obtained as dark yellow solid (P2) with yield of 65% (Scheme S1).

<sup>1</sup>H NMR (500 MHz, CDCl<sub>3</sub>, δ<sub>H</sub>): 8.12 (1 H, d, *J* = 1.9 Hz), 8.07 (1 H, dd, *J* = 8.2, 1.4 Hz), 7.69 – 7.65 (1 H, m). <sup>13</sup>C NMR (126 MHz, CDCl<sub>3</sub>, δ): 178.75, 135.83, 133.33, 132.00, 131.99, 129.75, 127.29.

**Synthesis of 2,7,12-tribromodibenzo[*f,h*]pyrido[2,3-*b*]quinoxaline (PQT):** P1 (200 mg, 1 eqv.) and 5-bromopyridine-2,3-diamine (122 mg, 1.2 eqv.) were dissolved in 20 mL ethanol. After a while, 5-6 drops of acetic acid were added to the reaction mixture while stirring. The mixture was refluxed for 90 min at 78 °C. The reaction mixture was brought to room temperature, and filtration followed by washing with ethanol afforded the product 2,7,12-tribromodibenzo[*f,h*]pyrido[2,3-*b*]quinoxaline as a pale yellowish solid with yield 85% (Scheme S1).

<sup>1</sup>H NMR (500 MHz in CDCl<sub>3</sub>, δ<sub>H</sub>): 9.56 (1 H, d, *J* = 2.3 Hz), 9.32 (2 H, m), 8.84 (1 H, dd, *J* = 2.5, 1.3 Hz), 8.32 (2 H, m), 7.93 – 7.87 (2 H, m). Due to the low solubility of PQT in common deuterated organic solvents, <sup>13</sup>C NMR characterization was not possible. HRMS (APCI): [M+H]<sup>+</sup> (m/z) calculated for C<sub>19</sub>H<sub>8</sub>Br<sub>3</sub>N<sub>3</sub>: 517.8248; found: 517.8300.

**Synthesis of 3,6,12-tribromodibenzo[*f,h*]pyrido[2,3-*b*]quinoxaline (PQV):** P2 (200 mg, 1 eqv.) and 5-bromopyridine-2,3-diamine (122 mg, 1.2 eqv.) were dissolved in 20 mL ethanol. Then 5-6 drops of acetic acid were added to the reaction mixture while stirring. The mixture was refluxed for 90 min at 78 °C. The reaction mixture was brought to room temperature, and filtration followed by washing with ethanol



afforded the product 3,6,12-tribromodibenzo[*f,h*]pyrido[2,3-*b*]quinoxaline as a yellowish solid with yield 85% (Scheme S1).

**<sup>1</sup>H NMR (700 MHz in CDCl<sub>3</sub>, δ<sub>H</sub>):** 9.37 (1 H, d, *J* = 8.6 Hz), 9.30 (1 H, d, *J* = 2.5 Hz), 9.19 (1 H, d, *J* = 8.6 Hz), 8.86 (1 H, d, *J* = 2.4 Hz), 8.64 (2 H, m), 7.92 (2 H, m). Due to the low solubility of **PQV** in common deuterated organic solvents, <sup>13</sup>C NMR characterization was not possible. **HRMS (APCI):** [M+H]<sup>+</sup> (m/z) calculated for C<sub>19</sub>H<sub>8</sub>Br<sub>3</sub>N<sub>3</sub>: 517.8248; found: 517.8359.

**Synthesis of 7-bromo-2,3-bis(4-bromophenyl)pyrido[2,3-*b*]pyrazine (PZV):** 1,2-bis(4-bromophenyl)ethane-1,2-dione (200 mg, 1 eqv.) and 5-bromopyridine-2,3-diamine (122 mg, 1.2 eqv.) were dissolved in 20 mL ethanol. Then 5–6 drops of acetic acid were added to the reaction mixture while stirring. The mixture was refluxed for 90 min at 78 °C. The reaction mixture was brought to room temperature and filtration followed by washing with ethanol afforded the product **PZV** as a white solid with yield 80% (Scheme S2).

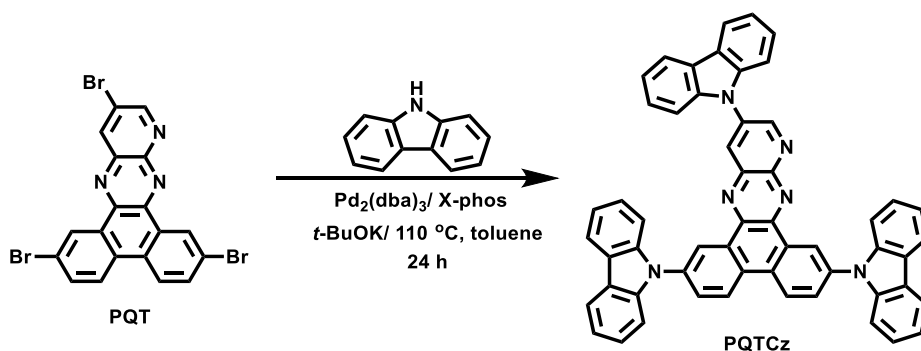
**<sup>1</sup>H NMR (500 MHz in CDCl<sub>3</sub>, δ<sub>H</sub>):** 9.17 (1 H, d, *J* = 2.4 Hz), 8.66 (1 H, d, *J* = 2.4 Hz), 7.56 – 7.48 (6 H, m), 7.45 – 7.41 (2 H, m). **<sup>13</sup>C NMR (126 MHz in CDCl<sub>3</sub>, δ<sub>C</sub>):** 155.66, 139.39, 136.69, 136.59, 136.33, 131.93, 131.77, 131.70, 131.40, 124.76, 124.61, 121.43. **HRMS (APCI):** [M+H]<sup>+</sup> (m/z) calculated for C<sub>19</sub>H<sub>10</sub>Br<sub>3</sub>N<sub>3</sub>: 519.8504; found: 519.8508.

### 3.2 Synthesis of donor-acceptor compounds:

The C-N coupling of both the precursor with the donor moieties was achieved through Pd-catalysed Buchwald-Hartwig amination reaction.<sup>18</sup> The detailed synthetic procedure is discussed below.

**Synthesis of 2,7,12-tri(9*H*-carbazol-9-yl)dibenzo[*f,h*]pyrido[2,3-*b*]quinoxaline (PQTCz):** Toluene (10 mL) was added to a mixture of 1 eqv. **PQT** (100 mg) and 3.2 eqv. carbazole, Pd<sub>2</sub>(dba)<sub>3</sub> (0.15 eqv.), *t*-BuOK (4.0 eqv.) and X-Phos (0.15 eqv.). The solution was stirred under the argon atmosphere at 110 °C for 24 h. After cooling to the room temperature, the reaction was quenched by adding 10% aqueous NaHCO<sub>3</sub> and 20 mL distilled water. The organic layer was then extracted with dichloromethane (3 x 15 mL). The collected organic products were then dried over anhydrous MgSO<sub>4</sub> and concentrated under vacuum. The residue was purified by column chromatography (hexane/DCM 1:4) in alumina gel to afford dark brown solid with a yield 62% (Scheme S3).

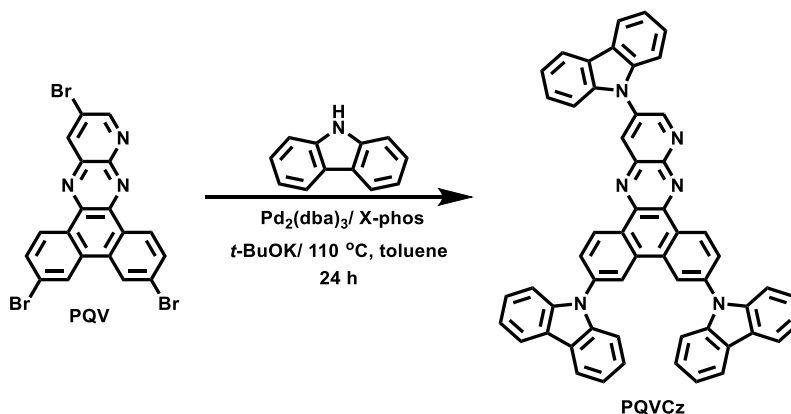
**<sup>1</sup>H NMR (500 MHz in CDCl<sub>3</sub>, δ<sub>H</sub>):** 9.86 (1 H, d, *J* = 2.2 Hz), 9.68 (1 H, d, *J* = 2.2 Hz), 9.59 (1 H, d, *J* = 2.7 Hz), 8.87 (3 H, m), 8.17 (8 H, m), 7.64 (6 H, m), 7.47 (6 H, m), 7.35 (6 H, m). **<sup>13</sup>C NMR (176 MHz in CDCl<sub>3</sub>, δ<sub>C</sub>):** 154.12, 148.33, 144.40, 143.77, 140.76, 140.08, 139.32, 138.31, 138.01, 137.97, 135.58, 132.89, 131.54, 131.16, 130.89, 130.81, 129.92, 129.80, 127.85, 126.72, 126.26, 126.22, 125.60, 125.23, 125.12, 124.78, 124.31, 123.77, 123.74, 121.54, 120.76, 120.54, 120.48, 120.45, 114.09, 109.88, 109.76, 109.38. **HRMS (APCI):** [M+H]<sup>+</sup> (m/z) calculated for C<sub>55</sub>H<sub>32</sub>N<sub>6</sub>: 777.2767; found: 777.2775. **M. Pt.:** 273 °C (decomp.).



**Scheme S3** Synthetic route of 2,7,12-tri(9*H*-carbazol-9-yl)dibenzo[*f,h*]pyrido[2,3-*b*]quinoxaline (PQTCz).

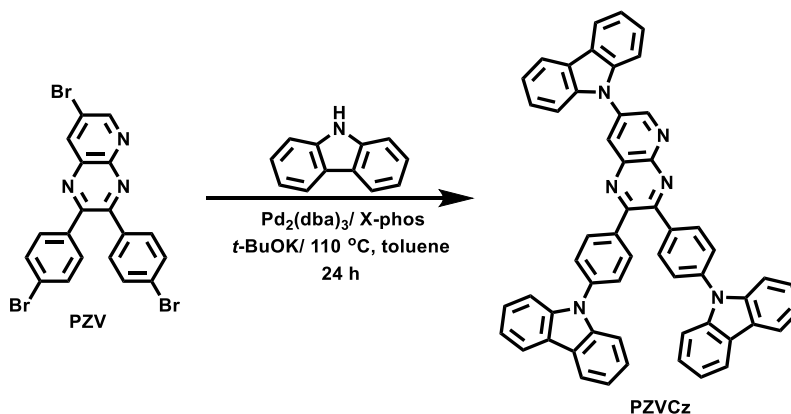
**Synthesis of 3,6,12-tri(9*H*-carbazol-9-yl)dibenzo[*f,h*]pyrido[2,3-*b*]quinoxaline (PQVCz):** A mixture of 3,6,12-tribromodibenzo[*f,h*]pyrido[2,3-*b*]quinoxaline (0.1 mmol), carbazole (0.32 mmol), tris(dibenzylideneacetone)dipalladium(0) Pd<sub>2</sub>(dba)<sub>3</sub> (0.015 mmol), potassium *tert*-butoxide *t*-BuOK (0.4 mmol) and 2-dicyclohexylphosphino-2',4',6'-triisopropylbiphenyl X-Phos (0.6 mmol) was added into 8 mL of dry toluene in a Schlenk tube. The solution was then stirred under the nitrogen atmosphere for 24 h at 110 °C temperature. The reaction was quenched by adding 20 mL distilled water after cooling to the room temperature. The organic layer was collected in dichloromethane (3 x 15 mL). The collected organic layer was then dried over anhydrous magnesium sulphate MgSO<sub>4</sub> and after the filtration concentrated under vacuum. The residue was purified through column chromatography (neutral alumina) using dichloromethane/hexane solvent mixture as eluent to obtain the desired compound **PQVCz** as a dark orange solid powder with yield 62% (Scheme S4).

**<sup>1</sup>H NMR (500 MHz in CDCl<sub>3</sub>, δ<sub>H</sub>):** 9.88 (1 H, d, *J* = 8.5 Hz), 9.71 – 9.67 (2 H, m), 8.97 (1 H, d, *J* = 2.7 Hz), 8.76 (2 H, s), 8.25 (2 H, d, *J* = 7.8 Hz), 8.17 (4 H, d, *J* = 7.8 Hz), 8.10 (2 H, m), 7.71 (2 H, d, *J* = 8.3 Hz), 7.62 (4 H, m), 7.55 (2 H, m), 7.45 (6 H, m), 7.33 (4 H, m). **<sup>13</sup>C NMR (176 MHz in CDCl<sub>3</sub>, δ<sub>C</sub>):** 153.99, 148.55, 144.51, 143.85, 141.08, 140.95, 140.45, 140.27, 137.92, 135.51, 133.61, 133.14, 129.58, 129.02, 128.69, 128.40, 127.27, 127.20, 126.77, 126.39, 126.36, 124.34, 123.90, 121.56, 121.04, 120.93, 120.86, 120.72, 120.61, 120.59, 109.69, 109.64, 109.45. **HRMS (APCI):** [M+H]<sup>+</sup> (*m/z*) calculated for C<sub>55</sub>H<sub>32</sub>N<sub>6</sub>: 777.2767; found: 777.2775. **M. Pt.:** ~ 362 °C (decomp., considering darkening of color and textural change).



**Scheme S4** Synthetic route of 3,6,12-tri(9*H*-carbazol-9-yl)dibenzo[*f,h*]pyrido[2,3-*b*]quinoxaline (PQVCz).

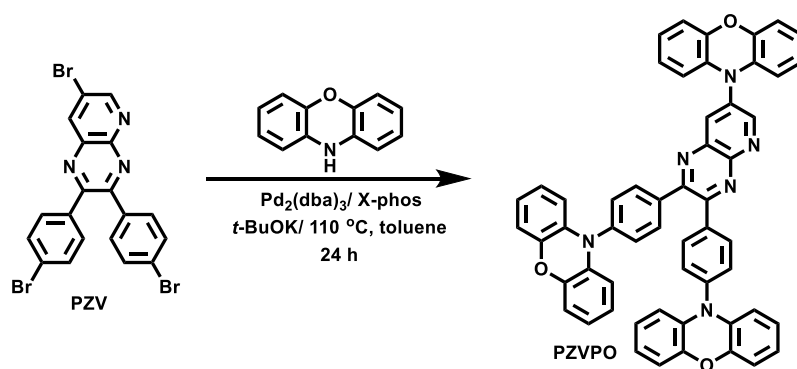
**Synthesis of 9,9'-((7-(9H-carbazol-9-yl)pyrido[2,3-*b*]pyrazine-2,3-diyl)bis(4,1-phenylene))bis(9H-carbazole) (PZVCz):** A mixture of PZV (100 mg, 1 eqv.), carbazole (3.2 eqv.), Pd<sub>2</sub>(dba)<sub>3</sub> (0.15 eqv.), *t*-BuOK (4.0 eqv.) and X-Phos (0.15 eqv.) was added in toluene (10 mL). The reaction mixture was stirred at 110 °C for 24 h under the argon atmosphere. After cooling to room temperature, the reaction was quenched by 10% aq. NaHCO<sub>3</sub> and 20 mL distilled water. The organic products were then extracted with dichloromethane (3 x 15 mL), dried over MgSO<sub>4</sub> and concentrated under vacuum. The crude product was purified by column chromatography (n-hexane/ DCM 1:1) to afford a yellow solid with yield 65% (Scheme S5). **<sup>1</sup>H NMR (500 MHz in CDCl<sub>3</sub> δ<sub>H</sub>)** 9.57 (1 H, d, *J* = 2.6 Hz), 8.83 (1 H, d, *J* = 2.6 Hz), 8.23 (2 H, d, *J* = 7.8 Hz), 8.17 (4 H, dd, *J* = 7.7, 2.5 Hz), 8.08 – 8.04 (2 H, m), 8.01 – 7.97 (2 H, m), 7.74 (4 H, m), 7.65 (2 H, d, *J* = 8.2 Hz), 7.52 (6 H, m), 7.47 – 7.40 (6 H, m), 7.33 (4 H, m). **<sup>13</sup>C NMR (176 MHz in CDCl<sub>3</sub> δ<sub>C</sub>)** 155.31, 154.65, 153.42, 148.36, 140.42, 140.17, 139.36, 139.34, 136.89, 136.71, 136.54, 135.87, 133.15, 131.98, 131.61, 126.95, 126.73, 126.67, 126.24, 124.30, 123.75, 121.53, 120.83, 120.51, 120.48, 120.46, 109.74, 109.67, 109.38. **HRMS (APCI):** [M+H]<sup>+</sup> (*m/z*) calculated for C<sub>55</sub>H<sub>34</sub>N<sub>6</sub>: 779.2845; found: 779.2898. **M. Pt.:** 355 °C (decomp., considering color change from yellow to orange).



**Scheme S5** Synthetic route of 9,9'-((7-(9H-carbazol-9-yl)pyrido[2,3-*b*]pyrazine-2,3-diyl)bis(4,1-phenylene))bis(9H-carbazole) (PZVCz).

**Synthesis of 10,10'-((7-(10H-phenoxazin-10-yl)pyrido[2,3-*b*]pyrazine-2,3-diyl)bis(4,1-phenylene))bis(10H-phenoxazine) (PZVPO):** A mixture of PZV (100 mg, 1 eqv.), phenoxazine (200 mg, 3.2 eqv.), Pd<sub>2</sub>(dba)<sub>3</sub> (0.15 eqv.), *t*-BuOK (4.0 eqv.) and X-Phos (0.15 eqv.) was added in toluene (10 mL). The reaction mixture was stirred at 110 °C for 24 h under the argon atmosphere. After cooling to room temperature, the reaction was quenched by 10% aq. NaHCO<sub>3</sub> and 20 mL distilled water. The organic residue was then extracted with dichloromethane (3 x 15 mL), dried over MgSO<sub>4</sub> and concentrated under vacuum. The crude product purified by column chromatography (n-hexane/ DCM 1:2) to afford red solid with yield 80% (Scheme S6).

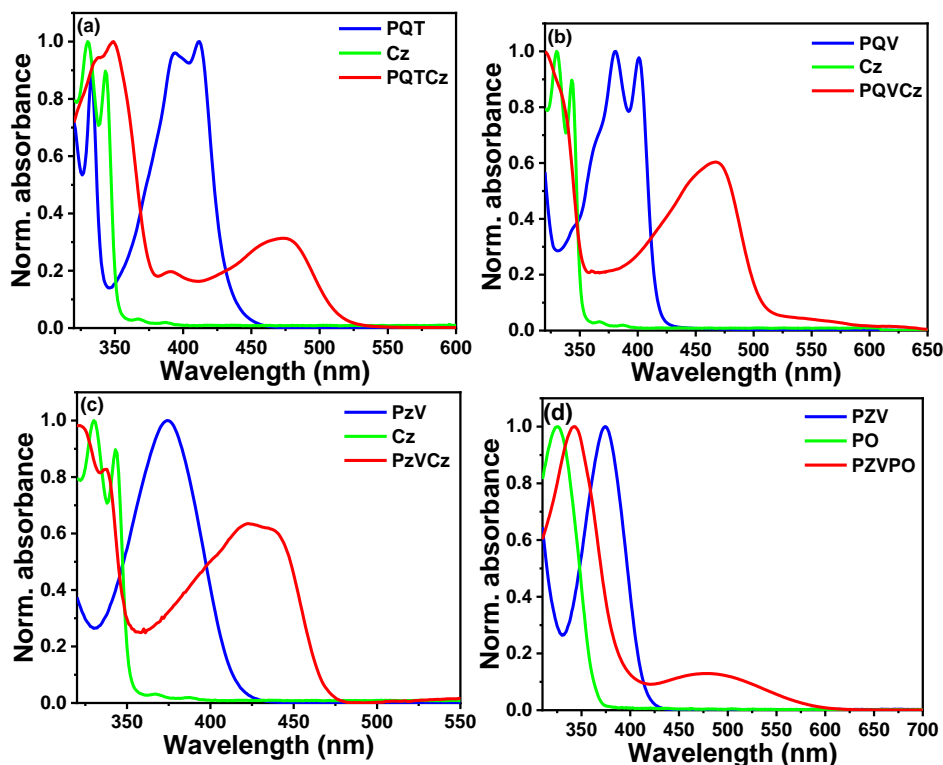
**<sup>1</sup>H NMR (500 MHz in CDCl<sub>3</sub>, δ<sub>H</sub>)** 9.23 (1 H, d, *J* = 2.6 Hz), 8.66 (1 H, d, *J* = 2.6 Hz), 7.93 – 7.90 (2 H, m), 7.88 – 7.85 (2 H, m), 7.44 (4 H, m), 6.82 (4 H, m), 6.72 – 6.63 (10 H, m), 6.54 (4 H, m), 6.19 (2 H, m), 5.97 (4 H, m). **<sup>13</sup>C NMR (176 MHz in CDCl<sub>3</sub>, δ<sub>C</sub>)**: 157.53, 155.77, 154.29, 148.85, 144.45, 143.95, 140.68, 140.65, 139.42, 138.03, 137.85, 137.28, 136.97, 133.82, 133.79, 133.03, 132.92, 132.63, 131.19, 130.95, 123.53, 123.45, 123.41, 123.03, 121.77, 121.74, 116.37, 115.70, 115.67, 113.71, 113.13. **HRMS (APCI):** [M+H]<sup>+</sup> (*m/z*) calculated for C<sub>55</sub>H<sub>34</sub>N<sub>6</sub>O<sub>3</sub>: 827.2771; found: 827.2744. **M. Pt.:** 348 °C (decomp.).



**Scheme S6** Synthetic route of 10,10'-((7-(10*H*-phenoxazin-10-yl)pyrido[2,3-*b*]pyrazine-2,3-diyl)bis(4,1-phenylene))bis(10*H*-phenoxazine) (PZVPO).

## IV. Spectroscopic characterization

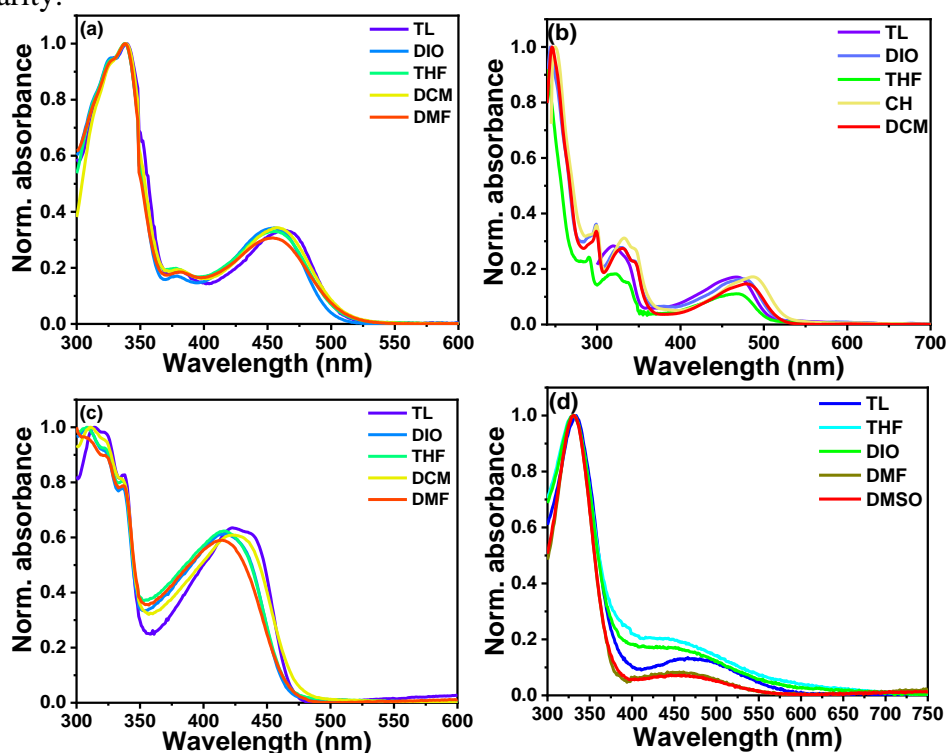
### 4.1 Electronic absorption:



**Fig. S1** Normalized absorption spectra of (a) PQTcZ, (b) PQVcZ, (c) PzVcZ, and (d) PzVPO compared with absorption of the respective acceptor (PQT, PQV, and PzV) cores and donor carbazole (Cz) and phenoxazine (PO) units in toluene.

The absorption spectra of the four D<sub>3</sub>-A compounds PQTcZ, PQVcZ, PzVcZ, and PzVPO were compared with that of their constituent units (donor and acceptor) in toluene.<sup>19</sup> The prominent absorption bands for all the four compounds were observed mostly in the UV region, solely contributed by the donor units (carbazole or phenoxazine). On the other hand, the small hump (at 350 to 390 nm) in the absorption spectra can be attributed due to the acceptor cores PQT and PzV in PQTcZ and PzVcZ, respectively (Fig. S1a, c). Whereas, such humps were not noticeable in PQVcZ and PzVPO due to the effective electronic communication between the acceptor cores and the donor units (Fig. S1b, d). The red-shifted absorption bands in the visible region for all the D<sub>3</sub>-A compounds were due to the extended conjugation between the donors and acceptor units. Both PQTcZ and PQVcZ showed a broad absorption band at around 470 nm (Fig. S1a, b). However, the intensity of the band was much higher for PQVcZ as compared to that of PQTcZ. The facile electronic communication due to the 3,6-connectivity (*para* substitution, V shape) in PQVcZ is the reason behind such observation.<sup>18,20</sup> On the other hand, when we moved from PQVcZ to PzVcZ, a comparatively blue-shifted broad absorption band was noticed at 430 nm. It is due to the flexible conformation of the Pz core as compared to that of the rigid PQ core (Fig. S1b and S1c). The red shift in absorption of PzVPO as compared to PzVcZ is due to the strong donor group phenoxazine over carbazole. The similar nature of absorption in PQVcZ, PzVcZ, and PzVPO was due to the *para*-substituted donor in PQV and PzV. The direct ground state communication between the donor and acceptor through +R effect is the origin of red-shifted absorption in D<sub>3</sub>-A compounds.<sup>18,19</sup>

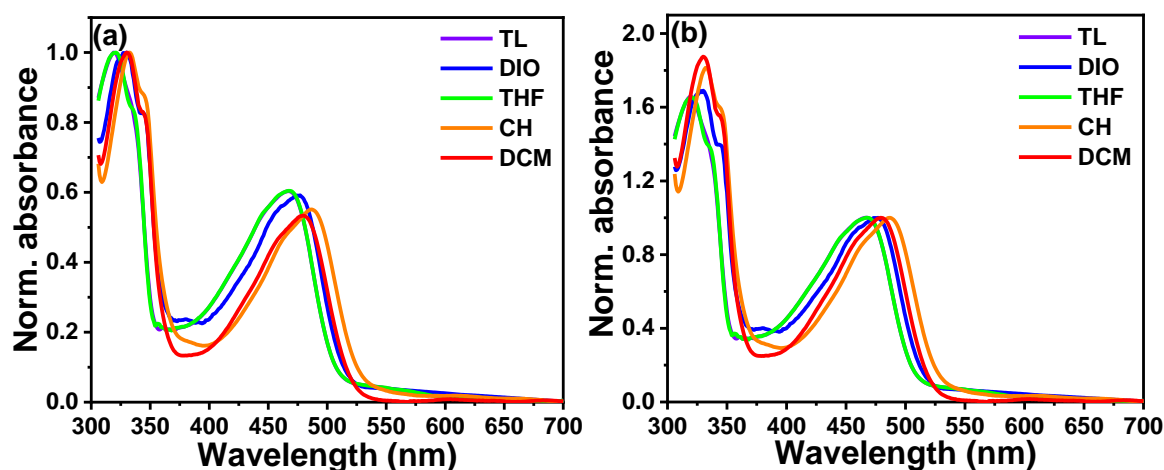
Steady-state absorption measurements of PQTCz, PQVCz, PZVCz, and PZVPO were carried out in five different solvents of varying polarity (Fig. S2). There is no significant change of absorption with solvent polarity for all the compounds. It indicates that the ground state geometry is not perturbed with the solvent polarity.<sup>19, 21</sup>



**Fig. S2** Normalized absorption spectra of (a) PQTCz, (b) PQVCz, (c) PZVCz, and (d) PZVPO in different solvents with varying polarity. TL: toluene, DIO: 1,4-dioxane, THF: tetrahydrofuran, DCM: dichloromethane, DMF: dimethylformamide, CH: chloroform, DMSO: dimethyl sulfoxide.

## 4.2 Absorption analysis:

The prominent absorption band of PQVCz, ranging from  $\lambda_{\text{abs}} = 320\text{-}332\text{ nm}$ , is due to the  $\pi\text{-}\pi^*$  transitions. Comparing with the precursors carbazole (Cz) and PQV unit, as shown in Fig. S1b suggests that the band at around 320 nm is due to the Cz absorption. Instead of the PQV absorption band at around 380-400 nm, a new red shifted absorption band around 470 nm was observed in PQVCz. The slight red shift with solvent polarity (not consistent) indicates intramolecular charge transfer (ICT). However, progressive red shift with solvent polarity as expected for the strong solvatochromic dye was not observed in PQVCz as well as in other D<sub>3</sub>-A compounds. On the other hand, all the compounds exhibit strong ICT fluorescence upon excitation. Additionally, the excitation spectra in different polar solvents also revealed a similar nature that observed from the absorption spectra (Fig. S6b).



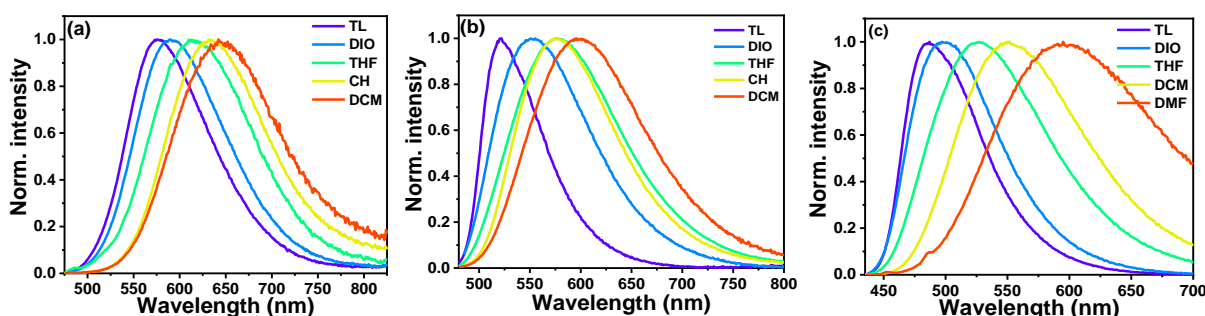
**Fig. S3** The absorption spectra of PQVCz normalized at (a)  $\pi$ - $\pi^*$  and (b) ICT bands in different solvents with varying polarity. TL: toluene, DIO: 1,4-dioxane, THF: tetrahydrofuran, CH: chloroform, DCM: dichloromethane.

**Table S3** Molar absorption coefficients ( $\epsilon$ ) of D<sub>3</sub>-A compounds in toluene at  $\pi$ - $\pi^*$  and ICT bands.

| Compd. | Absorption bands (nm)   |   |
|--------|---|---|
|        | $\pi$ - $\pi^*$ ( $\epsilon$ , M <sup>-1</sup> cm <sup>-1</sup> ) | ICT ( $\epsilon$ , M <sup>-1</sup> cm <sup>-1</sup> ) |
| PQTCz  | 338 (20645)   | 470 (6153)  |
| PQVCz  | 320 (20500)   | 469 (12402)   |
| PZVCz  | 325 (26214)   | 430 (15746)   |
| PZVPO  | 343 (27522)   | 481 (3862)  |

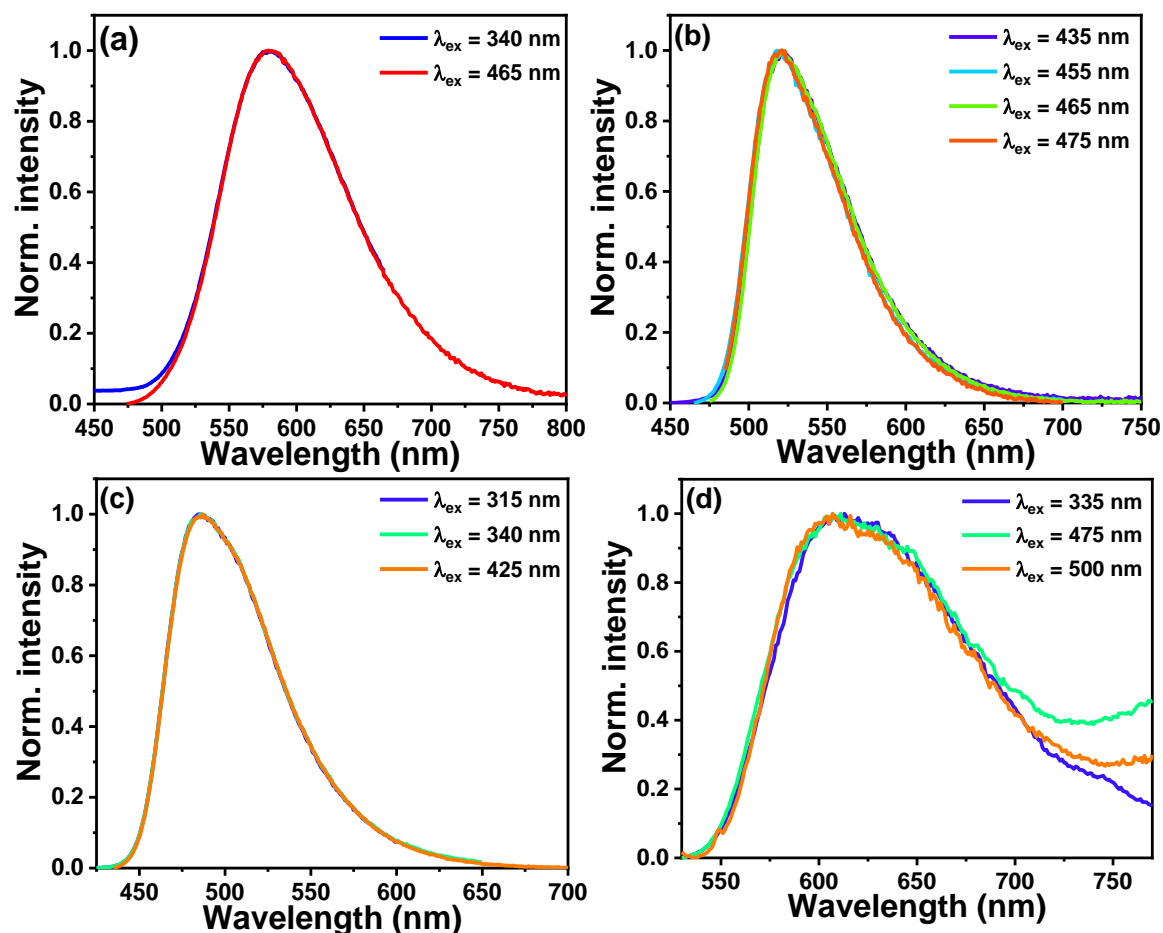
### 4.3 Electronic Emission:

Steady-state emission measurements of PQTCz, PQVCz, PZVCz, and PZVPO were carried out in five different solvents of varying polarity. Emission spectra of PQTCz, PQVCz, and PZVCz were found to be gradually red-shifted with increasing solvent polarity depicting highly sensitive solvatochromic behaviour (Fig. S4).<sup>22</sup> However, PZVPO was almost nonemissive in moderately polar and polar solvents due to strong D-A pair leading to dark TICT state.<sup>21</sup> Hence, we checked the emission of PZVPO in nonpolar solvent toluene only. The red region emission band at 625 nm indicates the facile ICT behaviour of PZVPO among the series of D<sub>3</sub>-A compounds (Fig. S5d).



**Fig. S4** Normalized emission spectra of (a) PQTCz ( $\lambda_{\text{ex}} = 465$  nm), (b) PQVCz ( $\lambda_{\text{ex}} = 465$  nm), and (c) PZVCz ( $\lambda_{\text{ex}} = 425$  nm) in different solvents with varying polarity. TL: toluene, DIO: 1,4-dioxane, THF: tetrahydrofuran, DCM: dichloromethane, DMF: dimethylformamide, CH: chloroform, DMSO: dimethyl sulfoxide.

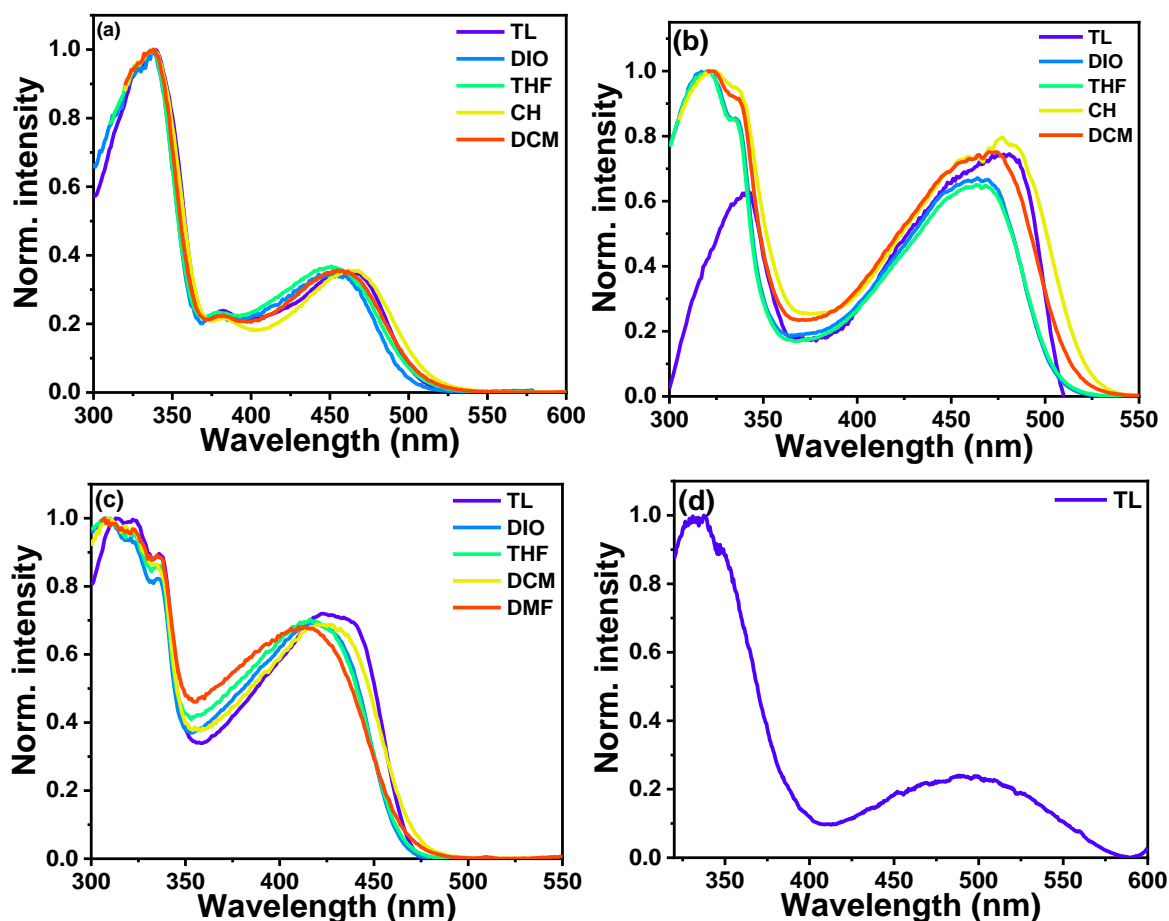
The large solvatochromic shifts in the fluorescence spectra with no significant shift in the absorption spectra on increasing the solvent polarity indicate the presence of a highly polarized excited state with respect to the ground state. The spectral broadening of the emission band and positive solvatochromic behaviour are the two characteristic features indicative of the presence of a strong ICT character.<sup>19, 21</sup> The ICT behaviour was further substantiated through Lippert-Mataga plot (*vide infra*).



**Fig. S5** Normalized emission spectra of (a) PQTCz, (b) PQVCz, (c) PZVCz, and (d) PZVPO in toluene at different excitation wavelengths.

The emission was found to be independent of the excitation wavelength for all the D<sub>3</sub>-A compounds (Fig. S5). It signifies that the emission is coming from the same energy state irrespective of excitation wavelengths. Further, the excitation spectra were recorded with varying solvent polarity at respective emission maxima in different solvents. As shown in Fig. S6, the excitation spectra are similar to the corresponding absorption spectra and remain unchanged with varying solvent polarity.<sup>19</sup>





**Fig. S6** Normalized excitation spectra of (a) PQTCz ( $\lambda_{em} = 570$  nm), (b) PQVCz ( $\lambda_{em} = 520$  nm), (c) PZVCz ( $\lambda_{em} = 490$  nm) and, (d) PZVPO ( $\lambda_{em} = 615$  nm in TL) in different polar solvents. TL: toluene, DIO: 1,4-dioxane, THF: tetrahydrofuran, DCM: dichloromethane, CH: chloroform, DMF: dimethylformamide.

#### 4.4 Lippert-Mataga plot:

Lippert-Mataga (L-M) theory of general solvent effects provides a useful framework to understand the solvent-dependent spectral shifts.<sup>19, 21, 22</sup> The interactions between the solvent molecules and the fluorophore affect the energy difference between the ground and the excited state of the fluorophore. The energy difference is a property of the refractive index ( $n$ ) and dielectric constant ( $\epsilon$ ) of the solvent and is described by the L-M equation as:

$$\Delta\bar{\nu} = \bar{\nu}_a - \bar{\nu}_f = \frac{2}{hc} \left( \frac{\epsilon-1}{2\epsilon+1} - \frac{n^2-1}{2n^2+1} \right) \frac{(\mu_E - \mu_G)^2}{a^3} + \text{constant} \quad (1)$$

$$\text{or, } \Delta\bar{\nu} = \frac{2}{hc} (\Delta f) \frac{(\mu_E - \mu_G)^2}{a^3} + \text{constant} \quad (2)$$

where,

$\bar{\nu}_a$  and  $\bar{\nu}_f$ : wavenumbers ( $\text{cm}^{-1}$ ) of the absorption and emission, respectively

$\mu_E$  and  $\mu_G$ : dipole moments of the fluorophore in the excited and ground states, respectively

$\Delta f$ : orientation polarizability of the solvent

$a$ : radius of the cavity in which fluorophore resides

$h$ : Planck's constant

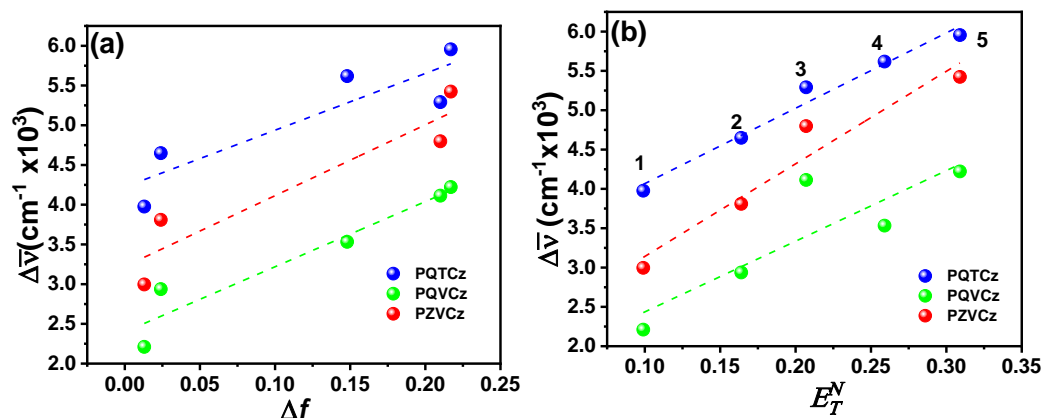
$c$ : speed of light in vacuum

The L-M equation is an approximation in which the polarizability of the fluorophore and higher-order terms are neglected. The specific solvent fluorophore interactions, such as hydrogen bonding and formation of charge-transfer states, are excluded. According to this model, only solvent reorientation is expected to result in a substantial Stokes shift. Thus, an ideal L-M plot demonstrates the linear relation of Stokes shift ( $\Delta\bar{\nu}$ ) and orientation polarizability of the solvent ( $\Delta f$ ). However, as depicted in Fig. S7, a clear deviation from linearity is observed in the L-M plot for PQTCz ( $R^2 = 0.73$ ). However, a better linear fitting was observed for PQVCz ( $R^2 = 0.90$ ) and PZVCz ( $R^2 = 0.82$ ). This is consistent with the formation of a highly dipolar excited state ICT or TICT for D<sub>3</sub>-A compounds, particularly in PQTCz due to strong charge transfer interactions as compared to PQVCz and PZVCz.<sup>18, 19, 21, 22</sup>

**Table S4** Reichardt's solvent polarity parameters,  $E_T^N$ , dielectric constants ( $\epsilon$ ), refractive indices ( $\eta$ ), orientation polarizabilities ( $\Delta f$ ) of different solvents including the Stokes shift ( $\Delta\bar{\nu}$ ) of PQTCz, PQVCz, and PZVCz as a function of the different solvents.

| Solvent parameters |         |            |        |            | Stokes shift (cm <sup>-1</sup> ) |       |       |       |
|--------------------|---------|------------|--------|------------|----------------------------------|-------|-------|-------|
| Entry              | $E_T^N$ | $\epsilon$ | $\eta$ | $\Delta f$ | PQTCz                            | PQVCz | PZVCz | PZVPO |
| Toluene            | 0.099   | 2.38       | 1.497  | 0.013      | 3976                             | 2210  | 2996  | 5245  |
| 1,4- dioxane       | 0.164   | 2.25       | 1.422  | 0.024      | 4649                             | 2937  | 3809  | -     |
| Tetrahydrofuran    | 0.207   | 7.58       | 1.407  | 0.210      | 5291                             | 4114  | 4798  | -     |
| Chloroform         | 0.259   | 4.81       | 1.446  | 0.148      | 5619                             | 3532  | -     | -     |
| Dichloromethane    | 0.309   | 8.93       | 1.424  | 0.217      | 5955                             | 4222  | 5424  | -     |

A relationship between the solvent polarity parameter ( $E_T^N$ ) and Stokes shift ( $\Delta\bar{\nu}$ ) in various solvents was studied to probe the nature of the dipole-dipole interaction between the fluorophore and the solvent molecules.<sup>22</sup> Generally, such an interaction is highly stabilized in solvents of high polarity given that the excited state is also highly dipolar in nature. Consequently, a larger Stokes shift is expected in a more polar solvent. The same is demonstrated through Reichardt's plot (Fig. S7). A linear relationship was observed between the Stokes shift and solvent polarity for all the D<sub>3</sub>-A compounds.



**Fig. S7** (a) Lippert-Mataga plot illustrating the Stokes shift ( $\Delta\bar{\nu}$ ) versus the solvent orientation polarizability ( $\Delta f$ ) and (b) Reichardt's plot depicting the Stokes shift ( $\Delta\bar{\nu}$ ) versus the solvent polarity parameter ( $E_T^N$ ) of PQTCz (blue), PQVCz (green), and PZVCz (red) in different polar solvents. The numbers in the plot refer to the solvents: (1) toluene, (2) 1,4- dioxane, (3) tetrahydrofuran, (4) chloroform, and (5) dichloromethane. The dotted line represents the best linear fit.

To define the solvent polarity in Reichardt's plot,  $E_T(30)$  and  $E_T^N$  values for different solvents are used.  $E_T(30)$  is defined as the molar electronic transition energies ( $E_T$ ) of dissolved pyridinium N-phenolate betaine dye measured in kilocalories per mole ( $\text{kcal}\cdot\text{mol}^{-1}$ ) at room temperature ( $25\text{ }^\circ\text{C}$ ) and normal pressure (1 bar).<sup>22</sup>

$$E_T(30) (\text{Kcal mol}^{-1}) = hc\bar{\nu}_{max}N_A \quad (3)$$

Where  $h$  is the Plank's constant,  $c$  is the speed of light,  $N_A$  is Avogadro's number, and  $\nu$  is the electronic transition energy in wavenumber.  $E_T^N$  is the normalized value for which water and tetramethylsilane (TMS) are used as extreme polar and non-polar reference solvents, respectively. The normalized  $E_T^N$  value is scaled approximately from 0 for TMS, the least polar solvent to 1.000 for water, the most polar solvent.

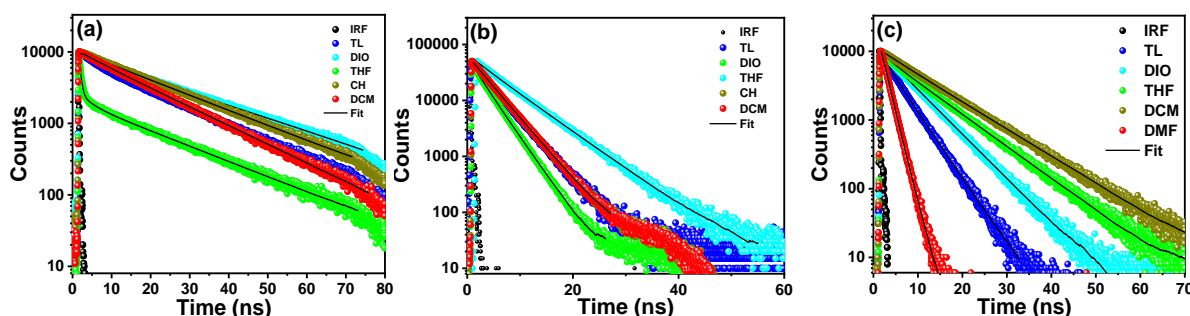
$$E_T^N = \left( \frac{E_T(\text{solvent}) - E_T(\text{TMS})}{E_T(\text{water}) - E_T(\text{TMS})} \right) \quad (4)$$

#### 4.5 Fluorescence quantum yield and time-resolved spectroscopy:

The fluorescence quantum yields of PQTCz, PQVCz, and PZVPO were estimated by comparison with quinine hemisulfate dye in 0.1 M  $\text{HClO}_4$  ( $\Phi_f = 0.59$ ). The quantum yield of PZVCz was calculated using Coumarin 153 dye in EtOH ( $\Phi_f = 0.53$ ).<sup>23, 24</sup>

$$\Phi_{f,x} = \Phi_{f,s} * \frac{F_x}{F_s} * \frac{f_s}{f_x} * \frac{n_x^2}{n_s^2} \dots \quad (5)$$

Where  $\Phi_f$  is the fluorescence quantum yield, the subscript  $x$  denotes sample, and the subscript  $s$  refers to the standard dye.  $F$  denotes integral fluorescence,  $n$  refers to the refractive index of the solvent used in the measurements and  $f$  is the absorption factor at the excitation wavelength given by the following equation:  $f = 1 - 10^{-\varepsilon(\lambda_{ex})cl} = 1 - 10^{-A(\lambda_{ex})}$ , where  $A$  is the absorbance, and  $\varepsilon$  = molar extinction coefficient in  $\text{L mol}^{-1} \text{cm}^{-1}$ .



**Fig. S8** Emission decay profiles of (a) PQTCz ( $\lambda_{ex} = 468\text{ nm}$ ), (b) PQVCz ( $\lambda_{ex} = 468\text{ nm}$ ), and (c) PZVCz ( $\lambda_{ex} = 410\text{ nm}$ ) in different polar solvents. TL: toluene, DIO: 1,4-dioxane, THF: tetrahydrofuran, DCM: dichloromethane, DMF: dimethylformamide, CH: chloroform, DMSO: dimethyl sulfoxide.

All the compounds showed a biexponential emission decay profile at room temperature in solvents of varying polarities (Fig. S8). Such a biexponential emission decay profile was observed presumably due to the presence of mixed locally excited (LE) and ICT states.

## 4.6 Spectroscopic data table:

**Table S5** Spectroscopic data of PQTCz in various organic solvents; the decay times ( $\tau_1$ ,  $\tau_2$ ), the respective percentage contributions ( $\alpha_1$ ,  $\alpha_2$ ), and the quality of fitting ( $\chi^2$ ) are shown.

| Solvent      | Entry | Abs.<br>$\lambda_{\max}$ (nm) | Emission<br>$\lambda_{\max}$ (nm) | Quantum Yield<br>% | Stokes shift<br>(nm) | $\Delta\bar{\nu}$<br>( $\text{cm}^{-1}$ ) | Lifetime (ns)<br>( $\lambda_{\text{ex}} = 468$ nm) |            |               |            |              |
|--------------|-------|-------------------------------|-----------------------------------|--------------------|----------------------|---|--|------------|---------------|------------|--------------|
|              |       |                               |                                   |                    |                      |   | $\tau_1$ (ns)                                      | $\alpha_1$ | $\tau_2$ (ns) | $\alpha_2$ | ( $\chi^2$ ) |
| Toluene      | 0.099 | 470                           | 575                               | 18                 | 107                  | 3976                                      | 3.8  | 7          | 18.4          | 93         | 1.01         |
| 1,4- dioxane | 0.164 | 463                           | 590                               | 21                 | 127                  | 4649                                      | 6.2  | 5          | 25.3          | 95         | 1.11         |
| THF          | 0.207 | 464                           | 615                               | 21                 | 151                  | 5291                                      | 2.8  | 5          | 20.1          | 95         | 1.03         |
| Chloroform   | 0.259 | 468                           | 635                               | 4                  | 167                  | 5619                                      | 2.4  | 1          | 20.3          | 99         | 1.07         |
| DCM          | 0.309 | 466                           | 645                               | 6                  | 179                  | 5955                                      | 7.4  | 6          | 17.0          | 94         | 1.14         |

**Table S6** Spectroscopic data of PQVCz in various organic solvents; the decay times ( $\tau_1$ ,  $\tau_2$ ), the respective percentage contributions ( $\alpha_1$ ,  $\alpha_2$ ), and the quality of fitting ( $\chi^2$ ) are shown.

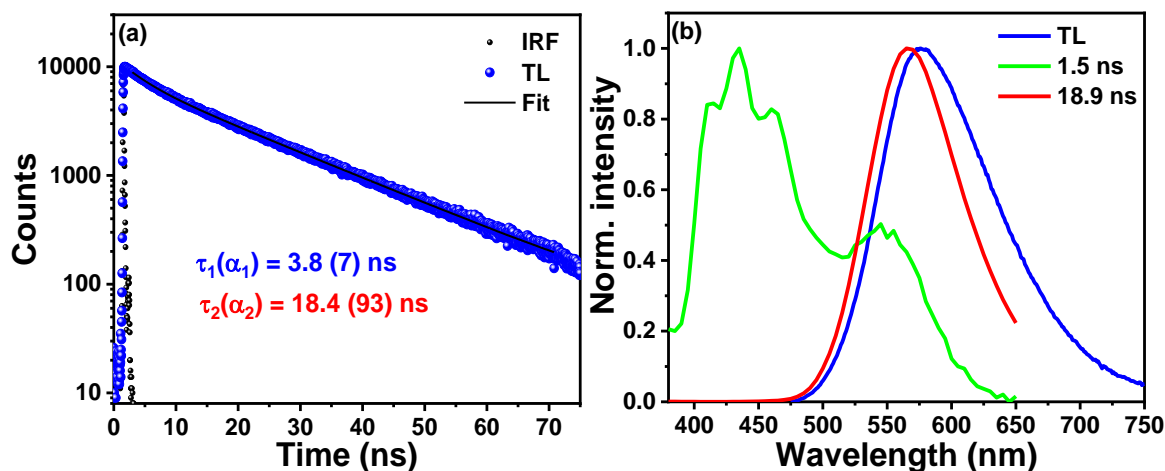
| Solvent      | Entry | Abs.<br>$\lambda_{\max}$ (nm) | Emission<br>$\lambda_{\max}$ (nm) | Quantum Yield<br>% | Stokes shift<br>(nm) | $\Delta\bar{\nu}$<br>( $\text{cm}^{-1}$ ) | Lifetime (ns)<br>( $\lambda_{\text{ex}} = 468$ nm) |            |               |            |              |
|--------------|-------|-------------------------------|-----------------------------------|--------------------|----------------------|---|--|------------|---------------|------------|--------------|
|              |       |                               |                                   |                    |                      |   | $\tau_1$ (ns)                                      | $\alpha_1$ | $\tau_2$ (ns) | $\alpha_2$ | ( $\chi^2$ ) |
| Toluene      | 0.099 | 469                           | 522                               | 6                  | 54                   | 2210                                      | 1.3  | 7          | 4.0           | 93         | 1.16         |
| 1,4- dioxane | 0.164 | 476                           | 552                               | 6                  | 77                   | 2937                                      | 4.3  | 19         | 6.6           | 81         | 1.00         |
| THF          | 0.207 | 469                           | 575                               | 2                  | 110                  | 4114                                      | 3.2  | 6          | 6.6           | 94         | 1.07         |
| Chloroform   | 0.259 | 486                           | 578                               | <1                 | 98                   | 3532                                      | 4.1  | 5          | 8.1           | 95         | 1.2          |
| DCM          | 0.309 | 479                           | 602                               | <1                 | 122                  | 4222                                      | 3.9  | 4          | 7.9           | 96         | 1.2          |

**Table S7** Spectroscopic data of PZVCz in various organic solvents; the decay times ( $\tau_1$ ,  $\tau_2$ ), the respective percentage contributions ( $\alpha_1$ ,  $\alpha_2$ ), and the quality of fitting ( $\chi^2$ ) are shown.

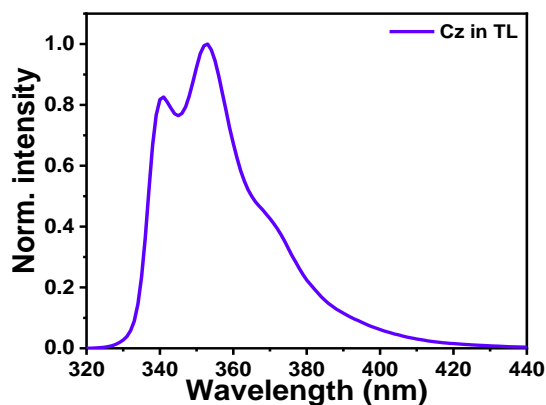
| Solvent      | Entry | Abs.<br>$\lambda_{\max}$ (nm) | Emission<br>$\lambda_{\max}$ (nm) | Quantum Yield<br>% | Stokes shift<br>(nm) | $\Delta\bar{\nu}$<br>( $\text{cm}^{-1}$ ) | Lifetime (ns)<br>( $\lambda_{\text{ex}} = 440$ nm) |            |               |            |              |
|--------------|-------|-------------------------------|-----------------------------------|--------------------|----------------------|---|--|------------|---------------|------------|--------------|
|              |       |                               |                                   |                    |                      |   | $\tau_1$ (ns)                                      | $\alpha_1$ | $\tau_2$ (ns) | $\alpha_2$ | ( $\chi^2$ ) |
| Toluene      | 0.099 | 425, 435                      | 487                               | 15                 | 62, 52               | 2996                                      | 1.2  | 8          | 4.5           | 92         | 1.06         |
| 1,4- dioxane | 0.164 | 420                           | 500                               | 1-2                | 80                   | 3809                                      | 0.8  | 2          | 6.7           | 98         | 1.05         |
| THF          | 0.207 | 420                           | 526                               | 1-2                | 106                  | 4798                                      | 1.6  | 4          | 9.3           | 96         | 1.07         |
| DCM          | 0.309 | 425                           | 552                               | <1                 | 127                  | 5424                                      | 5.5  | 4          | 11.1          | 96         | 1.13         |

## V. Time resolved Emission Spectra (TRES): LE vs. ICT

A single emission band at  $\lambda_{em} = 565$  nm was observed for PQTCz in toluene. However, a biexponential emission decay was observed with the decay time 3.8 ns and 18.4 ns. To get the decay associated emission spectra for a particular timescale, emission decays from 350 nm to 750 nm with the gap of 5 nm were measured. The reconstructed decay-associated fluorescence spectra at 1.5 ns and 18.9 ns showed two different spectral profiles (Fig. S9). The emission spectrum at 18.9 ns is due to the charge transfer emission.<sup>25</sup> The spectral profile at 1.5 ns is quite similar to that of carbazole in toluene, which indicates the emission from the locally excited (LE, Fig. S10) state.

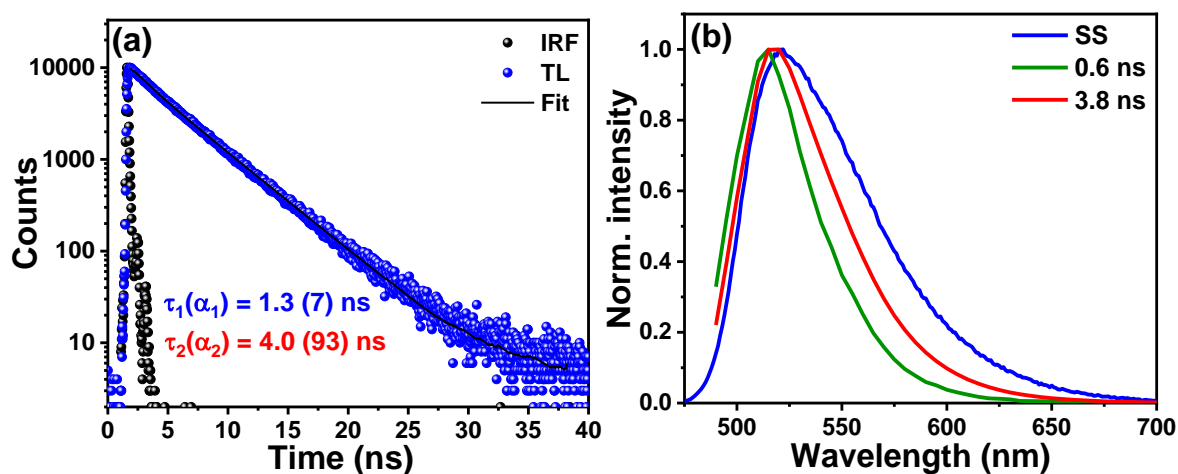


**Fig. S9** (a) Emission decay profile ( $\lambda_{ex} = 468$  nm,  $\lambda_{em} = 570$  nm), and (b) time-resolved emission spectra of PQTCz along with the steady-state (SS) emission spectrum in toluene at room temperature.

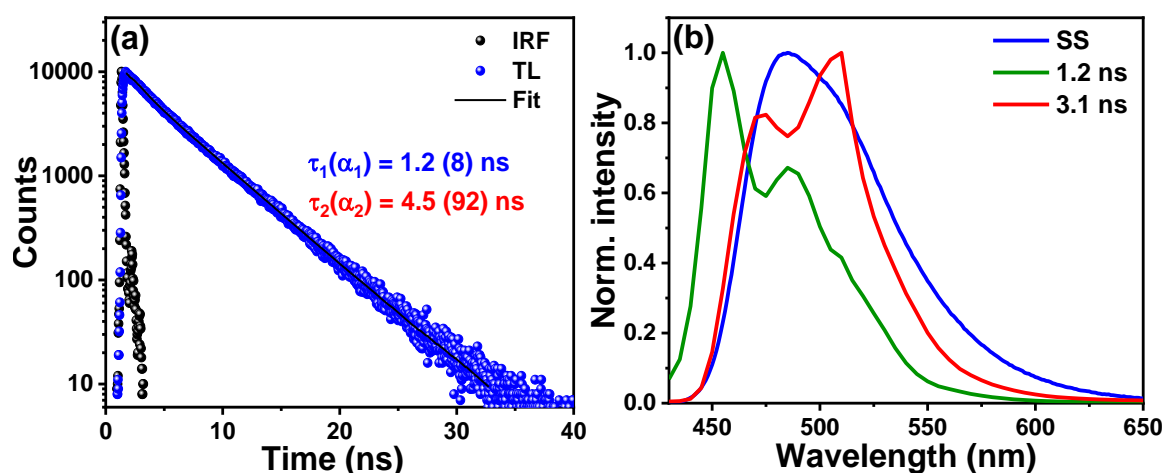


**Fig. S10** The normalized emission spectrum ( $\lambda_{ex} = 300$  nm) of carbazole in toluene at room temperature.

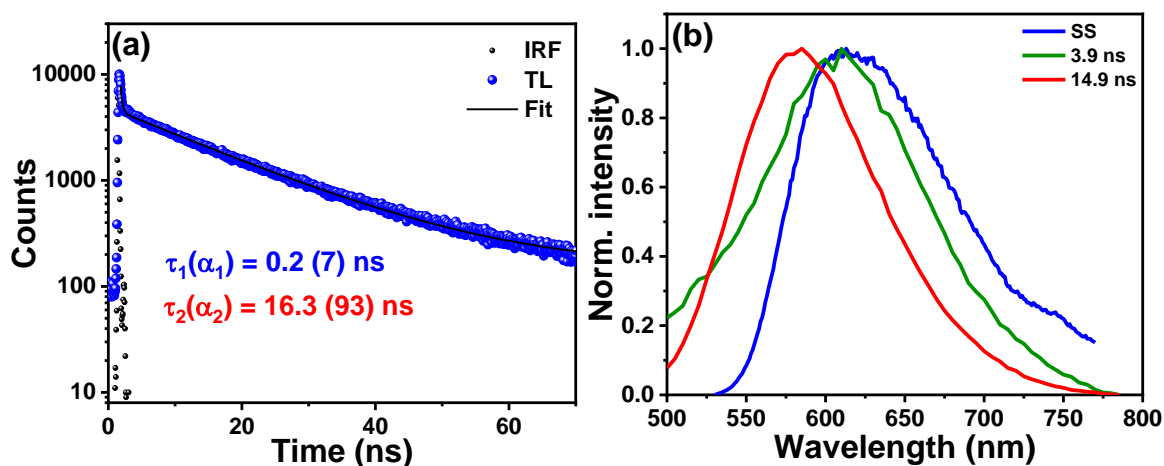
The biexponential fluorescence decay of PQVCz in toluene at room temperature was observed with the decay time 1.3 and 4.0 ns (Fig. S11). Interestingly, the decay associated spectra of PQVCz at 1.3 and 4.0 ns are identical. This is due to the facile ground state communication between the donor and acceptor units in PQVCz, as observed in the absorption spectra. Thus, the structural LE emission due to the donor units was not observed in PQVCz. Similarly, the biexponential decay was observed in PZVCz with the decay time 1.2 and 4.5 ns in toluene at room temperature (Fig. S12). However, a clear signature of LE emission from the donor carbazole was noticeable. The breaking of the ground state communication between the D and A units in PZVCz is due to the flexible  $\pi$ -spacer resulting in the distinct LE and charge transfer emission at room temperature.



**Fig. S11** (a) Emission decay profile ( $\lambda_{\text{ex}} = 468 \text{ nm}$ ,  $\lambda_{\text{em}} = 525 \text{ nm}$ ), and (b) time-resolved emission spectra of PQVCz along with the steady-state (SS) emission spectrum in toluene at room temperature.



**Fig. S12** (a) Emission decay profile ( $\lambda_{\text{ex}} = 410 \text{ nm}$ ,  $\lambda_{\text{em}} = 490 \text{ nm}$ ), and (b) time-resolved emission spectra of PZVCz along with the steady-state (SS) emission in toluene at room temperature.

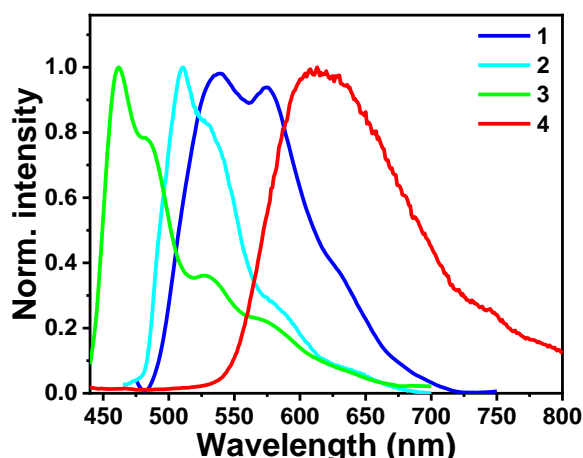


**Fig. S13** (a) Emission decay profile ( $\lambda_{\text{ex}} = 468 \text{ nm}$ ,  $\lambda_{\text{em}} = 620 \text{ nm}$ ), and (b) time-resolved emission spectra of PZVPO along with the steady-state (SS) emission spectrum in toluene at room temperature.

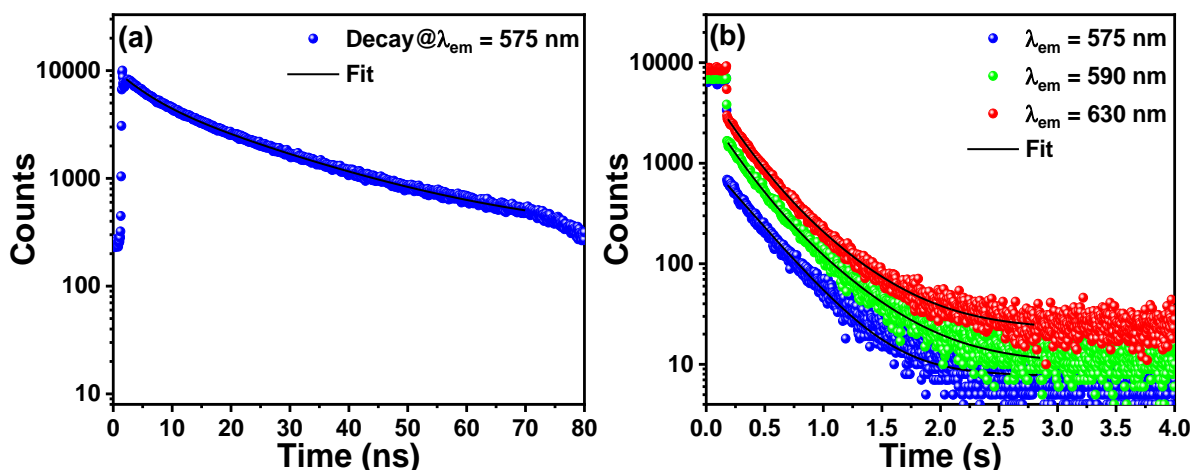
## VI. Low-temperature emission measurements

### 6.1 Steady-state emission spectra:

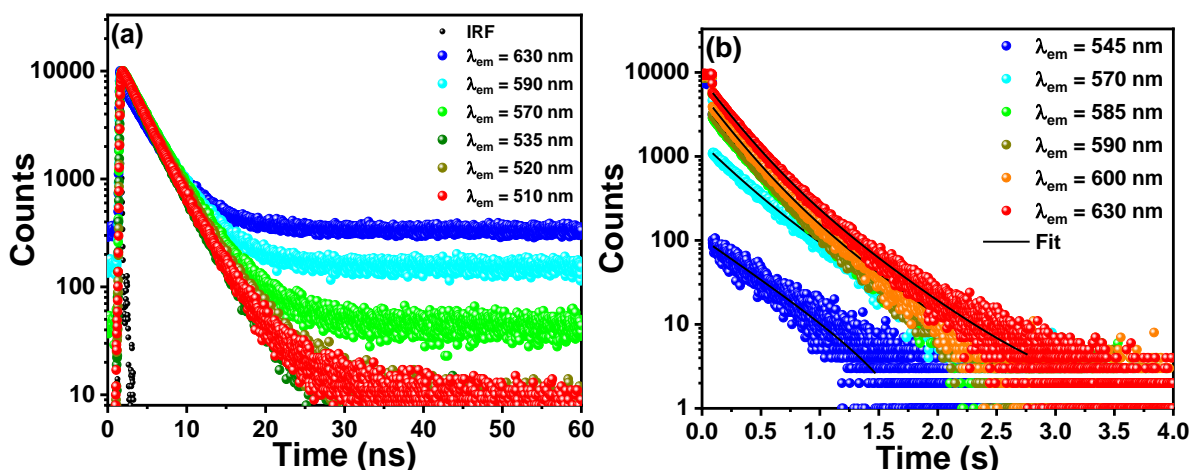
The fluorescence emission spectra of PQTCz, PQVCz, PZVCz, and PZVPO at liquid nitrogen temperature (77 K) provide important insights about their photophysical characteristics in the condensed state.<sup>3</sup> A significant emission is observed from all the four D-A compounds at 77 K (Fig. S14). The intramolecular rotations across the D-A bonds are restricted to a large extent owing to the increased rigidity of the molecular environment. This, in turn, inhibits the thermally activated non-radiative decay channels and results in substantial photoluminescence. The appearance of the featured bands for all the compounds at 77 K as compared to that of the solution state is presumably due to the formation of the rigid molecular structure at such low temperatures.



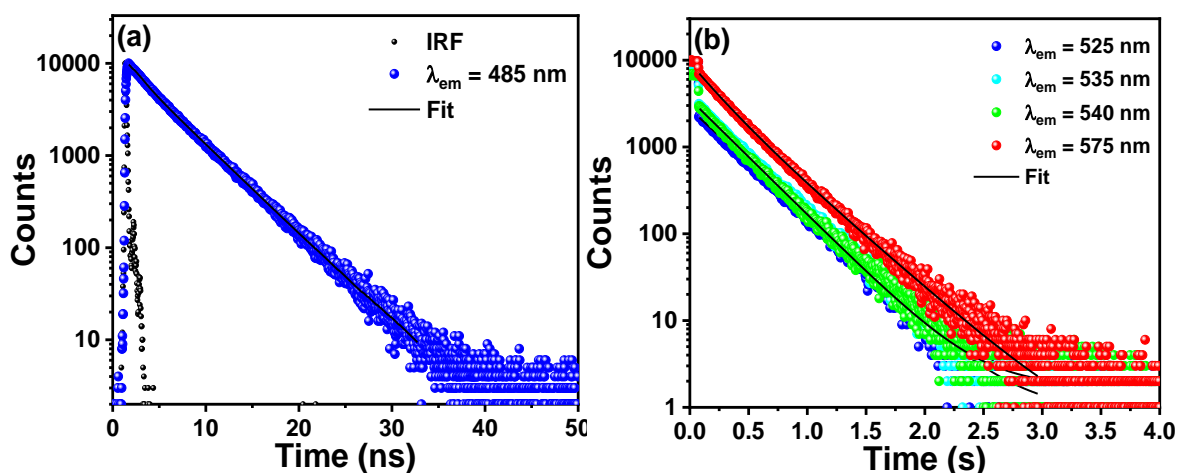
**Fig. S14** Normalized emission spectra of (1) PQTCz, (2) PQVCz, (3) PZVCz, and (4) PZVPO in toluene at 77 K.



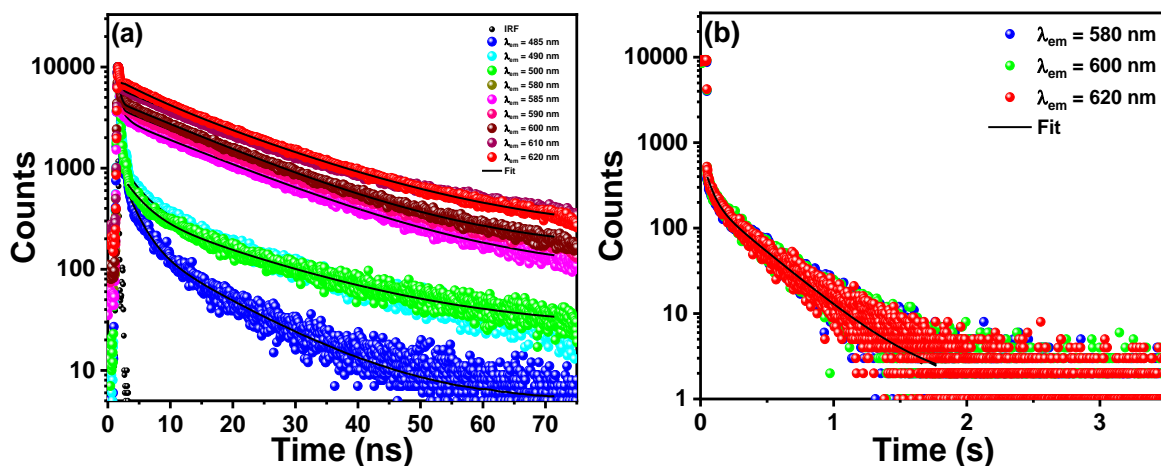
**Fig. S15** Emission decay profiles of PQTCz in (a) nanosecond ( $\lambda_{ex} = 468$  nm) and (b) second ( $\lambda_{ex} = 461$  nm) timescale in toluene at 77 K.



**Fig. S16** Emission decay profiles of PQVCz in (a) nanosecond ( $\lambda_{\text{ex}} = 468$  nm) and (b) second ( $\lambda_{\text{ex}} = 461$  nm) timescale in toluene at 77 K.



**Fig. S17** Emission decay profiles of PZVCz in (a) nanosecond ( $\lambda_{\text{ex}} = 410$  nm) and (b) second ( $\lambda_{\text{ex}} = 417$  nm) timescale in toluene at 77 K.



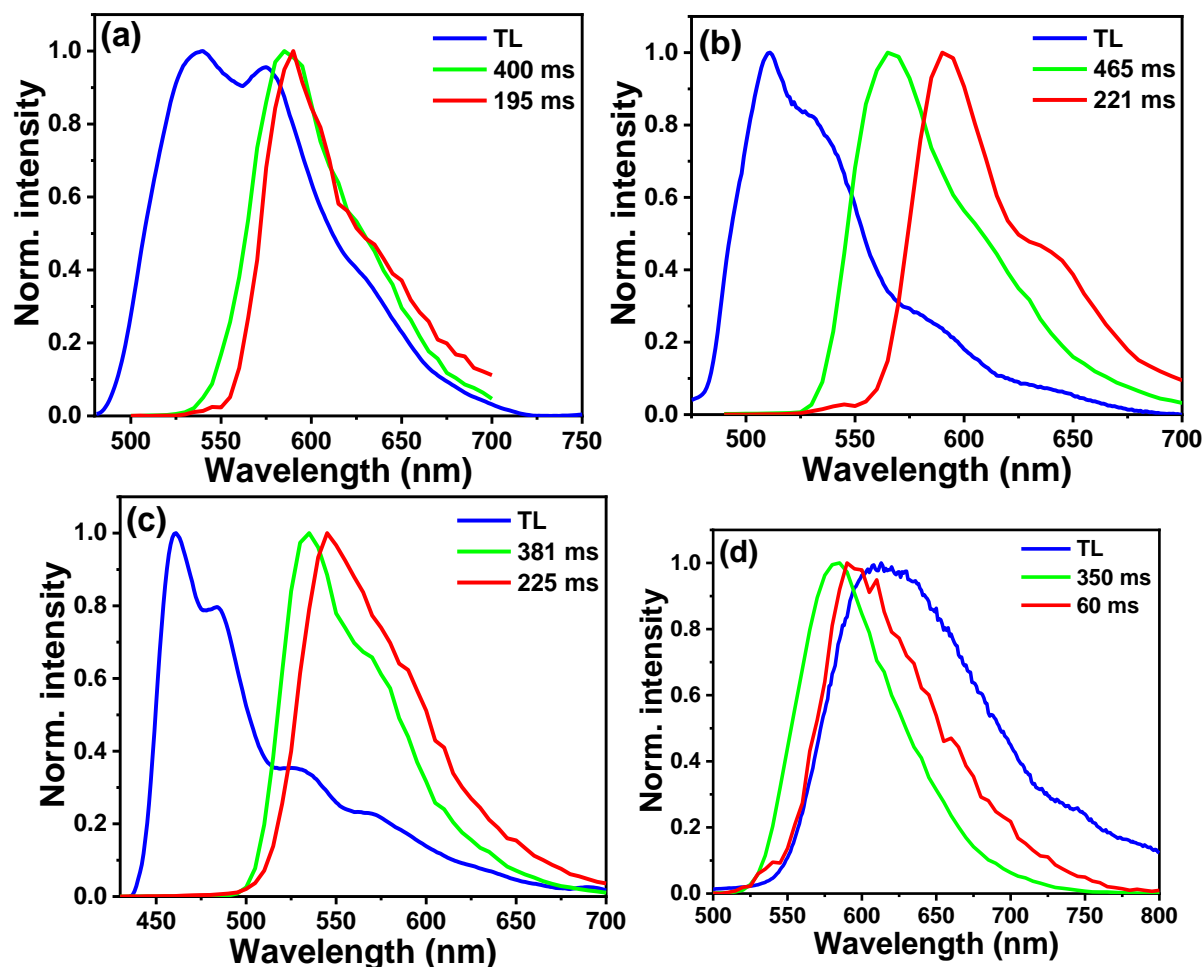
**Fig. S18** Emission decay profiles of PZVPO in (a) nanosecond ( $\lambda_{\text{ex}} = 468$  nm) and (b) second ( $\lambda_{\text{ex}} = 461$  nm) timescale in toluene at 77 K.

All the compounds showed a biexponential emission decay profile at 77 K, monitoring both in the nanosecond as well as the second-time domain (Fig. S15-S18). Such biexponential emission decay profiles were observed presumably due to the presence of mixed LE and ICT states.



## 6.2 Phosphorescence Spectra:

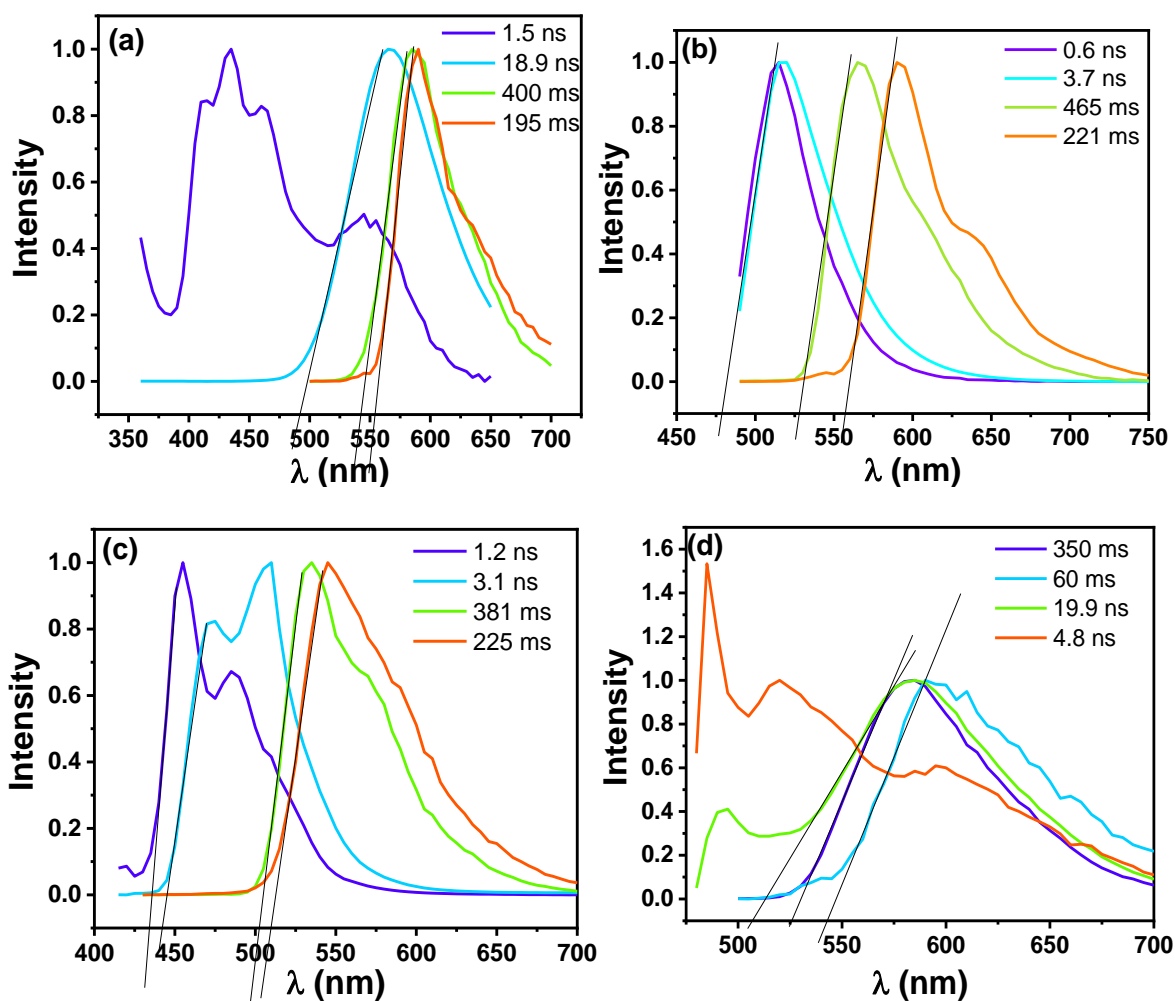
The nature of the phosphorescence emission at 77 K was analyzed using time-resolved emission spectra (TRES) measurements by TCSPC coupled with SpectraLED light source.<sup>26, 27</sup> The millisecond TRES of all the D<sub>3</sub>-A compounds at 77 K are shown in Fig. S19. The phosphorescence emission maxima of PQTCz were observed at 585 and 590 nm with lifetime 400 and 195 ms, respectively. The emission of PQVCz was found at 565 and 590 nm, with the decay time 465 and 221 ms, respectively. The phosphorescence emission peaks of PZVCz were observed at 535 and 545 nm, with decay time 381 and 225 ms, respectively. The phosphorescence decay time of PZVPO was found to be 60 and 350 ms, with peaks centered at 590 and 585 nm, respectively.



**Fig. S19** Time-resolved emission (phosphorescence) spectra (TRES) of (a) PQTCz, (b) PQVCz, (c) PZVCz, and (d) PZVPO in toluene at 77 K.

## 6.3 Experimental calculation of singlet-triplet energy gap ( $\Delta E_{ST}$ ):

The prompt emission (<100 ns time range) at room temperature (fluorescence) and emission in the millisecond timescale at 77 K (phosphorescence) were used for the experimental calculation of the singlet charge transfer state (<sup>1</sup>CT), and the lowest-energy triplet state (<sup>3</sup>CT/T<sub>1</sub>), respectively (Fig. S20).<sup>26</sup>



**Fig. S20** Time-resolved emission spectra (TRES) of (a) PQTCz, (b) PQVCz, (c) PZVCz, and (d) PZVPO at nanosecond (room temperature, fluorescence) and millisecond (77 K, phosphorescence) timescale.

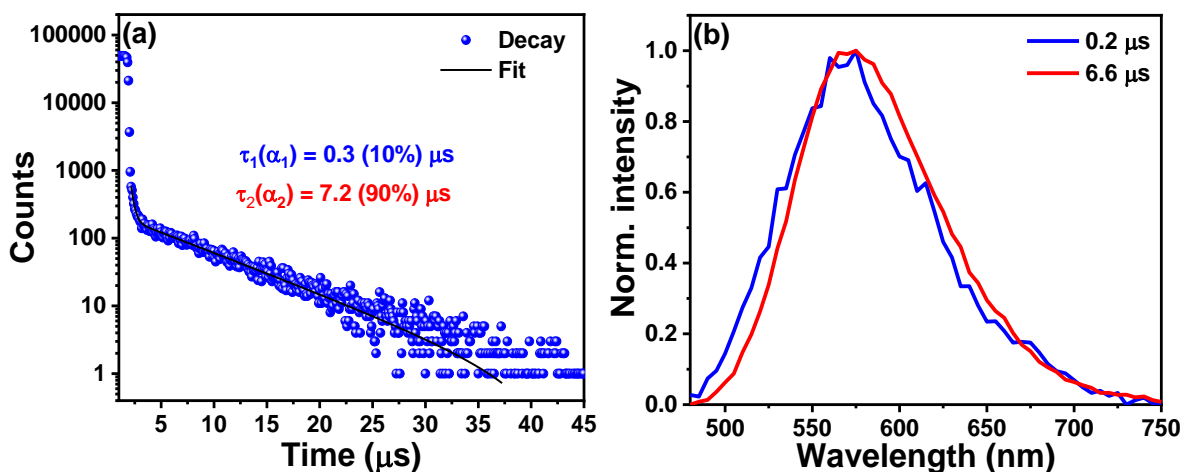
**Table S8** The excited state energy levels and experimental values of the singlet-triplet energy gap ( $\Delta E_{ST}$ ) of D<sub>3</sub>-A compounds.

| Compound Name | T <sub>1</sub> |            | S <sub>1</sub> |            | $\Delta E_{ST}$ |
|---------------|----------------|------------|----------------|------------|-----------------|
|               | nm             | eV         | nm             | eV         | eV              |
| <b>PQTCz</b>  | 542, 554       | 2.29, 2.24 | 490            | 2.53       | <b>0.24</b>     |
| <b>PQVCz</b>  | 530, 558       | 2.33, 2.22 | 482            | 2.57       | <b>0.35</b>     |
| <b>PZVCz</b>  | 503, 510       | 2.46, 2.43 | 434, 442       | 2.85, 2.80 | <b>0.39</b>     |
| <b>PZVPO</b>  | 526, 542       | 2.35, 2.28 | 508            | 2.44       | <b>0.09</b>     |

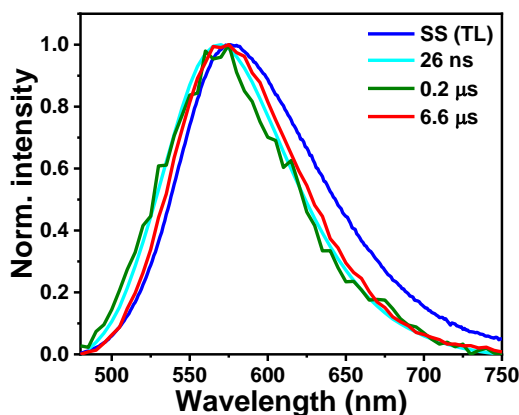
## VII. Delayed Fluorescence

### 7.1 Delayed fluorescence in degassed toluene:

Emission decays of D<sub>3</sub>-A compounds were measured in degassed toluene at microsecond timescale to probe the thermally activated delayed fluorescence (TADF).<sup>6, 28</sup> A biexponential emission decay composed of a component with a decay time of 0.3  $\mu$ s and a long-lived component with decay time 7.2  $\mu$ s was observed for PQTCz at ambient conditions (Fig. S21a). However, no significant photon counts were observed for PQVCz, PZVCz, and PZVPO in degassed toluene. Further, the time-resolved emission spectra of PQTCz in degassed toluene were measured (Fig. S21b). The microsecond decay associated emission spectra were merged with the emission spectrum obtained at nanosecond timescale (prompt fluorescence, Fig. S22) and the steady-state emission with the peak centered at  $\lambda_{em} = 570$  nm at room temperature. The long-lived emission of PQTCz was quenched upon exposure to oxygen. The triplet state is deactivated through the collisions with molecular oxygen (Fig. S23). TRES and emission in oxygenated solvent unambiguously suggest TADF from PQTCz in solution.



**Fig. S21** (a) Emission decay profile ( $\lambda_{ex} = 461$  nm,  $\lambda_{em} = 570$  nm) of PQTCz (5  $\mu$ M) in degassed toluene, and (b) normalized time-resolved emission spectra ( $\lambda_{ex} = 461$  nm) in microsecond timescale at ambient conditions.



**Fig. S22** Normalized time-resolved emission spectra ( $\lambda_{ex} = 468$  nm for ns and  $\lambda_{ex} = 461$  nm for  $\mu$ s timescale) of PQTCz in degassed toluene at ambient conditions depicting the delayed fluorescence.

## 7.2 Oxygen free condition: The delayed-to-prompt fluorescence ratio:

The ratio between the quantum yield of the delayed fluorescence (DF) and the prompt fluorescence (PF) is represented as  $\left(\frac{\phi_{DF}}{\phi_{PF}}\right)$ . The quality of a TADF emitter can be evaluated by the delayed-to-prompt fluorescence ratio. In the present study, we used the steady-state approach to determine the delayed-to-prompt fluorescence ratio. The triplet excited state is strongly quenched by the presence of molecular oxygen; hence, the DF is likely to be suppressed in non-degassed solutions, or films. Therefore, the area under the steady-state fluorescence spectrum for an air-equilibrated sample provides the quantum yield of PF. On the other hand, both the PF and DF contribute to the total emission for a degassed sample. Hence, the ratio of the integrated fluorescence spectra for the samples with degassed and non-degassed conditions will provide the quantum yield ratio of the DF and PF according to the following equation.

$$\frac{\int I_{DF}^{deg}(\lambda)d\lambda}{\int I_{PF}^{O_2}(\lambda)d\lambda} = \frac{\phi_{PF} + \phi_{DF}}{\phi_{PF}} = 1 + \frac{\phi_{DF}}{\phi_{PF}} \quad (6)$$

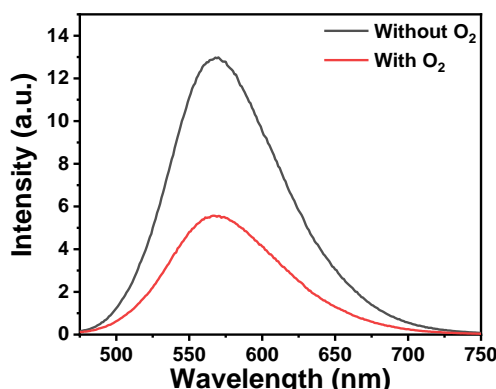
In strong TADF emitters, the triplet yield can be determined directly from equation (7).<sup>28</sup>

The total emission of a TADF emitter ( $\phi_F$ ) is described by equation (7), accounting for the recycling of singlet and triplet states.

$$\begin{aligned} \phi_F &= \phi_{PF} + \phi_{DF} = \sum_{i=1}^n \phi_{PF} (\phi_{ISC} \phi_{RISC})^i \\ &= \phi_{PF} \frac{1}{1 - \phi_{ISC} \phi_{RISC}} \end{aligned} \quad (7)$$

**Table S9** The kinetics data of TADF for PQTcZ in toluene at room temperature.

| $\phi_F$ | $\phi_{PF}$ | $\phi_{DF}$ | $\tau_{PF}$ | $k_F$                            | $\frac{\phi_{DF}}{\phi_{PF}}$ | $\phi_{ISC}$ |
|----------|-------------|-------------|-------------|----------------------------------|-------------------------------|--------------|
| 0.22     | 0.09        | 0.13        | 18.4 ns     | $4.8 \times 10^6 \text{ s}^{-1}$ | 1.44                          | 0.59         |

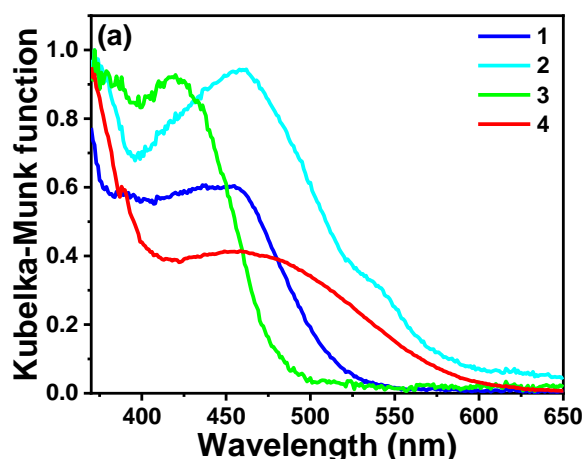


**Fig. S23** Steady-state fluorescence spectra ( $\lambda_{ex} = 465 \text{ nm}$ ) of PQTcZ in toluene at room temperature in the presence and absence of molecular oxygen.

## VIII. Film Photophysics

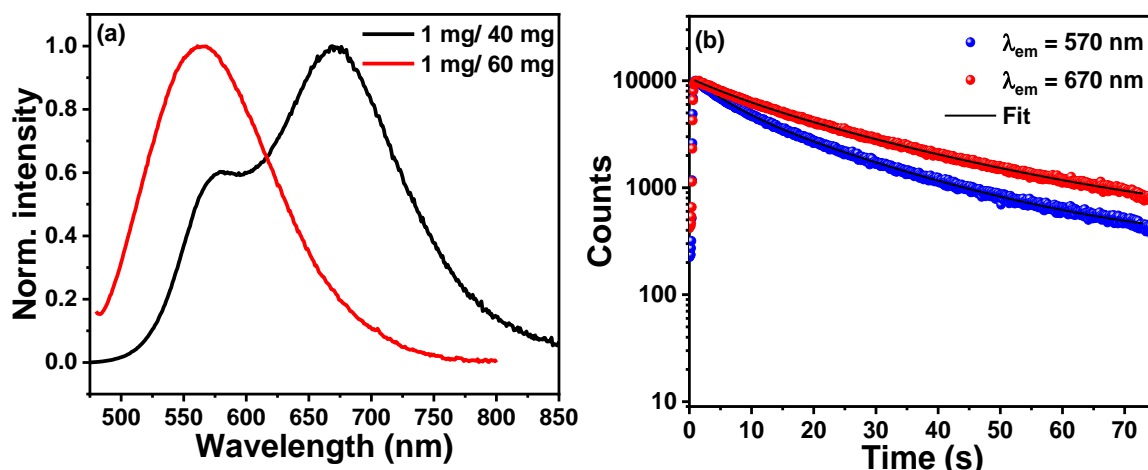
### 8.1 Steady-state and time-resolved spectroscopy:

The D<sub>3</sub>-A compounds were doped in PMMA (polymethyl methacrylate) matrix to study the emission features in a rigid matrix. PMMA was chosen due to its remarkable optical transparency, surface rigidity and dimensional stability. PMMA polymer is ideal for wide-bandgap host materials because it does not interfere with triplet states of visible or infrared-emitting molecules (triplet energy of PMMA = 3.1 eV).<sup>29</sup> The thin films of all the D<sub>3</sub>-A compounds were prepared by mixing ~ 1 mg of each compound with 60 mg of poly(methyl methacrylate) in dry toluene (1 mL). The viscous solution of PMMA:compound was spin-coated at 4000 rpm for 120 s onto cleaned quartz plates.



**Fig. S24** Normalized absorption spectra of (1) PQTCz, (2) PQVCz, (3) PZVCz, and (4) PZVPO doped PMMA thin films at room temperature.

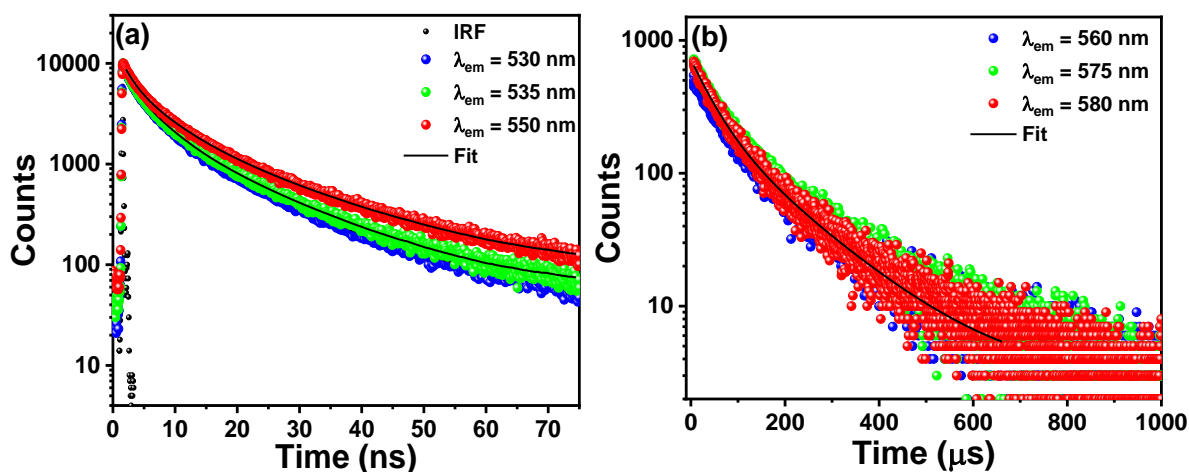
The absorption spectra of the fabricated thin films were measured using diffuse reflectance accessories (DRA) coupled with an absorption spectrophotometer (Fig. S24a). The steady-state emission spectra of thin films are shown in Fig. 2i-l. We fabricated the polymer films of PQTCz in a different fraction of compound and polymer ratios (w/w).<sup>30, 31</sup> A prominent emission band at 570 nm with a red-shifted peak at 670 nm was observed at high PQTCz concentration (1:40, w/w). The peak at 570 nm was due to the charge transfer emission of PQTCz, whereas the lower energy peak centered at 670 nm was likely to be originated from the molecular aggregates (Fig. S25, S26). However, at lower concentrations (1:60, w/w) of PQTCz, only a charge transfer emission peak was observed at  $\lambda_{em} = 570$  nm. Thus, the higher ratio of compound to polymer (1:60, w/w) was chosen for the film preparation of D<sub>3</sub>-A compounds. The steady-state emission spectra do not show a prominent effect of aggregation at the compound:PMMA ratio 1:60 (Fig. S25). The details of emission decays of PQTCz film at lower and higher concentrations at different emission wavelengths are mentioned in Table S9.



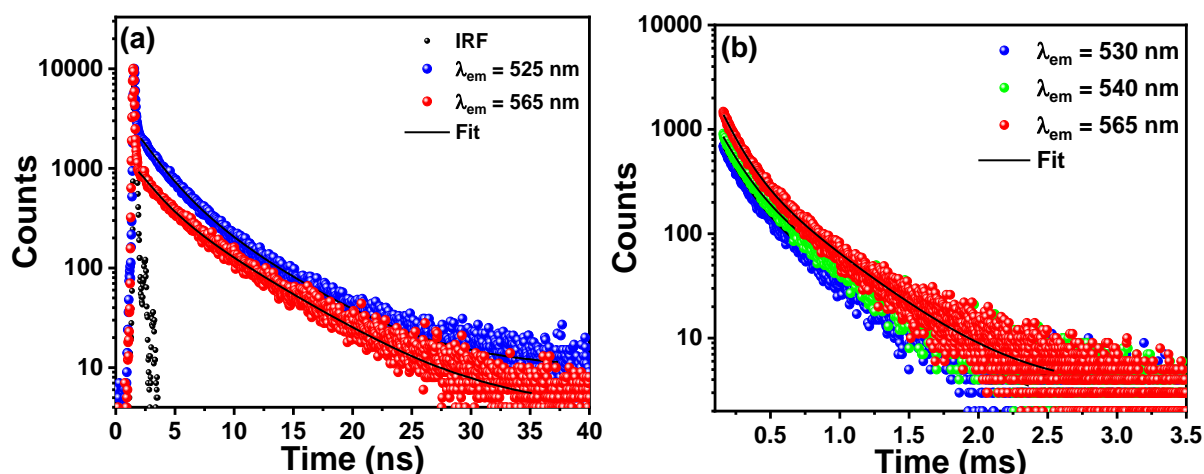
**Fig. S25** (a) Normalized emission spectra ( $\lambda_{ex} = 465$  nm) of PQTCz films with different ratios of the compound to polymer (1:40 and 1:60, w/w) and (b) emission decay profiles ( $\lambda_{ex} = 468$  nm) of PQTCz embedded in PMMA matrix with 1:40 ratio of compound to the polymer at room temperature.

**Table S10** Emission decays of PQTCz film (1:40, w/w) at different emission wavelengths; the decay times ( $\tau_1$ ,  $\tau_2$ , ns), the respective percentage contributions ( $\alpha_1$ ,  $\alpha_2$ ), and the quality of fitting ( $\chi^2$ ) are shown.

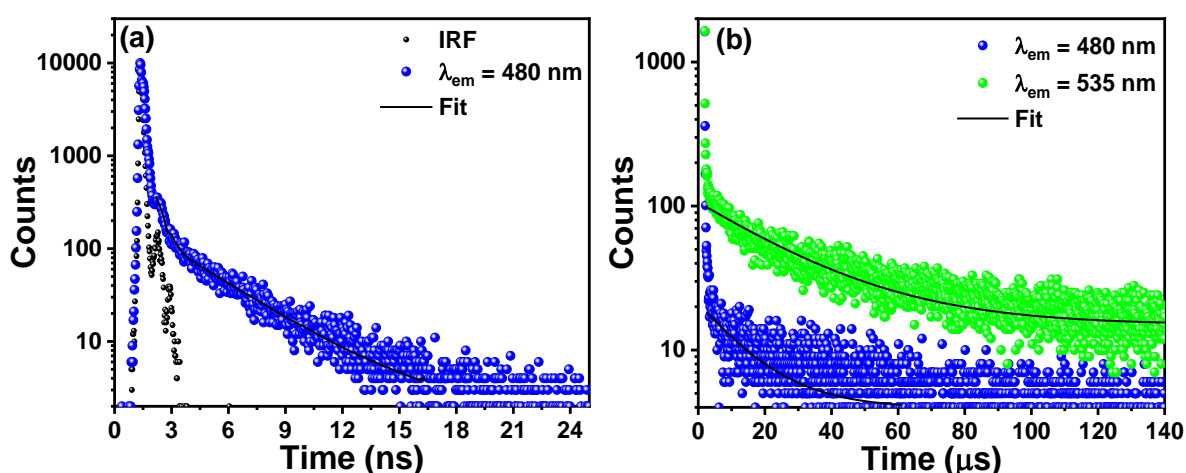
| Concentration | $\lambda_{em}$ | $\tau_1$ ( $\alpha_1$ ) | $\tau_2$ ( $\alpha_2$ ) | $\chi^2$ |
|---------------|----------------|-------------------------|-------------------------|----------|
| 1:40 (w/w)    | 570 nm         | 5.5 (16)                | 20.7 (84)               | 1.10     |
|               | 670 nm         | 8.3 (11)                | 26.7 (89)               | 1.08     |
| 1:60 (w/w)    | 570 nm         | 3.1 (22)                | 15.9 (78)               | 1.07     |
|               | 670 nm         | 0.1 (83)                | 9.2 (17)                | 1.24     |



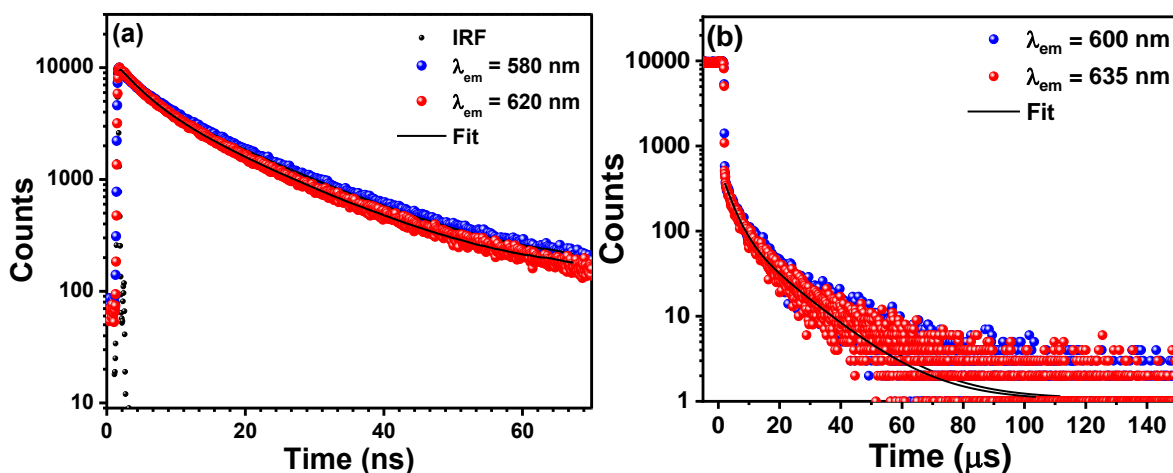
**Fig. S26** Emission decay profiles of PQTCz doped PMMA thin film in (a) nanosecond ( $\lambda_{ex} = 468$ ) and (b) microsecond ( $\lambda_{ex} = 461$  nm) timescale at ambient conditions.



**Fig. S27** Emission decay profiles of PQVCz doped PMMA thin film in (a) nanosecond ( $\lambda_{ex} = 468$ ) and (b) millisecond ( $\lambda_{ex} = 461$  nm) timescale at ambient conditions.



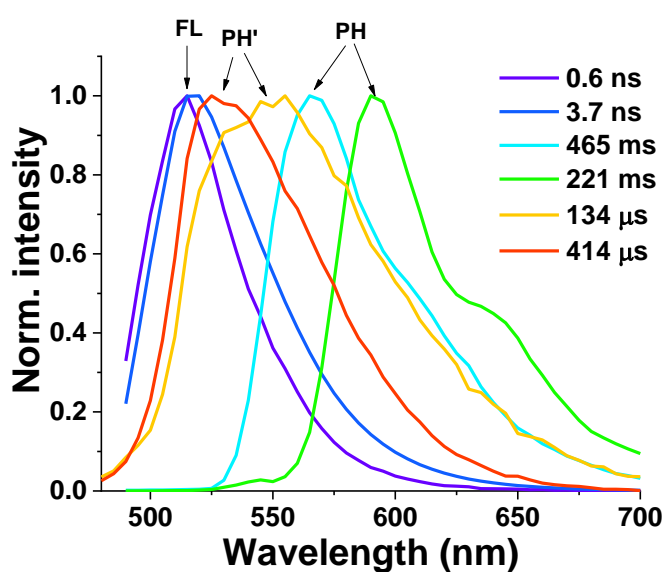
**Fig. S28** Emission decay profiles of PZVCz doped PMMA thin film in (a) nanosecond ( $\lambda_{ex} = 410$ ) and (b) microsecond ( $\lambda_{ex} = 417$  nm) timescale at ambient conditions.



**Fig. S29** Emission decay profiles of PZVPO doped PMMA thin film in (a) nanosecond ( $\lambda_{ex} = 468$ ) and (b) microsecond ( $\lambda_{ex} = 461$  nm) timescale at ambient conditions.

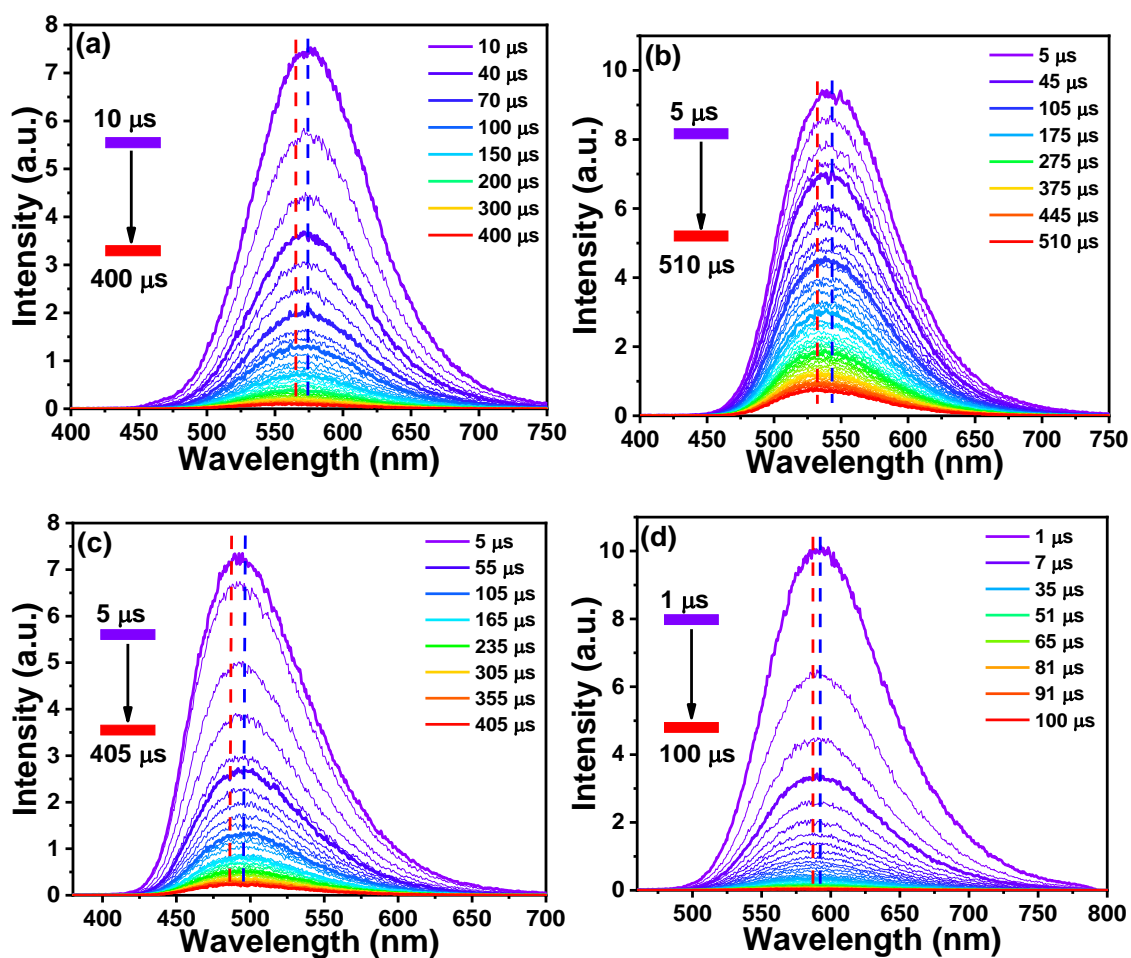
All the D<sub>3</sub>-A compounds showed a biexponential emission decay profile in polymer films at ambient conditions monitoring both in the nanosecond as well as millisecond time domain (Fig. S26-S29). Such biexponential emission decay profiles were observed presumably due to the presence of mixed LE and ICT states.

If the excited singlet state is populated from the triplet state via reverse intersystem crossing (RISC), then the radiative decay of that excited singlet state is called delayed fluorescence.<sup>1, 19</sup> TADF originates from the singlet state with charge-transfer (<sup>1</sup>CT) characteristics. Hence, it appears as a broad, structure-less Gaussian band. On the other hand, the phosphorescence is due to the direct emission from the triplet excited state (<sup>3</sup>LE or <sup>3</sup>CT). PQVCz exhibited prompt fluorescence with the peak centered at 520 nm. Whereas, it showed the phosphorescence peaks centered at 565 and 590 nm (77 K). Also, PQVCz film showed the long-lived emission at ambient conditions with the peaks centered at 530 and 550 nm. The peaks and shape of the emission spectra of PQVCz-polymer film do not coincide with either fluorescence or phosphorescence spectra. But the long-lived species in PQVCz film appear to have larger decay time compared to other D<sub>3</sub>-A compounds. We presume aggregate formation due to the rigid nature of PQVCz in PMMA films (Fig. S30).



**Fig. S30** Normalized time-resolved emission spectra of PQVCz [ $\lambda_{\text{ex.}} = 468$  nm (ps diode laser) and 461 nm (ms MCS spectraLED)] at different timescale in solution at room temperature (FL: fluorescence), 77 K (PH: phosphorescence), and in polymer film under ambient conditions (PH': phosphorescence).

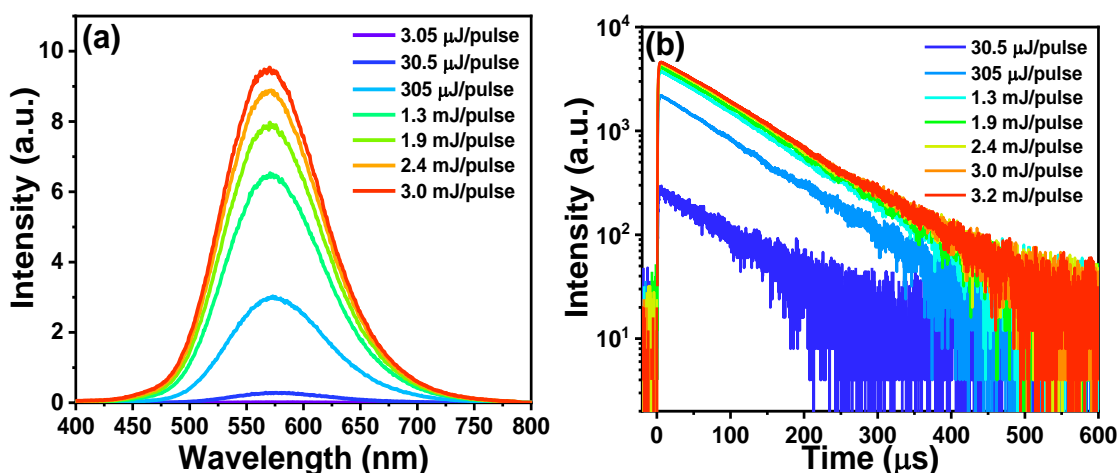




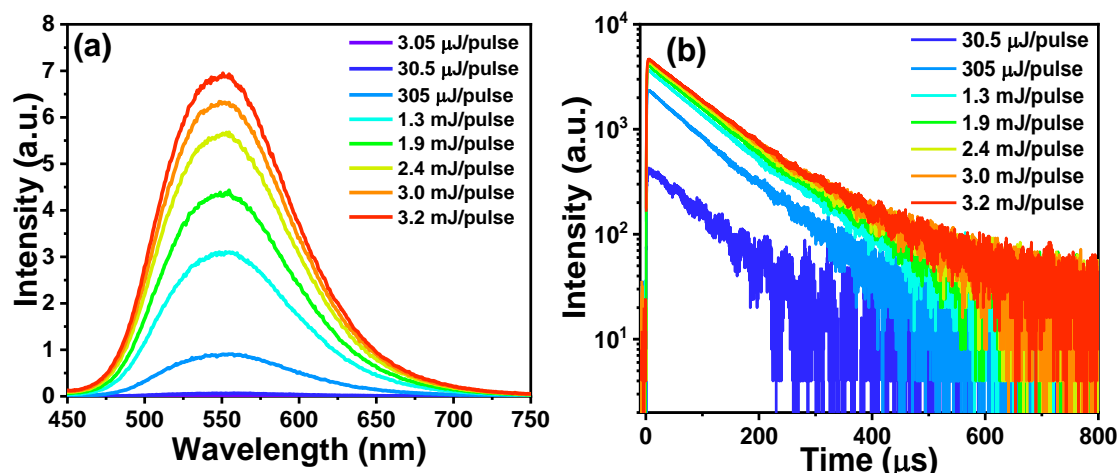
**Fig. S31** (a) Time-resolved emission spectra (TRES) of PMMA films of (a) PQTCz, (b) PQVCz, (c) PZVCz, and (d) PZVPO at ambient conditions. Spectra were recorded using an intensified charge-coupled device (iCCD) camera with tunable excitation source through optical parametric oscillators (OPO) crystal with  $\lambda_{\text{ex}} = 460$  nm for PQTCz, PQVCz and PZVPO and  $\lambda_{\text{ex}} = 420$  nm for PZVCz.

## IX. Laser power dependent study

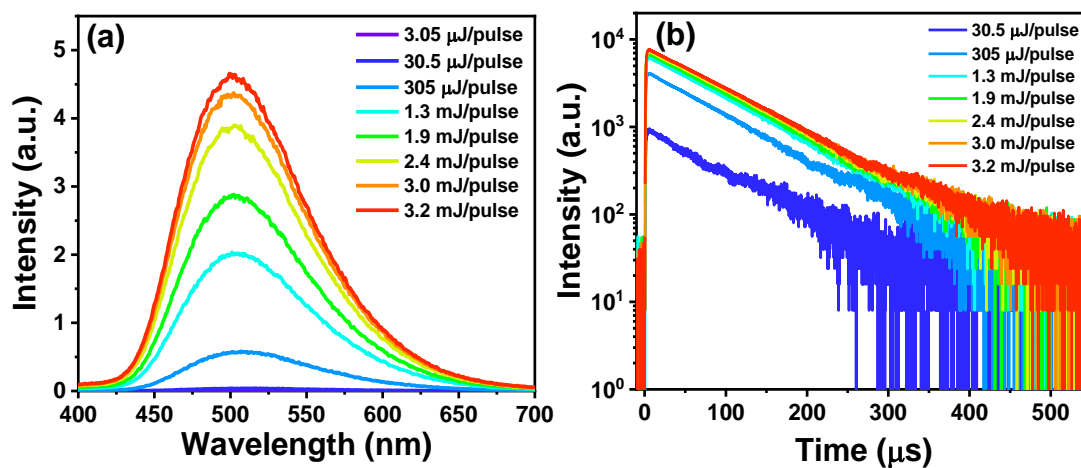
In a unimolecular and pseudo-first-order decay process, the light intensity follows a linear dependency to incident light power.<sup>28</sup> However, due to the two-sequential one photon absorptions, the upconverted photon sensitized by the triplet-triplet annihilation (TTA) process shows quadratic relation with incident light power. The laser power-dependent emission spectra using iCCD camera and the decay kinetics of the thin films for all the compounds were recorded to elucidate the long-lived components of D<sub>3</sub>-A compounds in the rigid polymer matrix (Fig. S32-S35). The emission intensity vs. laser power plots for all the compounds lead to a linear correlation, which demonstrate the unimolecular decay processes (Fig. 3c), ruling out the possibility of the triplet-triplet annihilation.



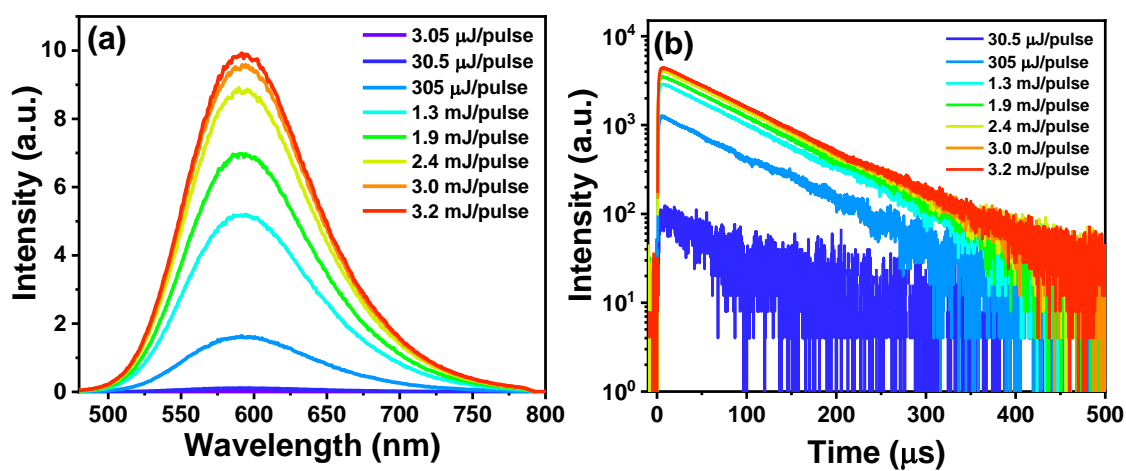
**Fig. S32** Laser power dependent (a) emission spectra ( $\lambda_{\text{ex}} = 355 \text{ nm}$ ) and (b) decay kinetics ( $\lambda_{\text{ex}} = 355 \text{ nm}$ ,  $\lambda_{\text{em}} = 570 \text{ nm}$ ) of PQTcz embedded in PMMA films at ambient conditions.



**Fig. S33** Laser power dependent (a) emission spectra ( $\lambda_{\text{ex}} = 355 \text{ nm}$ ) and (b) decay kinetics ( $\lambda_{\text{ex}} = 355 \text{ nm}$ ,  $\lambda_{\text{em}} = 550 \text{ nm}$ ) of PQVCz embedded in PMMA films at ambient conditions.



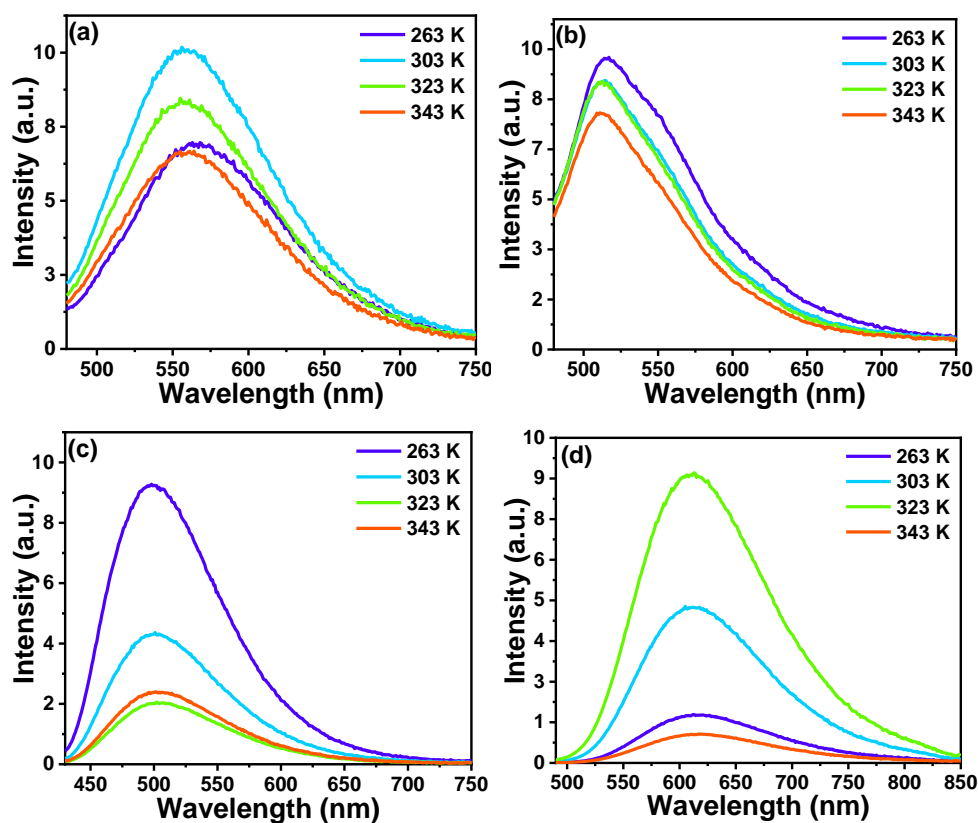
**Fig. S34** Laser power dependent (a) emission spectra ( $\lambda_{\text{ex}} = 355 \text{ nm}$ ) and (b) decay kinetics ( $\lambda_{\text{ex}} = 355 \text{ nm}$ ,  $\lambda_{\text{em}} = 520 \text{ nm}$ ) of PZVCz embedded in PMMA films at ambient conditions.



**Fig. S35** Laser power dependent (a) emission spectra ( $\lambda_{\text{ex}} = 355 \text{ nm}$ ) and (b) decay kinetics ( $\lambda_{\text{ex}} = 355 \text{ nm}$ ,  $\lambda_{\text{em}} = 590 \text{ nm}$ ) of PZVPO embedded in PMMA films at ambient conditions.

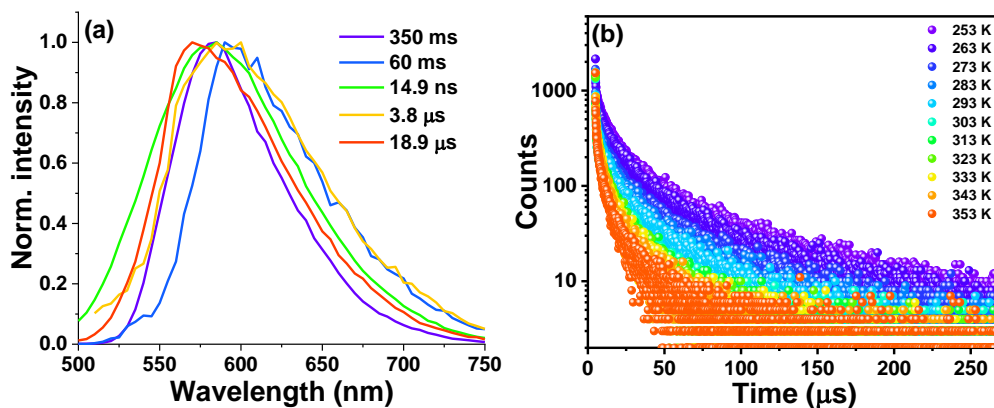
## X. Temperature-dependent decay

The harvesting of a triplet state to a singlet state becomes facile upon thermal activation. The intensity of TADF increases with increasing temperature.<sup>28</sup> In contrast, the phosphorescence involves direct emission from the triplet state. Thus, by decreasing the temperature, the quenching effect of molecular vibrations (internal conversion) is reduced, and the phosphorescence intensity is likely to increase. The temperature-dependent emission for all the D<sub>3</sub>-A compounds in PMMA thin films was carried out. An increase in the emission intensity was observed for both PQTCz and PZVPO film with increasing the temperature from 263 to 323 K confirming TADF (Fig. S36a and S36d). However, a decrease in the emission intensity was noticed at a higher temperature, *i.e.*, 343 K. The activation of the nonradiative decay channels at the higher temperature, presumably quenches the delayed fluorescence. On the other hand, a decrease in the emission was observed with increasing temperature for PQVCz and PZVCz films referring to the radiative emission from the corresponding triplet states (Fig. S36b and S36c).



**Fig. S36** Emission spectra of D<sub>3</sub>-A compounds (a) PQTCz, (b) PQVCz, (c) PZVCz, and (d) PZVPO embedded in PMMA films with varying temperature.

In order to elucidate the triplet harvesting in PZVPO further, the emission decays were collected as a function of temperature, from 253 K to 353 K. The biexponential emission decays ( $\lambda_{em} = 590$  nm) were observed. The global fitting of all the decays indicates the decay time  $\tau_1 = 9.2$   $\mu$ s and  $\tau_2 = 47$   $\mu$ s at 253 K become 2.9 and 14.9  $\mu$ s at 353 K, respectively. The temperature-dependent decays of long-lived species of PZVPO film indicate the presence of phosphorescence or radiative decay of triplet states. Whereas, the lower  $\Delta E_{ST}$  suggests the possible reverse intersystem crossing (RISC), leading to delayed emission. However, it is challenging to distinguish between TADF and RTP in the present case.



**Fig. S37** (a) Normalized emission spectra ( $\lambda_{\text{ex}} = 468$  nm for nanosecond and 461 nm for millisecond timescale) of PZVPO at different timescales in solution at room temperature (ns), 77 K (ms), and in the polymer film ( $\mu\text{s}$ ) and (b) emission decay profiles ( $\lambda_{\text{ex}} = 461$  nm,  $\lambda_{\text{em}} = 590$  nm) of PZVPO embedded in PMMA matrix with varying temperature.

**Table S11** Emission decays of PZVPO film ( $\lambda_{\text{ex}} = 461$  nm) with varying temperature; the decay times ( $\tau_1$ ,  $\tau_2$ ,  $\mu\text{s}$ ), the respective percentage contributions ( $\alpha_1$ ,  $\alpha_2$ ), and the quality of fitting ( $\chi^2$ ) are shown.

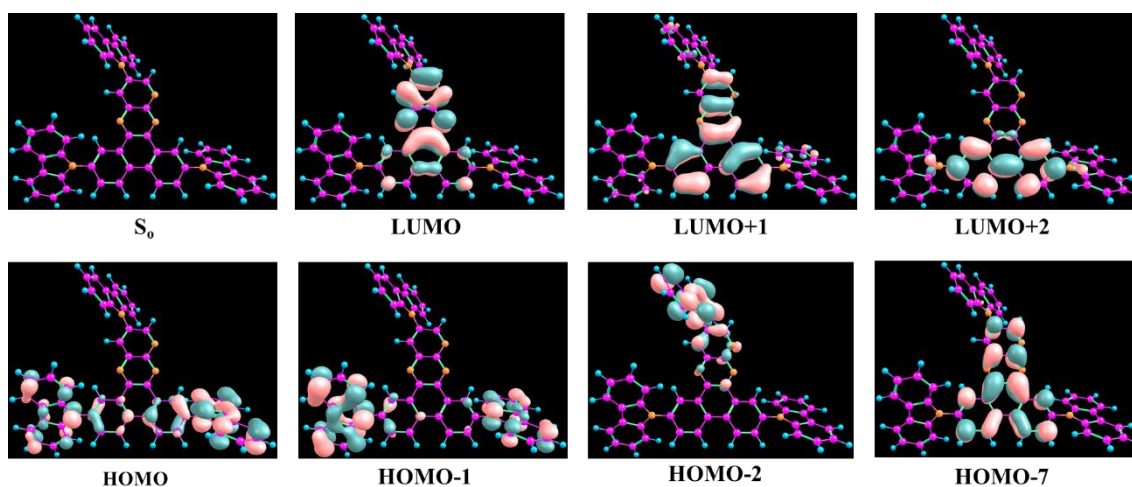
| Temperature | $\tau_1$ ( $\alpha_1$ ) | $\tau_2$ ( $\alpha_2$ ) | $\chi^2$ |
|-------------|-------------------------|-------------------------|----------|
| 253 K       | 9.2 (35)                | 47.0 (65)               | 1.2      |
| 263 K       | 7.7 (35)                | 40.2 (65)               | 1.2      |
| 273 K       | 6.8 (32)                | 35.8 (68)               | 1.21     |
| 283 K       | 6.3 (31)                | 30.3 (69)               | 1.16     |
| 293 K       | 5.9 (36)                | 29.2 (64)               | 1.14     |
| 303 K       | 5.3 (32)                | 22.7 (68)               | 1.09     |
| 313 K       | 4.2 (32)                | 19.6 (68)               | 1.19     |
| 323 K       | 3.7 (34)                | 16.9 (66)               | 1.17     |
| 333 K       | 3.2 (38)                | 16.6 (62)               | 1.15     |
| 343 K       | 3.1 (41)                | 16.1 (59)               | 1.16     |
| 353 K       | 2.9 (36)                | 14.9 (64)               | 1.13     |

## XI. Computational investigations

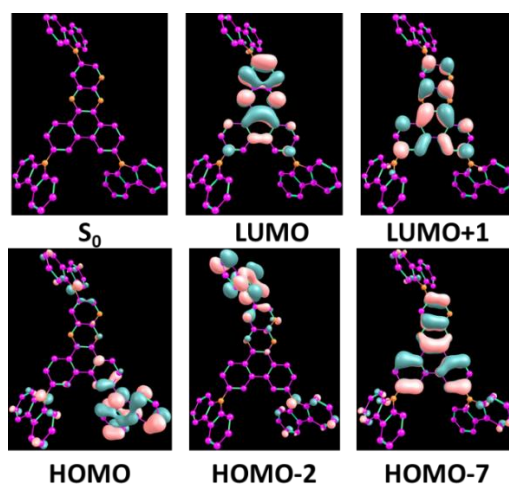
### 11.1 TDDFT Calculations:

A time-dependent density functional theory (TDDFT, spin unrestricted) investigation for all four D<sub>3</sub>-A compounds was performed using the Gaussian 16 program package.<sup>32-35</sup> The ground state molecular geometries of D<sub>3</sub>-A compounds were optimized employing density functional theory (DFT) B3LYP hybrid functional and 6-311G(d,p) basis set in Gaussian 16 Revision C.01 software.<sup>34, 35</sup> The TDDFT calculation with the same functionality and the basis set was employed to obtain the excited-state structure. The polarizable continuum model (PCM) of solvation was used to include the solvent effects.<sup>35, 36</sup> GaussView 6.0 and Chemcraft (version 1.8) were used to analyze the molecular orbitals. The iso values  $\pm 0.03$  were used for the HOMO-LUMO orbital picture, and iso values  $\pm 0.0004$  were used for electron density differences plot of singlet and triplet states. The spatial distributions of the highest occupied molecular orbital (HOMO) and the lowest unoccupied molecular orbital (LUMO) and probable electronic transitions of PQTCz, PQVCz, PZVCz, and PZVPO in the ground and the excited state were analyzed.

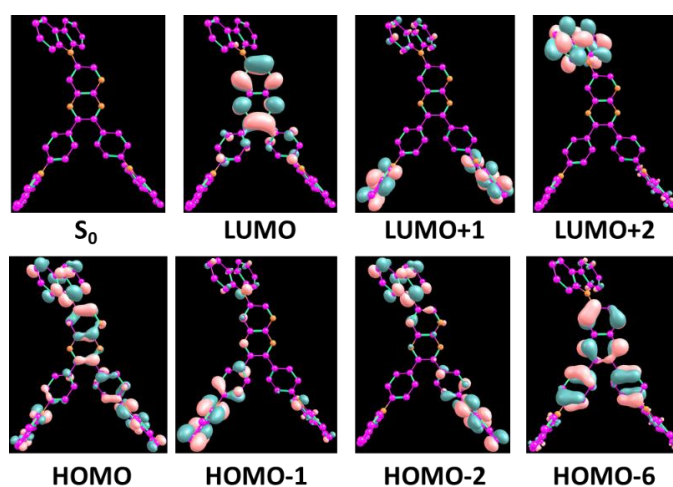
In the ground state, the LUMOs of all the compounds are predominantly located on the central pyridoquinoxaline (PQ) and pyridopyrazine (PZ) acceptor units, whereas the HOMOs are differently distributed (Fig. S38-S41). The HOMO is mainly distributed on carbazole (Cz) and phenoxazine (PO) donor units for all the compounds. However, due to the higher resonance stabilization of *p*-substituted donor molecules, like PQVCz, and PZVCz, PZVPO, the HOMO is extended to the central PQ and PZ units, respectively. The weak electron-donating character of phenanthrene leads to the localization of the HOMO on the phenanthrene unit along with carbazole for planar PQ core containing D<sub>3</sub>-A molecules. Whereas, there is no contribution towards HOMO electron density distribution by the  $\pi$ -spacer phenyl group in the twisted acceptor PZ containing D<sub>3</sub>-A molecules. The HOMO and the LUMO are well-separated accounting to the pronounce ICT characteristics in all the D<sub>3</sub>-A compounds.<sup>18</sup> The excited state geometry and the dihedral angles are shown in Table S11, S12.



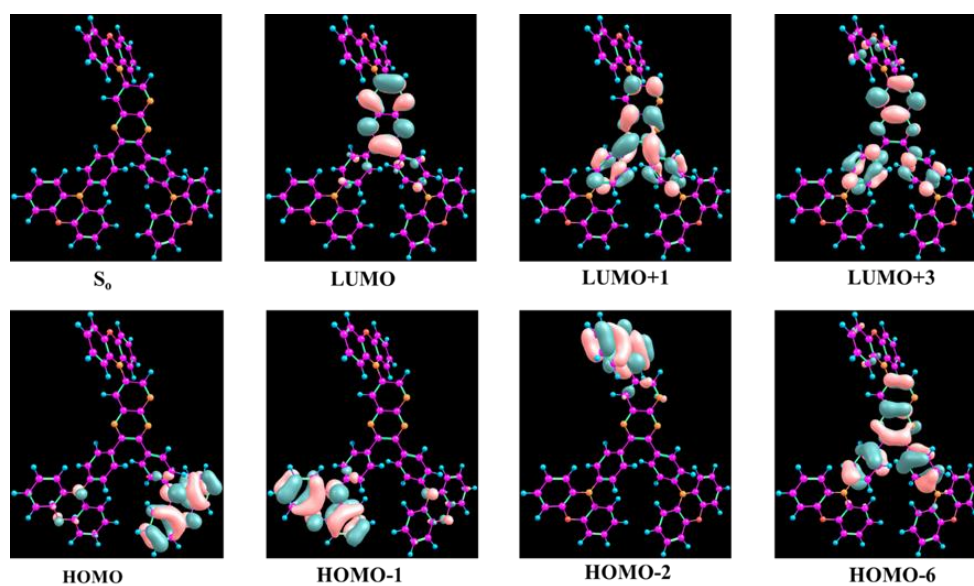
**Fig. S38** Representative molecular orbitals involved in electronic transitions revealed through TDDFT calculations for PQTCz with iso values  $\pm 0.03$ .



**Fig. S39** Representative molecular orbitals involved in electronic transitions revealed through TDDFT calculations for PQVCz with iso values  $\pm 0.03$ .

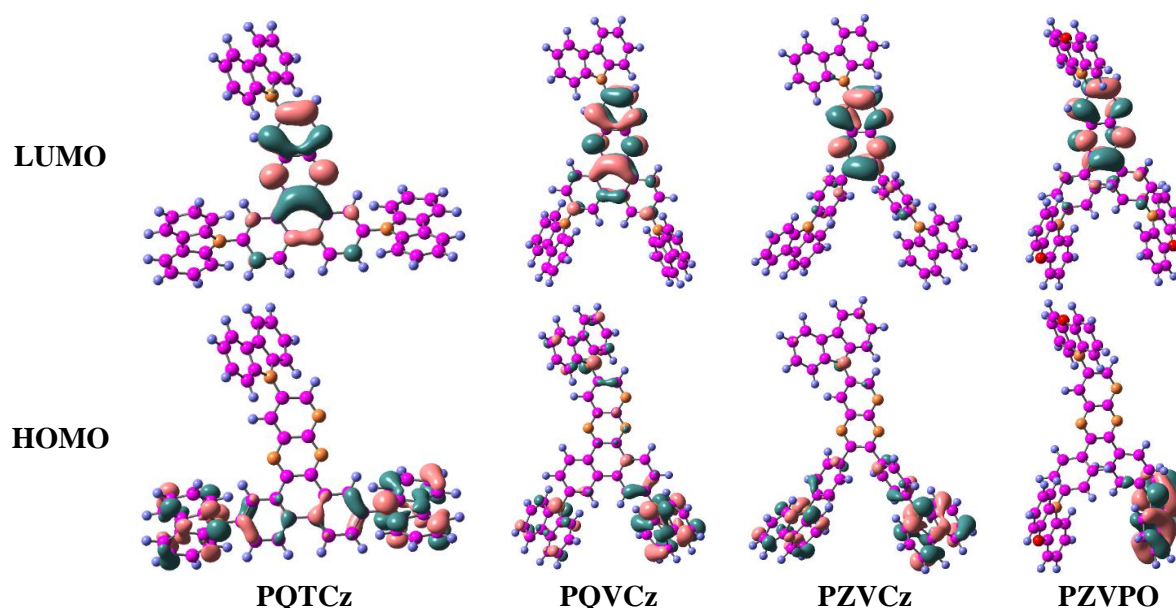


**Fig. S40** Representative molecular orbitals involved in electronic transitions revealed through TDDFT calculations for PZVCz with iso values  $\pm 0.03$ .



**Fig. S41** Representative molecular orbitals involved in electronic transitions revealed through TDDFT calculations for PZVPO with iso values  $\pm 0.03$ .

Further, we have also calculated the MOs of D<sub>3</sub>-A compounds considering diffusion correction in the basis set [6-311+G(d,p)]. There was no significant change of electron density observed with the same iso value  $\pm 0.03$  by considering the diffusion corrected basis set (Fig. S42).



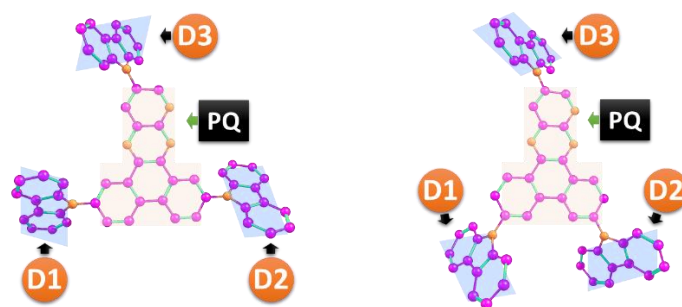
**Fig. S42** The HOMO-LUMO molecular orbital picture of D<sub>3</sub>-A compounds obtained from the DFT-B3LYP hybrid functional and 6-311+G(d,p) basis set with iso values  $\pm 0.03$ .

## 11.2 Dihedral angles:

The lower singlet-triplet energy gap ( $\Delta E_{ST}$ ) is the key for the photon upconversion from excited triplet states to the emissive singlet state through reverse intersystem crossing (RISC) leading to thermally activated delayed fluorescence (TADF).<sup>1</sup> The excited-state intramolecular charge transfer (ICT) in donor-acceptor (D-A) molecules with spatially-separated highest occupied molecular orbitals (HOMOs) and lowest unoccupied molecular orbitals (LUMOs) is conducive to a low  $\Delta E_{ST}$  value. Thus, the orthogonal geometry between the donor and acceptor leads to the lowest  $\Delta E_{ST}$  values for efficient triplet harvesting via TADF.<sup>1, 17</sup> We optimized the geometry of D<sub>3</sub>-A compounds in the excited state employing dielectric of toluene using a polarizable continuum (PCM) model. The dihedral angles in the excited state between the donor and acceptor are calculated and tabulated in Table S11 and S12. For clarity, the planar dibenzopyridoquinoxaline acceptor core is depicted as 'PQ' in the excited state geometry optimized structure of PQTCz and PQVCz. Similarly, the pyridopyrazine acceptor core is represented as PZ in the structure of PZVCz and PZVPO. The three donor units of D<sub>3</sub>-A compounds are described as D1, D2, and D3. The  $\pi$ -spacer phenyl groups in PZVCz and PZVPO are depicted as  $\pi 1$  and  $\pi 2$ .



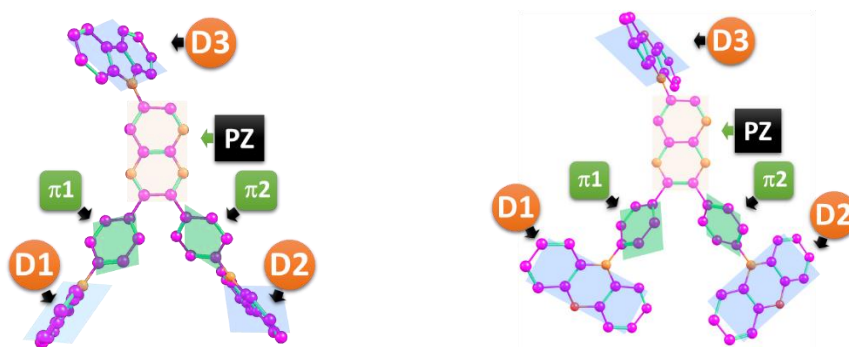
**Table S12** Dihedral angles between the donor and acceptor of PQTCz and PQVCz in the ground (GS) and excited states (ES) estimated by Gaussian B3LYP/6-311G(d,p) level calculation.



| Linkage | Dihedral angles |       |       |       |
|---------|-----------------|-------|-------|-------|
|         | PQTCz           |       | PQVCz |       |
|         | GS              | ES    | GS    | ES    |
| PQ-D1   | 123°            | 134°  | -125° | -121° |
| PQ-D2   | 123°            | 134°  | -124° | -129° |
| PQ-D3   | -127°           | -121° | -126° | -135° |

As shown in Table S11, the dihedral angle in the excited-state structure of PQTCz is 134° between PQ acceptor core and donor units (D1 and D2). Whereas, the dihedral angle between the third donor (D3) and acceptor is -121°. Thus, the twisted D-A linkages in PQTCz in the excited state lead to a low  $\Delta E_{ST}$  value, as revealed from the experimental data and theoretical calculations. PQVCz in the excited state also exhibits twisted structure. However, the lesser extent of charge transfer interactions due to the *p*-substitution of D1 and D2 leads to a comparatively higher  $\Delta E_{ST}$  than PQTCz.

**Table S13** Dihedral angles between the donor and acceptor of PZVCz and PZVPO in the ground (GS) and excited states (ES) estimated by Gaussian B3LYP/6-311G(d,p) level calculation.



| Linkage | Dihedral angles |       |         |      |
|---------|-----------------|-------|---------|------|
|         | PZVCz           |       | PZVPO   |      |
|         | GS              | ES    | Crystal | ES   |
| PZ-D1   | 98°             | 98°   | 10°     | 133° |
| PZ-D2   | -80°            | -108° | 80°     | 133° |

|             |       |       |      |       |
|-------------|-------|-------|------|-------|
| PZ-D3       | -124° | -135° | 119° | -91°  |
| PZ- $\pi$ 1 | -134° | -133° | 70°  | -140° |
| PZ- $\pi$ 2 | -135° | -156° | 138° | -143° |
| $\pi$ 1-D1  | 56°   | 57°   | 81°  | 91°   |
| $\pi$ 2-D2  | -123° | -123° | 119° | 91°   |

On the other hand, the D-A linkages involving D1 and D2 donor with PZ unit of PZVCz in the ground state is twisted in nature (Table S12). A relatively less twist was observed in the excited states. The computed  $\Delta E_{ST}$  of PZVCz was found to be 0.26 eV.

The crystal structure of PZVPO is discussed in Section XII. A more twisted and near orthogonal D-A connectivity between D3 and PZ unit was observed in the excited state for PZVPO. It could lead to the lowest  $\Delta E_{ST}$  among the mentioned D<sub>3</sub>-A compounds. Also, a smaller number of energy transition channels were observed (Fig. S43).

### 11.3 Singlet-triplet energy gap ( $\Delta E_{ST}$ ):

The energy gap between the first singlet and triplet state ( $\Delta E_{ST}$ ) was computed based on TDDFT calculation using a polarizable continuum model (PCM) for solvation (toluene) at B3LYP/ 6-311G(d,p) level.

**Table S14** TDDFT calculated excited state energy levels (eV) of singlet ( $S_n$ ) and triplet ( $T_n$ ) states and energy gap  $\Delta E_{ST}$  between the first excited singlet ( $S_1$ ) and triplet ( $T_1$ ) states of D<sub>3</sub>-A compounds. The energies of the triplet states close to  $S_1$  ( $E_{S_1} \pm 0.3$  eV) are indicated in blue.

| Energy level no. (n) | PQTCz       |                | PQVCz          |             | PZVCz          |             | PZVPO          |             |
|----------------------|-------------|----------------|----------------|-------------|----------------|-------------|----------------|-------------|
|                      | S           | T              | S              | T           | S              | T           | S              | T           |
| 1                    | <b>2.12</b> | <b>1.99</b>    | <b>2.32</b>    | <b>2.03</b> | <b>2.52</b>    | <b>2.26</b> | <b>1.68</b>    | <b>1.66</b> |
| 2                    | 2.32        | <b>2.11</b>    | 2.39           | <b>2.19</b> | 2.60           | <b>2.47</b> | 1.74           | <b>1.73</b> |
| 3                    | 2.38        | 2.29           | 2.47           | <b>2.32</b> | 2.66           | <b>2.53</b> | 1.77           | <b>1.77</b> |
| 4                    | 2.61        | 2.59           | 2.76           | 2.59        | 2.98           | <b>2.72</b> | 2.42           | 2.39        |
| $\Delta E_{ST}$      |             | <b>0.13 eV</b> | <b>0.29 eV</b> |             | <b>0.26 eV</b> |             | <b>0.02 eV</b> |             |

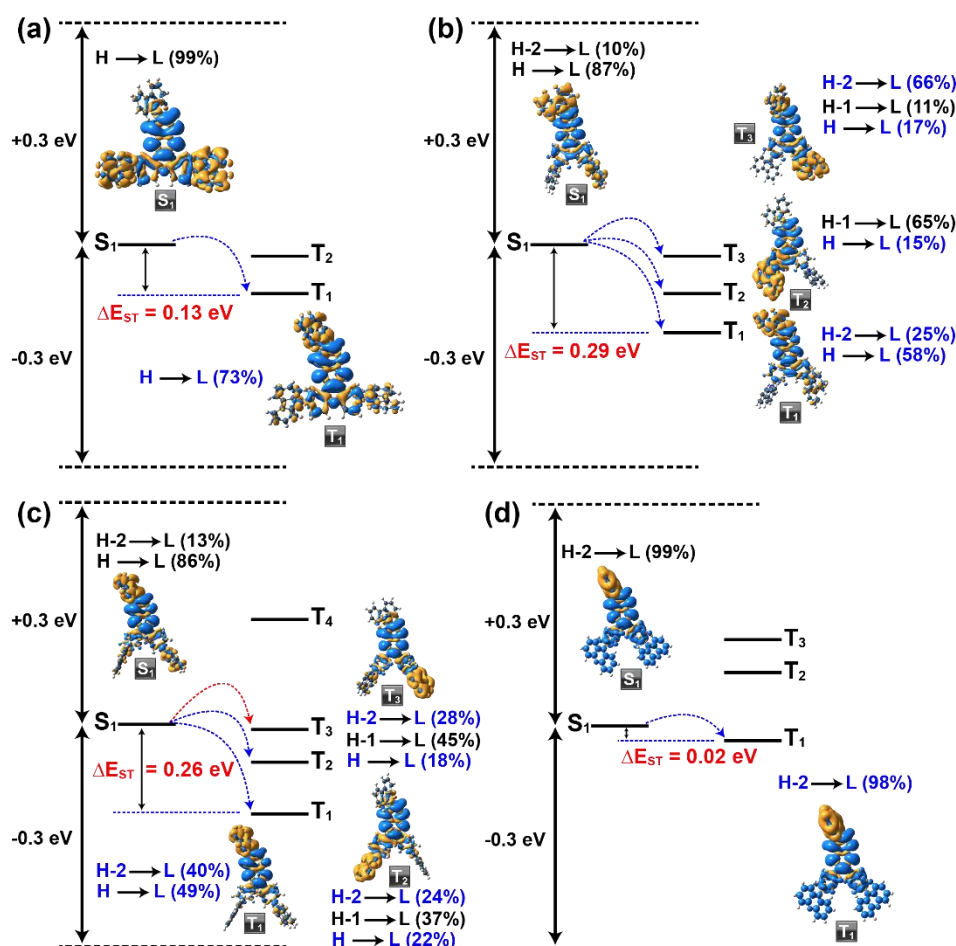
The transition configurations and electron density distributions of singlet and triplet excited states were analyzed to elucidate the possible singlet-triplet intersystem crossings (ISC) channels. The ISC channels were selected based on the same transition configurations of singlet ( $S_1$ ) and triplet ( $T_n$ ) state, and the energy levels of  $T_n$  were considered within the range of  $E_{S_1} \pm 0.3$  eV according to energy gap law.<sup>2, 37-39</sup> The electron density differences between the optimized ground state ( $S_0$ ) and the first excited singlet ( $S_0 \rightarrow S_1$ ) and the triplet state ( $S_0 \rightarrow T_n$ ) were obtained by subtracting the electron density of optimized ground state ( $S_0$ ) from that of the respective singlet and triplet excited states.<sup>35, 36</sup> The blue and yellow colors indicate the increase and decrease of electron density, respectively (Table S14, Fig.

S43). The low singlet-triplet energy gap ( $\Delta E_{ST} = 0.13$  eV) of PQTCz enables the photon upconversion from the excited triplet to the singlet state through reverse intersystem crossing (RISC) (Table S14, Fig. S43a). A single ISC channel from the  $S_1$  to the  $T_1$  of PQTCz was observed. Whereas, higher  $\Delta E_{ST}$  (0.29 eV) and a higher number of energy transition channels ( $S_1$  to  $T_1$ ,  $T_2$ , and  $T_3$ ) were observed for PQVCz (Table S14, Fig. S43b). These multiple ISC channels populate the triplet excited state through facile spin orbit coupling (SOC).

Similarly, a moderate  $\Delta E_{ST}$  (0.26 eV) along with three different energy transition channels ( $S_1$  to  $T_1$ ,  $T_2$ , and  $T_3$ ) for ISC was observed for PZVCz (Table S14, Fig. S43c). However, a very low  $\Delta E_{ST}$  (0.02 eV) and only a single ISC channel ( $S_1$  to  $T_1$ ) were obtained for PZVPO (Table S14, Fig. S43d). The facile single ISC channel, along with low  $\Delta E_{ST}$  in the case of PQTCz and PZVPO, promotes the RISC leading to TADF emission. While the multiple ISC channels in the case of PQVCz and PZVCz could populate the triplet excited state. But the higher  $\Delta E_{ST}$  and multiple reverse-ISC channels prevent the photon upconversion. The introduction of a stronger donor in PZVPO and a single ISC channel with very low  $\Delta E_{ST}$  allowed the photon upconversion from  $T_1$  to  $S_1$  state through RISC.

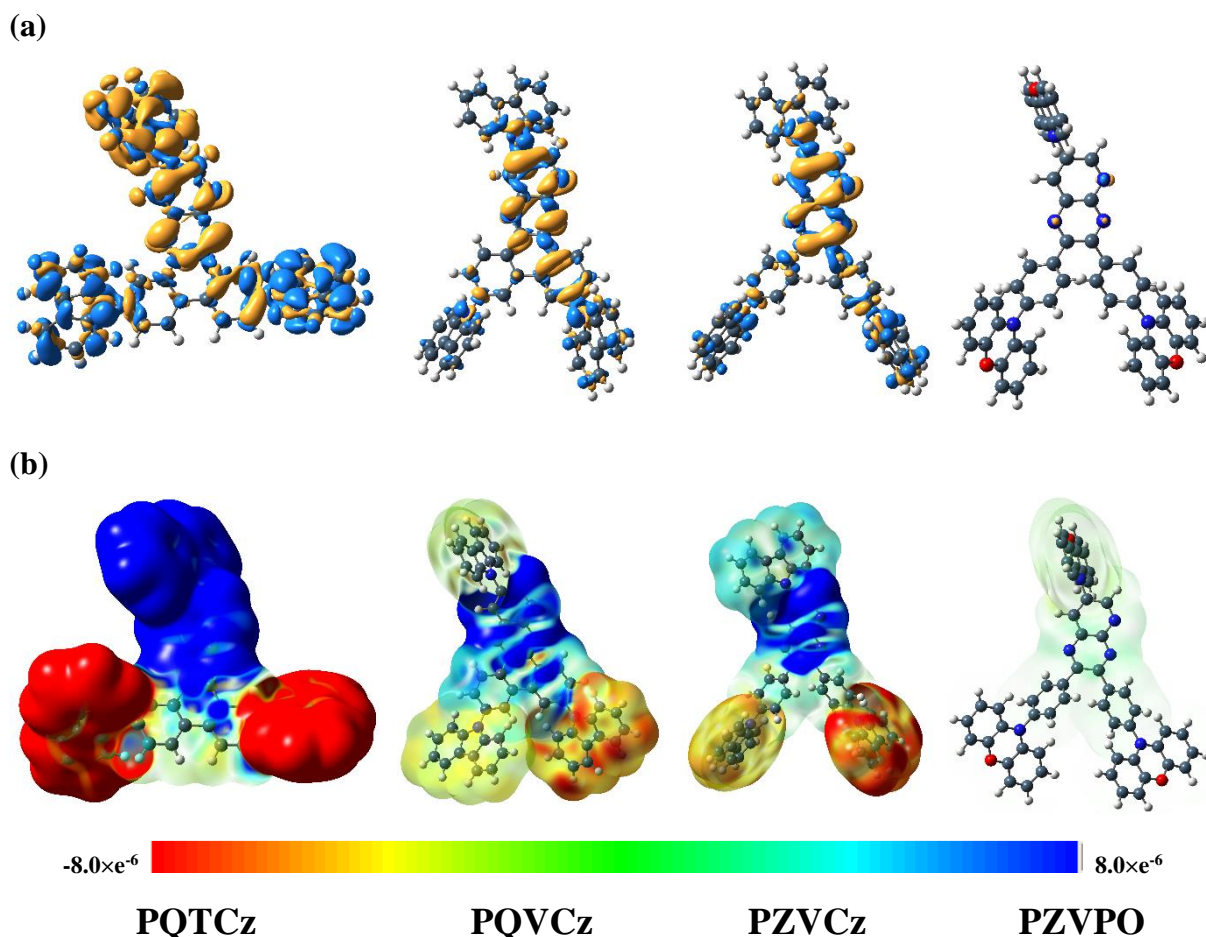
**Table S15** The singlet and triplet energy and transition configurations obtained by TDDFT calculations [B3LYP/6-311G (d,p)]. Triplet states within the energy  $E_{S_1} \pm 0.3$  eV are considered. The triplet states with the same transition configurations of  $S_1$  and  $T_n$  are highlighted in blue.

| Compound | Energy (eV) | State | Transition configurations                    |
|----------|-------------|-------|--|
| PQTCz    | 2.12        | $S_1$ | H to L (99%)                                 |
|          | 1.99        | $T_1$ | H to L (73%)                                 |
|          | 2.11        | $T_2$ | H-2 to L (72%)                               |
| PQVCz    | 2.32        | $S_1$ | H-2 to L (10%), H to L (87%)                 |
|          | 2.03        | $T_1$ | H-2 to L (25%), H to L (58%)                 |
|          | 2.19        | $T_2$ | H-1 to L (65%), H to L (15%)                 |
|          | 2.32        | $T_3$ | H-2 to L (66%), H-1 to L (11%), H to L (17%) |
| PZVCz    | 2.52        | $S_1$ | H-2 to L (13%), H to L (86%)                 |
|          | 2.26        | $T_1$ | H-2 to L (40%), H to L (49%)                 |
|          | 2.47        | $T_2$ | H-2 to L (24%), H-1 to L (37%), H to L (22%) |
|          | 2.53        | $T_3$ | H-2 to L (28%), H-1 to L (45%), H to L (18%) |
|          | 2.72        | $T_4$ | H-7 to L (74%)                               |
| PZVPO    | 1.68        | $S_1$ | H-2 to L (99%)                               |
|          | 1.66        | $T_1$ | H-2 to L (98%)                               |
|          | 1.73        | $T_2$ | H to L (99%)                                 |
|          | 1.77        | $T_3$ | H-1 to L (99%)                               |

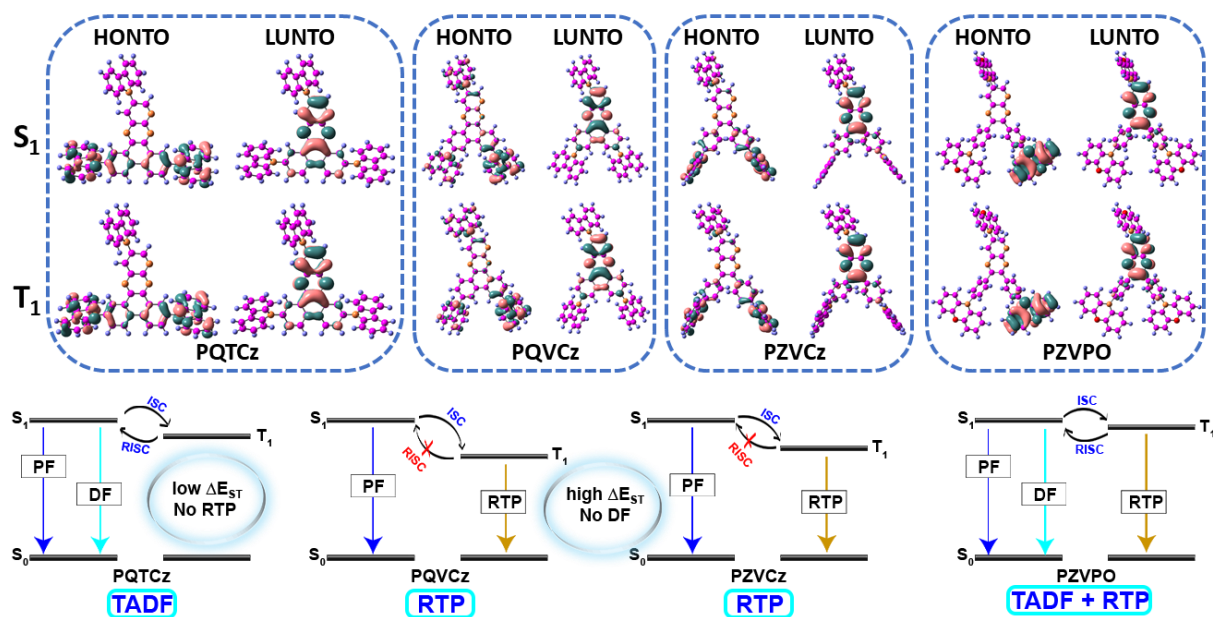


**Fig. S43** Schematic diagrams showing the TDDFT calculated [B3LYP/6-311G(d,p)] energy levels, isosurface of electron density differences in the S<sub>1</sub> and T<sub>n</sub> states, possible intersystem crossing (ISC) channels (considering E<sub>S1</sub> ± 0.3 eV according to energy gap law) of (a) PQTCz, (b) PQVCz, (c) PZVCz, and (d) PZVPO. H and L represent the highest occupied molecular orbital (HOMO) and the lowest unoccupied molecular orbital (LUMO), respectively. The triplet states with same transition configurations of S<sub>1</sub> are highlighted in blue. The values of S<sub>1</sub>-T<sub>1</sub> energy gaps (ΔE<sub>ST</sub>) are indicated.

The electron density differences between the first excited singlet state and the triplet state were plotted (Fig. S44a).<sup>36</sup> The blue and yellow area plots are the surface where the value of the difference density is +0.0004 and -0.0004, respectively. Electron density shifts from the blue region to the yellow region upon transit from the S<sub>1</sub> to the T<sub>1</sub> state. As shown in Fig. S44a, the electron density in the singlet state is distributed on the donor part, and the triplet state is located on the acceptor part for PQTCz, PQVCz, and PZVCz. Additionally, for PQTCz, the triplet state is extended up to the third donor unit (D3). Whereas, no such electron density differences were observed for PZVPO. This can be due to the fact that the singlet and triplet are distributed throughout the molecule in PZVPO. The map of electron density isosurface of the first singlet excited state (S<sub>1</sub>) with respect to S<sub>1</sub>-T<sub>1</sub> electron density differences are shown in Fig. S44b. The blue and red regions in Fig. S44b indicate the higher electron density in T<sub>1</sub> in comparison with S<sub>1</sub> and vice versa.



**Fig. S44** (a) Plots of electron density differences between first singlet ( $S_1$ ) and triplet ( $T_1$ ) excited states as an isosurface having a density value  $\pm 0.0004$ . The electron density shifts from the orange region to the cyan region while transition from  $S_1$  to  $T_1$  states. (b) Electron density isosurface of  $S_1$  mapped using the value of difference density between  $S_1$  and  $T_1$ . The blue region indicates that the electron density in  $T_1$  is higher than that of the  $S_1$ .

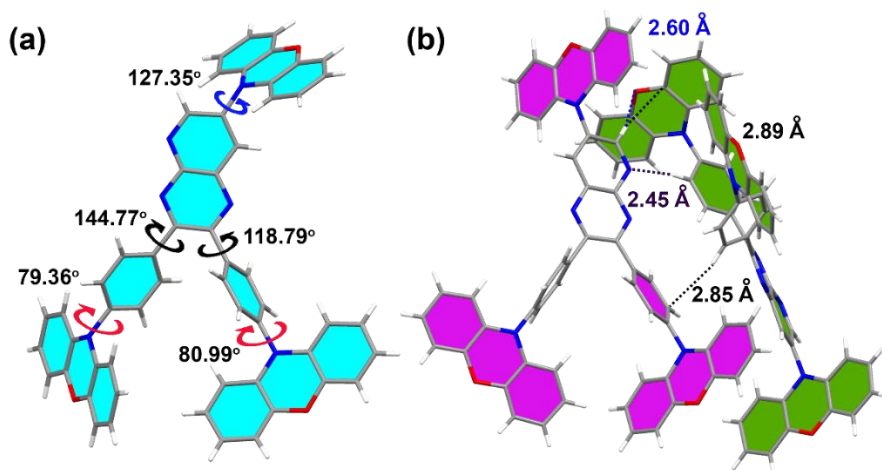


**Fig. S45** The impact of the frontier molecular orbital (FMOs) on triplet energies. The highest occupied natural transition orbitals (HONTOs) and the lowest unoccupied natural transition orbitals (LUNTOs) of singlet ( $S_1$ ) and triplet ( $T_1$ ) states with iso values  $\pm 0.03$  of  $D_3$ -A compounds are given in the upper panel. The respective long-lived decay pathways of  $D_3$ -A compounds are shown in the lower panel.

Further, the natural transition orbital (NTO) analysis was carried to know more about the excited-state electronic transitions.<sup>40</sup> There was no direct overlap between the highest occupied natural transition orbitals (HONTOs) and the lowest unoccupied natural transition orbitals (LUNTOs) of D<sub>3</sub>-A molecules at singlet (S<sub>1</sub>) and triplet (T<sub>1</sub>) states. This is indicating all the molecules are exhibiting excited-state charge transfer property, and the energy gap between the S<sub>1</sub> and T<sub>1</sub> states are below <0.5 eV. The LUNTOs of all the compounds are predominantly located on the acceptor cores, such as PQ and PZ units. Whereas HONTOs mainly located at donor units. The excited state D-A dihedral angles are given in Table S12 and S13. When the dihedral angle is close to 90°, the overlap between D and A units are quite small, which will induce small ΔE<sub>ST</sub>. Based on our experimental results and geometric parameters, we found that the donor groups have a significant influence on the relative orientations of D and A units. Thus, the introduction of the strong PO donor leads to more twisted structure, and small ΔE<sub>ST</sub> is observed in PZVPO as compared to Cz based molecules.

## XII. Crystal structure analysis

Crystals of PZVPO were grown from a mixture of dichloromethane and ethanol through a slow evaporation method. Single-crystal X-ray diffraction data were collected using a Bruker APEX II diffractometer equipped with a CCD area detector using Mo K $\alpha$  radiation ( $\lambda = 0.71073 \text{ \AA}$ ) in phi( $\phi$ ) and omega( $\omega$ ) scan.<sup>41</sup> The data collections for PZVPO was carried out at 140 K, giving an exposure time of 15 seconds per frame at the crystal to-detector distance of 6 cm. The data collection, unit cell measurements, integration, scaling and absorption corrections were done using Bruker Smart Apex II software.<sup>41</sup> The intensity data were processed by using the Bruker SAINT Program suite.<sup>42</sup> The crystal structures were refined by the full-matrix least-squares method using SHELXL97 present in the program suite WinGX (version2014.1).<sup>43-47</sup> Empirical absorption correction was applied using SADABS,<sup>48</sup> and the crystal packing diagrams were generated using Mercury 4.2.0,<sup>49</sup> and Materials Studio 6.1. The detailed crystallographic data and the structure refinement parameters are summarized in Table S15.



**Fig. S46** The molecular structures obtained from the crystal structure investigations of PZVPO showing (a) twisted molecular structure and (b) crystal packing along  $b$ -direction based on weak intermolecular interactions.

The single crystals of PZVPO belong to the centrosymmetric space group  $P\bar{1}$  with 2 molecules in the asymmetric unit cell. The molecular structure of PZVPO obtained from crystal structure analysis revealed a highly twisted structure. As depicted in Table S12, the dihedral angles between the central pyridopyrazine (PZ) core and the phenyl linker groups ( $\pi_1$  and  $\pi_2$ ) are  $70^\circ$  and  $138^\circ$  while the dihedral angle between the  $\pi$ -spacers and phenoxazine donor units are  $81^\circ$  ( $\pi_1$ -D1) and  $119^\circ$  ( $\pi_2$ -D2). On the other hand, the donor group connected directly to the acceptor core (PZ-D3) exhibits a dihedral angle of  $119^\circ$  (Fig. S46a, Fig. 3d, main text). Thus, the molecular geometry of PZVPO is significantly non-planar in nature. Additionally, a pair of  $\text{CH}\cdots\pi$  ( $2.84 \text{ \AA}$ ) and  $\text{CH}\cdots\text{HC}$  ( $2.32 \text{ \AA}$ ) intermolecular interactions between  $\pi$ -spacer phenyl groups generate a dimer like twisted structure along  $a$  axis and a pair of  $\text{CH}\cdots\pi$  interactions ( $2.86 \text{ \AA}$ ) between the  $\pi$ -spacer phenyl and donor phenoxazine stabilize the dimeric structure (Fig. 3e, main text). Additional  $\text{CH}\cdots\pi$  ( $2.77, 2.81 \text{ \AA}$ ) and  $\text{CH}\cdots\text{O}$  ( $2.63 \text{ \AA}$ ) interactions between  $\pi$ -spacer aromatic phenyl and phenoxazine are observed. As shown in Fig. S46b, the asymmetric unit cell of PZVPO contains multiple intermolecular interactions, such as  $\text{CH}\cdots\pi$  ( $2.89 \text{ \AA}$ ) between the aromatic hydrogen of PZ acceptor unit and  $\pi$ -electron of phenoxazine donor,  $\text{CH}\cdots\pi$  ( $2.85 \text{ \AA}$ ) between the aromatic  $\pi$ -spacer units of two adjacent molecules,  $\text{CH}\cdots\text{O}$  ( $2.60 \text{ \AA}$ ) between the aromatic hydrogen of PZ acceptor

unit and oxygen of phenoxazine donor, and CH $\cdots$ N (2.45 Å) between the aromatic nitrogen of PZ acceptor unit and CH of the  $\pi$ -spacer phenyl. These multiple intermolecular interactions lead to a twisted dimeric structure without any significant  $\pi\cdots\pi$  stacking interactions. Thus, the twisted structure and strong intermolecular interactions in the crystals of PZVPO could reduce the energy loss through non-radiative relaxation channels by the stabilization of excited triplet states.<sup>50-52</sup>

**Table S16** Crystallographic data of PZVPO.

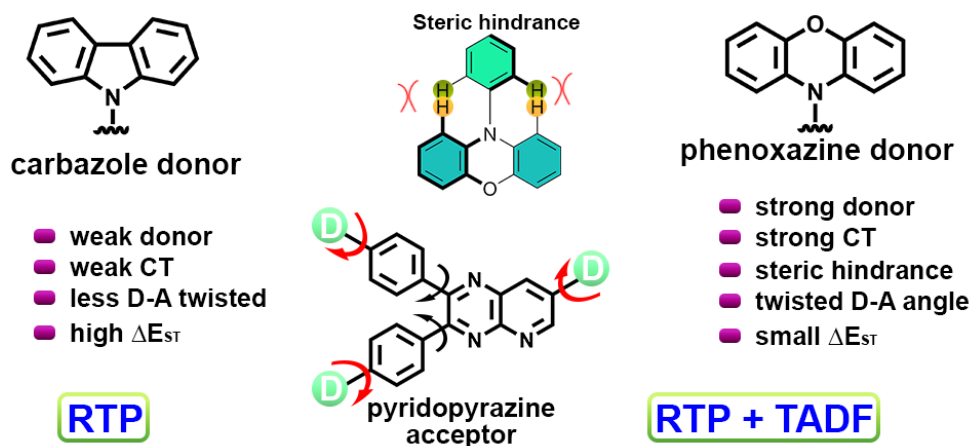
| Parameters                        | PZVPO  |
|-----------------------------------|--|
| Empirical formula                 | C <sub>55</sub> H <sub>34</sub> N <sub>6</sub> O <sub>3</sub>  |
| Formula Weight                    | 826.88   |
| Temperature                       | 140 K  |
| Wavelength                        | 0.71073  |
| Crystal system                    | Triclinic  |
| Space group                       | <i>P</i> $\bar{1}$   |
| Unit-cell dimension               | a = 12.05890(14), b = 18.638(2), c = 19.646(2),<br>$\alpha$ = 65.738(8), $\beta$ = 89.704(8), $\gamma$ = 84.778(7) |
| Volume                            | 4006.2(8)  |
| Z                                 | 4  |
| Density                           | 1.371 g cm <sup>-3</sup>   |
| Absorption coefficient            | 0.087 mm <sup>-1</sup>   |
| F(000)                            | 1720.0   |
| Crystal size                      | 0.3 × 0.2 × 0.1  |
| Theta range for data collection   | 1.1 to 25.0°   |
| Index ranges                      | -14 ≤ h ≤ 14, -22 ≤ k ≤ 22, -23 ≤ l ≤ 23   |
| Reflections collected             | 56053  |
| No. of unique Ref./ obs. Ref.     | 14139  |
| Data completeness                 | 0.997  |
| Absorption correction             | Multi scans  |
| Max. and min. transmission        | 0.991 and 0.979  |
| Refinement method                 | Full-matrix least-squares on F <sup>2</sup>  |
| No. of parameters                 | 1155   |
| Goodness-of-fit on F <sup>2</sup> | 1.019  |
| Final R indices [I > 2σI]         | R1 = 0.1161 and wR2 = 0.3258   |
| R indices (all data)              | R1 = 0.144 and wR2 = 0.295   |
| Largest diff. peak and hole       | 0.812 and -0.479   |
| <a href="#">CCDC Number</a>       | <a href="#">CCDC 1904506</a>   |

### PZVCz vs. PZVPO:

PZVCz prominently absorbed at  $\lambda_{\text{abs}} = 320$  and 425 nm along with a hump at  $\lambda_{\text{abs}} = 340$  nm. Whereas PZVPO exhibited two distinct absorption bands centered at  $\lambda_{\text{abs}} = 330$  and 465 nm. Similarly, PZVPO showed emission in the lower energy region as compared to PZVCz. A comparatively higher Stokes shift of 5245 cm<sup>-1</sup> was observed for PZVPO as compared to 2996 cm<sup>-1</sup> for PZVCz in toluene. A relatively weak emission band at  $\lambda_{\text{em}} = 610$  nm was noticeable for PZVPO in toluene at room temperature due to strong D-A pair leading to the dark TICT state. The emission data indicate the more facile charge transfer in PZVPO as compared to that in PZVCz. The crystal structure investigations of PZVPO indicate the twisted molecular geometry (Table S13). Additionally, the DFT-optimized excited-state structure of both PZVCz and PZVPO revealed the twisted nature. As depicted in Table S13, a partial twist in the excited-state



structure of PZVCz with the dihedral angles  $57^\circ$ ,  $-123^\circ$ , and  $-135^\circ$  was observed for  $\pi 1$ -D1,  $\pi 2$ -D2, and PZ-D3, respectively. Whereas a more twisted and near orthogonal D-A geometry was observed for PZVPO in the excited state with the dihedral angles  $91^\circ$ ,  $91^\circ$ , and  $-91^\circ$  for  $\pi 1$ -D1,  $\pi 2$ -D2, and PZ-D3, respectively. Even though both the compounds are non-planar, but the strong charge transfer interactions result in more twist in the case of PZVPO. A very low  $\Delta E_{ST}$  (0.02 eV) was observed for PZVPO as compared to PZVCz ( $\Delta E_{ST} = 0.26$  eV).

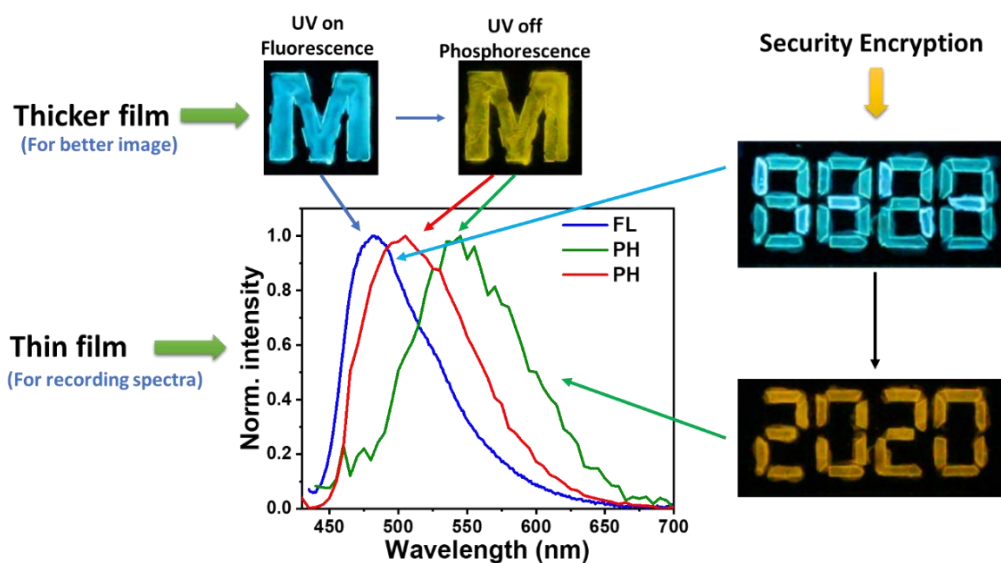


**Scheme S7** A schematic illustration of comparative features in terms of donor units carbazole and phenoxazine, respectively, in PZVCz and PZVPO.

Our observations and explanations can be justified by a few reported works. Adachi and coworkers achieved twisted molecular geometry with TADF emission by the stabilization of the ICT state between a phenoxazine donor and 2,4,6-triphenyl-1,3,5-triazine acceptor unit.<sup>53</sup> However, Huang and coworkers observed ultralong phosphorescence using carbazole as a donor.<sup>40,54,55</sup> The large twist angle in phenoxazine based D-A pair as compared to carbazole donor in dimesitylphenylborane acceptor core was reported by Oi and coworkers.<sup>56,57</sup> They found the introduction of the strong donor phenoxazine led to more twisted structure and small  $\Delta E_{ST}$  as compared to carbazole based molecules. Further, the twisted structure of PZVPO is due to the steric hindrance of the hydrogen atoms at 1- and 9-positions of phenoxazine (Scheme S7).<sup>57</sup> Whereas, the steric factor is less effective in the case of hydrogens at 1- and 8-positions of carbazole in PZVCz. Thus, the stronger electron donating ability and the higher steric hindrance from the hydrogens at 1- and 9-positions of the phenoxazine unit, lead to more twist in PZVPO than weak donor carbazole in PZVCz. Consequently, a lower  $\Delta E_{ST}$  was observed for PZVPO. Whereas, a relatively large  $\Delta E_{ST}$  was observed for PZVCz.

### XIII. Security Encryption

In order to illustrate the potential applications for security data encryption, we fabricated the PZVCz (fluorescence at  $\lambda_{em} = 480$  nm and phosphorescence at  $\lambda_{em} = 500-600$  nm) embedded film in PMMA matrix.<sup>29, 31, 58</sup> The homogeneous and transparent thin films were fabricated on a quartz plate using a spin-coater for spectral measurements. However, a relatively thicker film or security mark was fabricated on a quartz plate by drop-casting method for better clarity of visual impressions. As mentioned in Fig. 4e and Fig. S47, the spectra were recorded for thin films, and the digital photographs were taken using a thicker film. The photographs were collected using Canon EOS camera ( $f/4.6-9.0$ , Focal length: 18-55 mm, ISO Speed: 100-6400, Color Space: sRGB, Sensor type: CMOS, Shutter speed: 30-1/4000 sec, 50 fps at 720p) and Realme 5 Pro.



**Fig. S47** Demonstration of time-resolved emission spectra (TRES) measured with thin and digital photographs and security encryption with thick PZVCz-PMMA films.

## XIV. Summary

A comparative account of photophysical features of D<sub>3</sub>-A compounds is shown in Table S16 and Fig. 4a-d. The harvesting of the triplet states through TADF and RTP emission by tweaking the charge transfer interactions is mentioned here.

**Table S17** A comparative account of salient structural and spectral characteristics of D<sub>3</sub>-A compounds investigated.

| Parameter                                 | PQTCz            | PQVCz            | PZVCz                | PZVPO                |
|---|------------------|------------------|----------------------|----------------------|
| $\pi$ -spacer (acceptor)                  | Planar and rigid | Planar and rigid | Twisted and flexible | Twisted and flexible |
| Donor substitution                        | <i>meta</i>      | <i>para</i>      | <i>para</i>          | <i>para</i>          |
| Stokes shift (cm <sup>-1</sup> , toluene) | 3976             | 2210             | 2996                 | 5245                 |
| CT interaction                            | Strong           | Weak             | Moderate             | Strongest            |
| $\Delta E_{ST}$ (eV, computed)            | 0.13             | 0.29             | 0.26                 | 0.02                 |
| Outcome                                   | TADF             | RTP              | RTP                  | TADF + RTP           |

## XV. References

1. H. Uoyama, K. Goushi, K. Shizu, H. Nomura and C. Adachi, *Nature*, 2012, **492**, 234.
2. Z. Y. Yang, Z. Mao, X. P. Zhang, D. P. Ou, Y. X. Mu, Y. Zhang, C. Y. Zhao, S. W. Liu, Z. G. Chi, J. R. Xu, Y. C. Wu, P. Y. Lu, A. Lien and M. R. Bryce, *Angew. Chem. Int. Ed.*, 2016, **55**, 2181-2185.
3. C. J. Chen, R. J. Huang, A. S. Batsanov, P. Pander, Y. T. Hsu, Z. G. Chi, F. B. Dias and M. R. Bryce, *Angew. Chem. Int. Ed.*, 2018, **57**, 16407-16411.
4. P. Stachelek, J. S. Ward, P. L. Dos Santos, A. Danos, M. Colella, N. Haase, S. J. Raynes, A. S. Batsanov, M. R. Bryce and A. P. Monkman, *ACS Appl. Mater. Interfaces*, 2019, **11**, 27125-27133.
5. F. B. Dias, K. N. Bourdakos, V. Jankus, K. C. Moss, K. T. Kamtekar, V. Bhalla, J. Santos, M. R. Bryce and A. P. Monkman, *Adv. Mater.*, 2013, **25**, 3707-3714.
6. J. S. Ward, R. S. Nobuyasu, A. S. Batsanov, P. Data, A. P. Monkman, F. B. Dias and M. R. Bryce, *Chem. Commun.*, 2016, **52**, 2612-2615.
7. J. S. Ward, R. S. Nobuyasu, M. A. Fox, J. A. Aguilar, D. Hall, A. S. Batsanov, F. B. Dias, M. R. Bryce and Z. Ren, *J. Org. Chem.*, 2019, **84**, 3801-3816.
8. J. Chen, W. Tao, Y. Xiao, K. Wang, M. Zhang, X. Fan, W. Chen, J. Yu, S. Li, F. Geng, X. Zhang and C. Lee, *ACS Appl. Mater. Interfaces*, 2019, **11**, 29086-29093.
9. R. Furue, K. Matsuo, Y. Ashikari, H. Ooka, N. Amanokura and T. Yasuda, *Adv. Opt. Mater.* 2018, **6**, 1701147.
10. S. Wang, Y. Miao, X. Yan, K. Ye and Y. Wang, *J. Mater. Chem. C*, 2018, **6**, 6698-6704.
11. R. Pashazadeh, P. Pander, A. Bucinskas, P. J. Skabara, F. B. Dias and J. V. Grazulevicius, *Chem. Commun.*, 2018, **54**, 13857-13860.
12. T. Huang, D. Liu, J. Jiang and W. Jiang, *Chem. Eur. J*, 2019, **25**, 10926-10937.
13. G. Gokce, B. Karabay, A. Cihaner and M. Icli Ozkut, *J. Polym. Sci. Part A: Polym. Chem.*, 2017, **55**, 3483-3493.
14. P. Data, P. Pander, M. Okazaki, Y. Takeda, S. Minakata and A. P. Monkman, *Angew. Chem. Int. Ed.*, 2016, **55**, 5739-5744.
15. M. Okazaki, Y. Takeda, P. Data, P. Pander, H. Higginbotham, A. P. Monkman and S. Minakata, *Chem. Sci.*, 2017, **8**, 2677-2686.
16. P. Data, M. Okazaki, S. Minakata and Y. Takeda, *J. Mater. Chem. C*, 2019, **7**, 6616-6621.
17. Y. Im, M. Kim, Y. J. Cho, J.-A. Seo, K. S. Yook and J. Y. Lee, *Chem. Mater.*, 2017, **29**, 1946-1963.
18. B. Sk, S. Khodia and A. Patra, *Chem. Commun.*, 2018, **54**, 1786-1789.
19. J. R. Lakowicz, *Principles of fluorescence spectroscopy*, Springer, New York, 2006.
20. L. A. Estrada and D. C. Neckers, *Org. Lett.*, 2011, **13**, 3304-3307.
21. Z. R. Grabowski, K. Rotkiewicz and W. Rettig, *Chem. Rev.*, 2003, **103**, 3899-4032.
22. C. Reichardt, *Chem. Rev.*, 1994, **94**, 2319-2358.

23. K. Rurack and M. Spieles, *Anal. Chem.*, 2011, **83**, 1232-1242.
24. C. Wurth, M. Grabolle, J. Pauli, M. Spieles and U. Resch-Genger, *Nat. protocol.*, 2013, **8**, 1535-1550.
25. T. Suhina, S. Amirjalayer, B. Mennucci, S. Woutersen, M. Hilbers, D. Bonn and A. M. Brouwer, *J. Phys. Chem. Lett.*, 2016, **7**, 4285-4290.
26. J. S. Ward, N. A. Kukhta, P. L. dos Santos, D. G. Congrave, A. S. Batsanov, A. P. Monkman and M. R. Bryce, *Chem. Mater.*, 2019, **31**, 6684-6695.
27. N. A. Kukhta, R. Huang, A. S. Batsanov, M. R. Bryce and F. B. Dias, *J. Phys. Chem. C*, 2019, **123**, 26536-26546.
28. F. B. Dias, T. J. Penfold and A. P. Monkman, *Methods Appl. Fluores.*, 2017, **5**, 012001.
29. M. Louis, H. Thomas, M. Gmelch, A. Haft, F. Fries and S. Reineke, *Adv. Mater.*, 2019, **31**, 1807887.
30. G. Oster, N. Geacintov and A. Ullah Khan, *Nature*, 1962, **196**, 1089-1090.
31. S. Reineke and M. A. Baldo, *Sci. Rep.*, 2014, **4**, 3797.
32. C. Lee, W. Yang and R. G. Parr, *Phys. Rev. B*, 1988, **37**, 785-789.
33. B. Miehlich, A. Savin, H. Stoll and H. Preuss, *Chem. Phys. Lett.*, 1989, **157**, 200-206.
34. A. D. Becke, *J. Chem. Phys.*, 1993, **98**, 5648-5652.
35. M. J. Frisch, G. W. Trucks, H. B. Schlegel, G. E. Scuseria, M. A. Robb, J. R. Cheeseman, G. Scalmani, V. Barone, G. A. Petersson, H. Nakatsuji, X. Li, M. Caricato, A. V. Marenich, J. Bloino, B. G. Janesko, R. Gomperts, B. Mennucci, H. P. Hratchian, J. V. Ortiz, A. F. Izmaylov, J. L. Sonnenberg, Williams, F. Ding, F. Lipparini, F. Egidi, J. Goings, B. Peng, A. Petrone, T. Henderson, D. Ranasinghe, V. G. Zakrzewski, J. Gao, N. Rega, G. Zheng, W. Liang, M. Hada, M. Ehara, K. Toyota, R. Fukuda, J. Hasegawa, M. Ishida, T. Nakajima, Y. Honda, O. Kitao, H. Nakai, T. Vreven, K. Throssell, J. A. Montgomery Jr., J. E. Peralta, F. Ogliaro, M. J. Bearpark, J. J. Heyd, E. N. Brothers, K. N. Kudin, V. N. Staroverov, T. A. Keith, R. Kobayashi, J. Normand, K. Raghavachari, A. P. Rendell, J. C. Burant, S. S. Iyengar, J. Tomasi, M. Cossi, J. M. Millam, M. Klene, C. Adamo, R. Cammi, J. W. Ochterski, R. L. Martin, K. Morokuma, O. Farkas, J. B. Foresman and D. J. Fox, *Gaussian 16, Revision C.01*, Wallingford, CT, USA, 2016.
36. J. B. F. a. Æ. Frisch, *Exploring Chemistry with Electronic Structure Methods*, Gaussian, Inc., Wallingford, CT, USA, 2015.
37. L. Huang, L. Liu, X. Li, H. Hu, M. Chen, Q. Yang, Z. Ma and X. Jia, *Angew. Chem. Int. Ed.*, 2019, **58**, 16445–16450.
38. H. Li, H. Li, W. Wang, Y. Tao, S. Wang, Q. Yang, Y. Jiang, C. Zheng, W. Huang and R. Chen, *Angew. Chem. Int. Ed.*, 2020, **59**, 4756.
39. Z. An, C. Zheng, Y. Tao, R. Chen, H. Shi, T. Chen, Z. Wang, H. Li, R. Deng, X. Liu and W. Huang, *Nat. Mater.*, 2015, **14**, 685.
40. T. Chen, L. Zheng, J. Yuan, Z. An, R. Chen, Y. Tao, H. Li, X. Xie and W. Huang, *Sci. Rep.*, 2015, **5**, 10923.
41. Bruker APEX2, Bruker AXS Inc., *version 2014.11-0*, Madison, Wisconsin, USA, 2014
42. Bruker SAINT, Bruker AXS Inc., *version V8.34A*, Madison, Wisconsin, USA, 2013.
43. L. J. Farrugia, *J. Appl. Crystallogr.*, 2012, **45**, 849-854.

44. M. C. Burla, R. Caliendo, B. Carrozzini, G. L. Cascarano, C. Cuocci, C. Giacovazzo, M. Mallamo, A. Mazzone and G. Polidori, *J. Appl. Crystallogr.*, 2015, **48**, 306-309.
45. G. M. Sheldrick, *Acta. Crystallogr. A*, 2008, **64**, 112-122.
46. A. L. Spek, *Acta Crystallogr. D Biol. Crystallogr.*, 2009, **65**, 148-155.
47. G. M. Sheldrick, *Acta Crystallogr. C Struct. Chem.*, 2015, **71**, 3-8.
48. Bruker SADABS, *Bruker AXS Inc., version 2014/5*, Madison, Wisconsin, USA, 2014.
49. C. F. Macrae, P. R. Edgington, P. McCabe, E. Pidcock, G. P. Shields, R. Taylor, M. Towler and J. van de Streek, *J. Appl. Crystallogr.*, 2006, **39**, 453-457.
50. A. Forni, E. Lucenti, C. Botta and E. Cariati, *J. Mater. Chem. C*, 2018, **6**, 4603-4626.
51. J. Yang, X. Zhen, B. Wang, X. Gao, Z. Ren, J. Wang, Y. Xie, J. Li, Q. Peng, K. Pu and Z. Li, *Nat. Commun.*, 2018, **9**, 840.
52. L. Huang, L. Liu, X. Li, H. Hu, M. Chen, Q. Yang, Z. Ma and X. Jia, *Angew. Chem. Int. Ed.*, 2019, **58**, 16445-16450.
53. H. Tanaka, K. Shizu, H. Nakanotani and C. Adachi, *Chem. Mater.*, 2013, **25**, 3766-3771.
54. M. Kim, S. K. Jeon, S. Hwang, S. Lee, E. Yu and J. Y. Lee, *J. Phys. Chem. C*, 2016, **120**, 2485-2493.
55. Y. Duan, L. Wen, Y. Gao, Y. Wu, L. Zhao, Y. Geng, G. Shan, M. Zhang and Z. Su, *J. Phys. Chem. C*, 2018, **122**, 23091-23101.
56. Y. Kitamoto, T. Namikawa, D. Ikemizu, Y. Miyata, T. Suzuki, H. Kita, T. Sato and S. Oi, *J. Mater. Chem. C*, 2015, **3**, 9122-9130.
57. Y. Kitamoto, T. Namikawa, T. Suzuki, Y. Miyata, H. Kita, T. Sato and S. Oi, *Org. Electron.*, 2016, **34**, 208-217.
58. J. Jin, H. Jiang, Q. Yang, L. Tang, Y. Tao, Y. Li, R. Chen, C. Zheng, Q. Fan, K. Y. Zhang, Q. Zhao and W. Huang, *Nat. Commun.*, 2020, **11**, 842.

## XVI. Characterization: $^1\text{H}$ , $^{13}\text{C}$ NMR and Mass Spectra

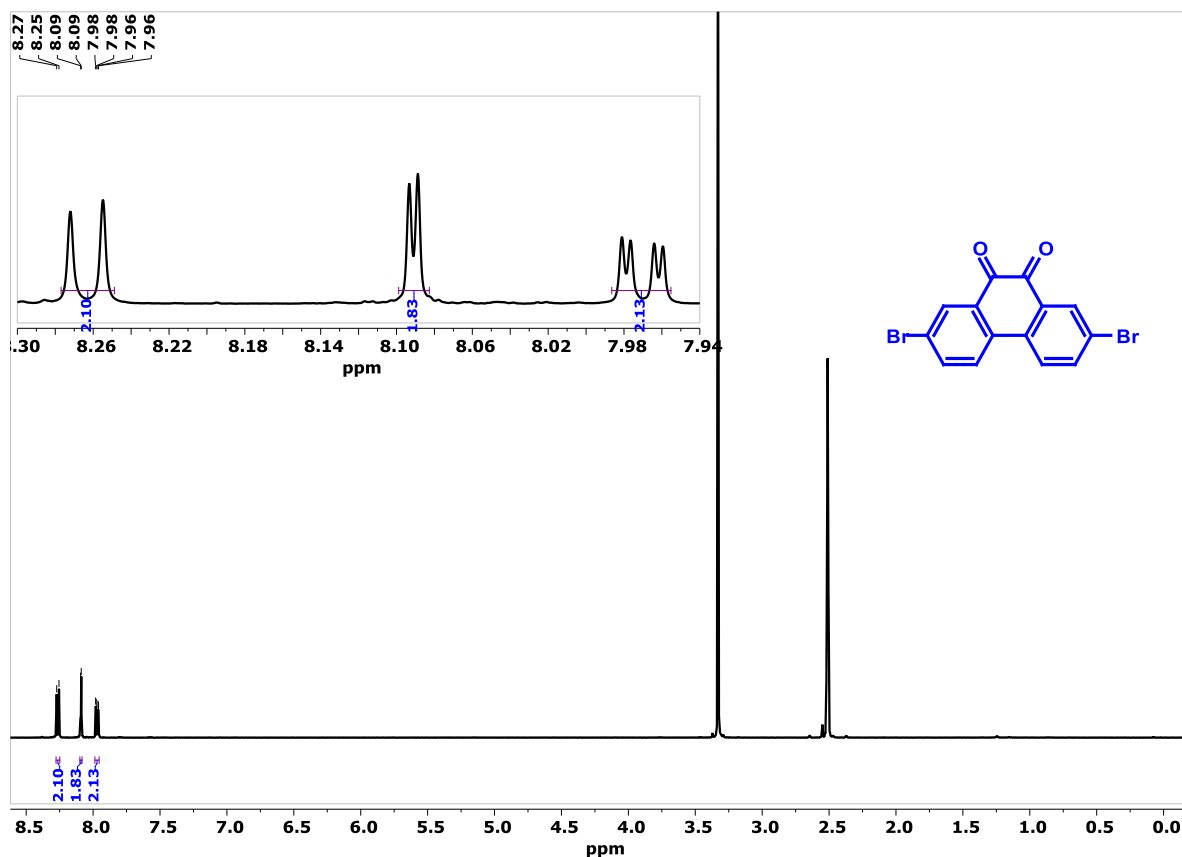


Fig. S48  $^1\text{H}$  NMR spectrum of 2,7-dibromophenanthrene-9,10-quinone (P1) in  $\text{DMSO-d}_6$ .

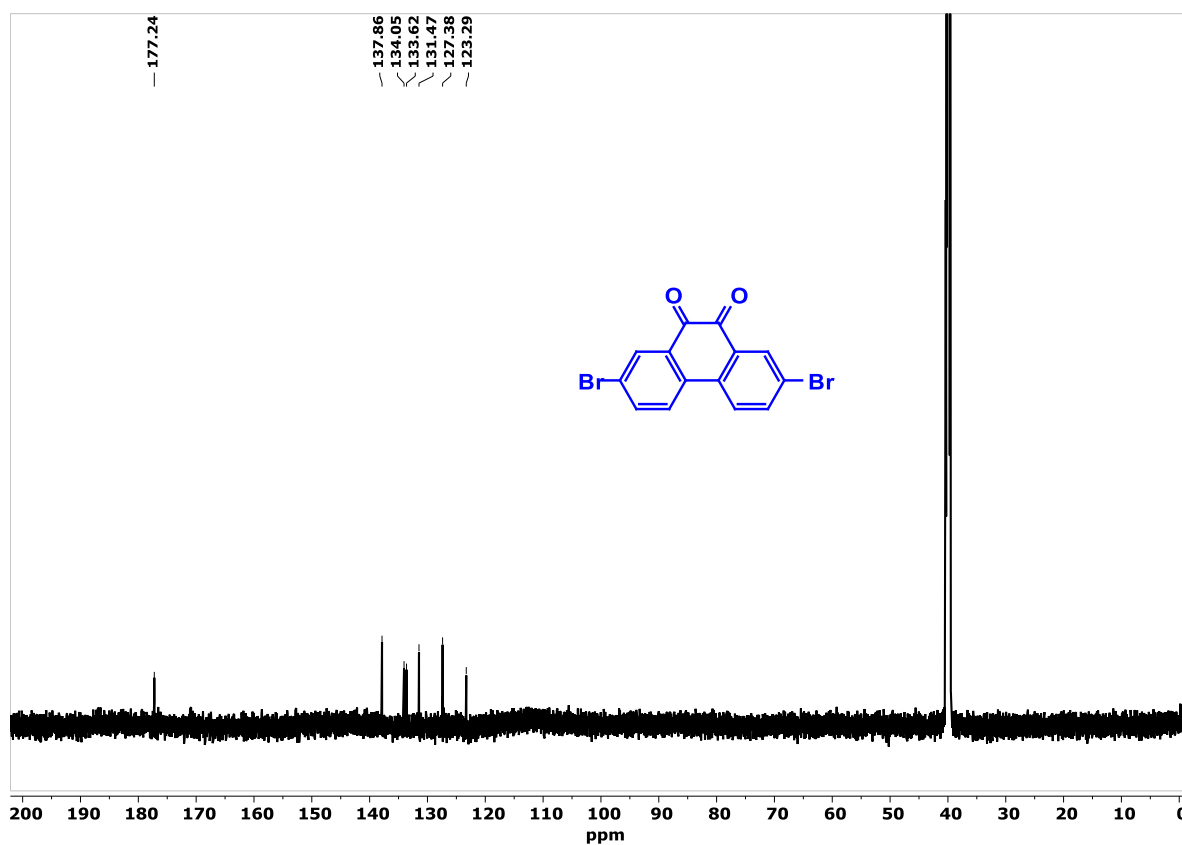


Fig. S49  $^{13}\text{C}$  NMR spectrum of 2,7-dibromophenanthrene-9,10-quinone (P1) in  $\text{DMSO-d}_6$ .

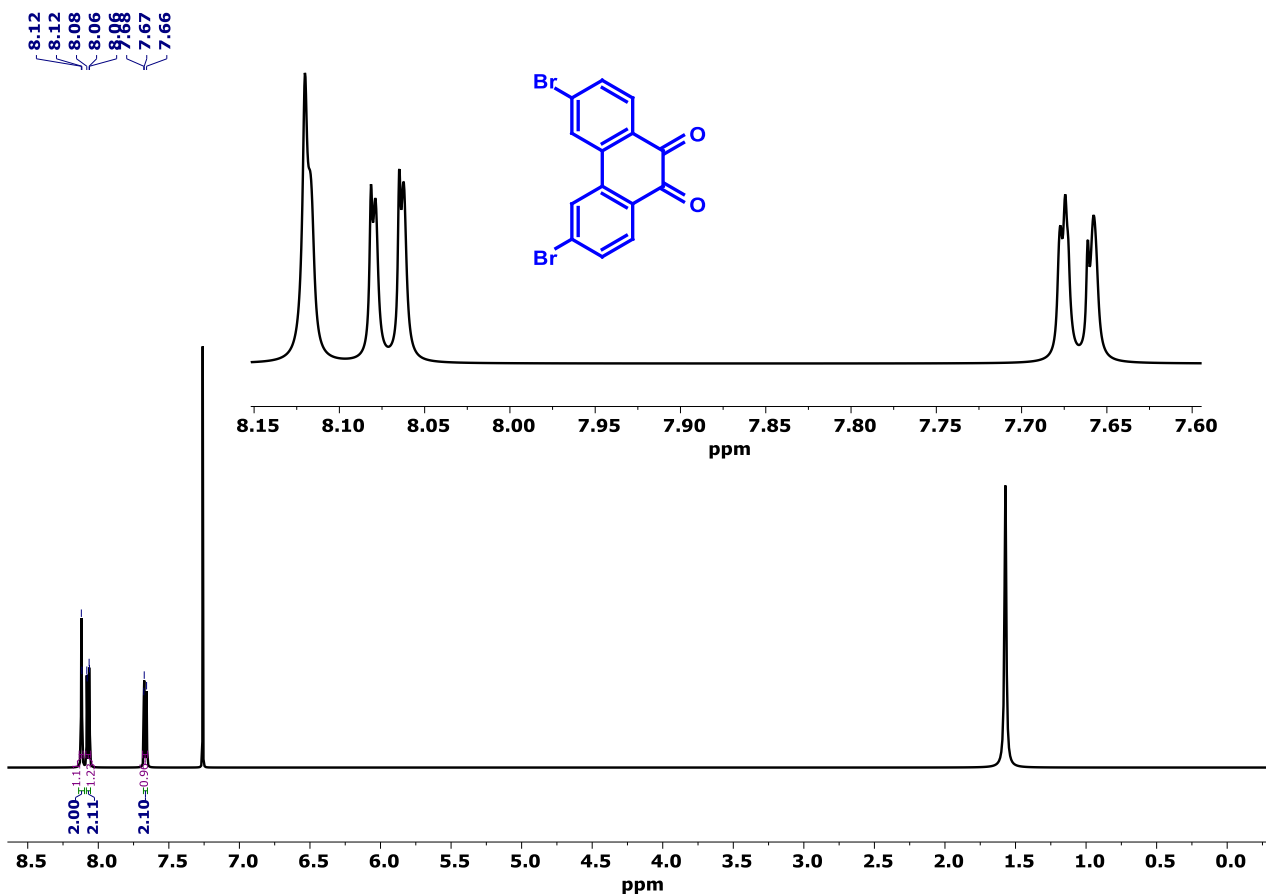


Fig. S50 <sup>1</sup>H NMR spectrum of 3,6-dibromophenanthrene-9,10-quinone (P2) in CDCl<sub>3</sub>.

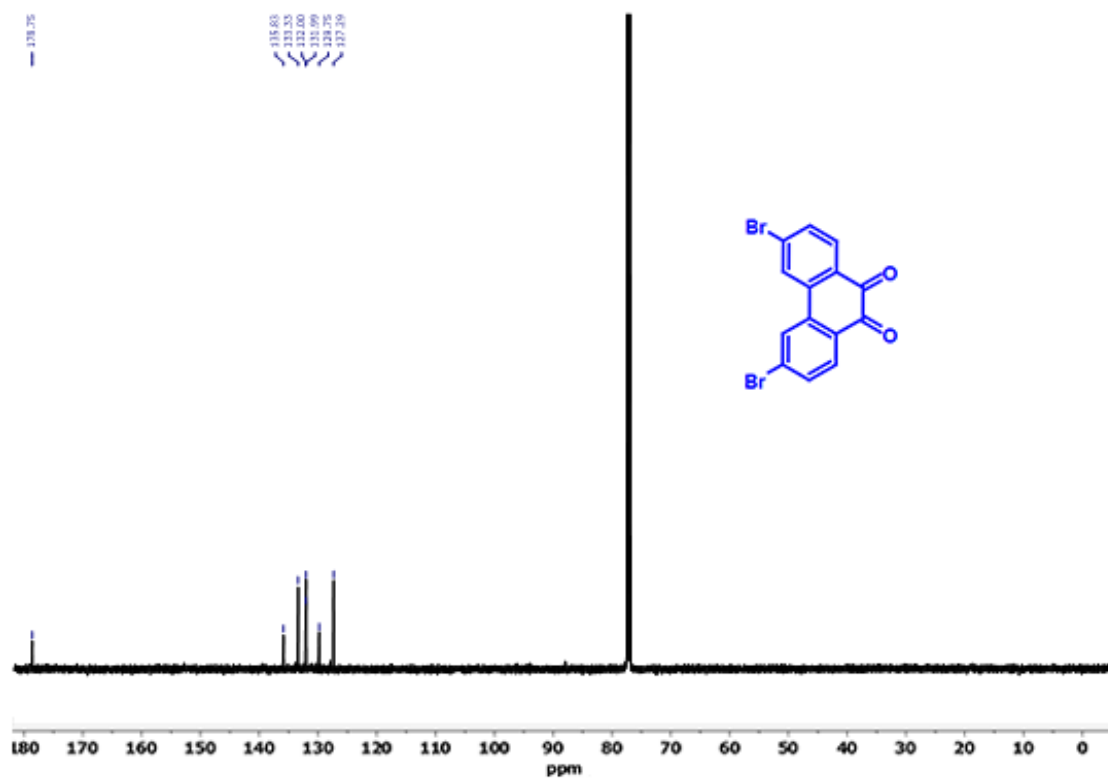


Fig. S51 <sup>13</sup>C NMR spectrum of 3,6-dibromophenanthrene-9,10-quinone (P2) in CDCl<sub>3</sub>.



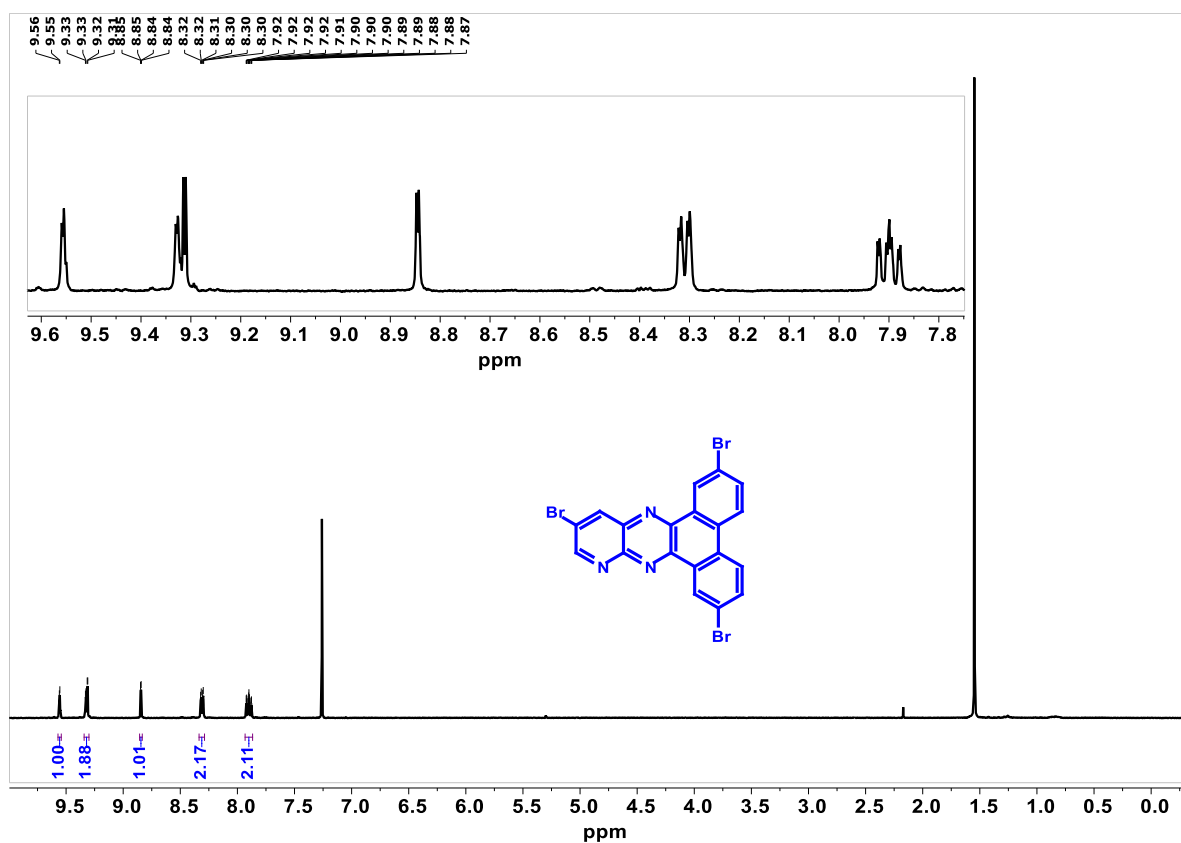


Fig. S52  $^1\text{H}$  NMR spectrum of 2,7,12-tribromodibenzo[*f,h*]pyrido[2,3-*b*]quinoxaline (PQT) in  $\text{CDCl}_3$ .

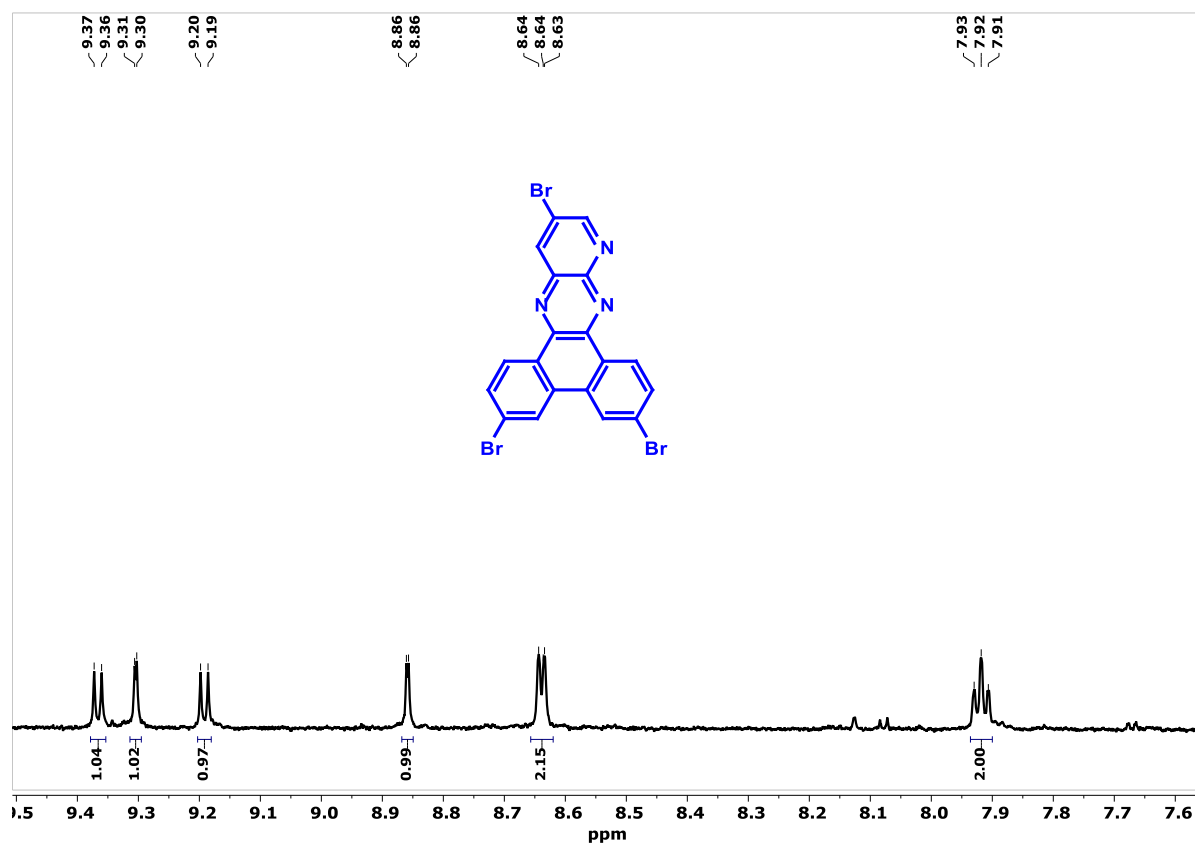


Fig. S53  $^1\text{H}$  NMR spectrum of 3,6,12-tribromodibenzo[*f,h*]pyrido[2,3-*b*]quinoxaline (PQV) in  $\text{CDCl}_3$  (it is challenging to record resolved NMR due to the solubility issue; zoomed view of the aromatic region is shown).

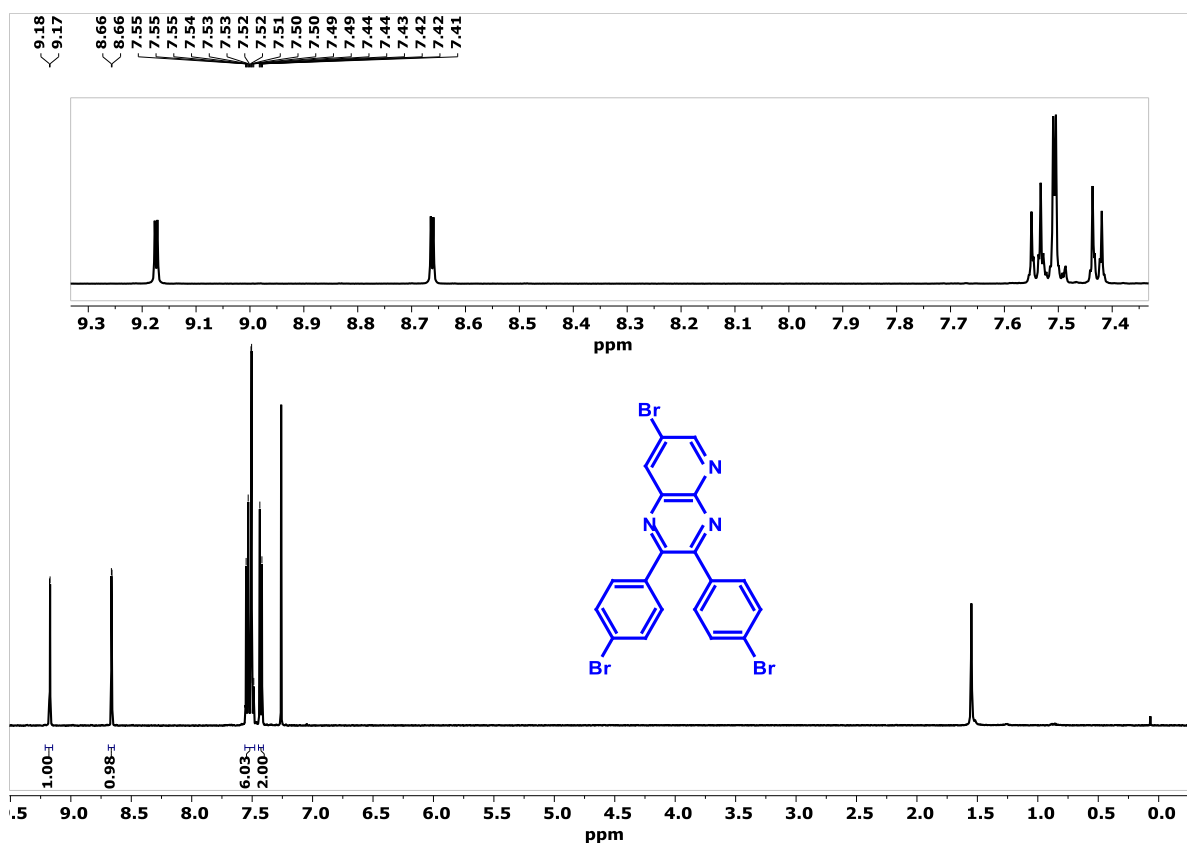


Fig. S54 <sup>1</sup>H NMR spectrum of 7-bromo-2,3-bis(4-bromophenyl)pyrido[2,3-*b*]pyrazine (PZV) in CDCl<sub>3</sub>.

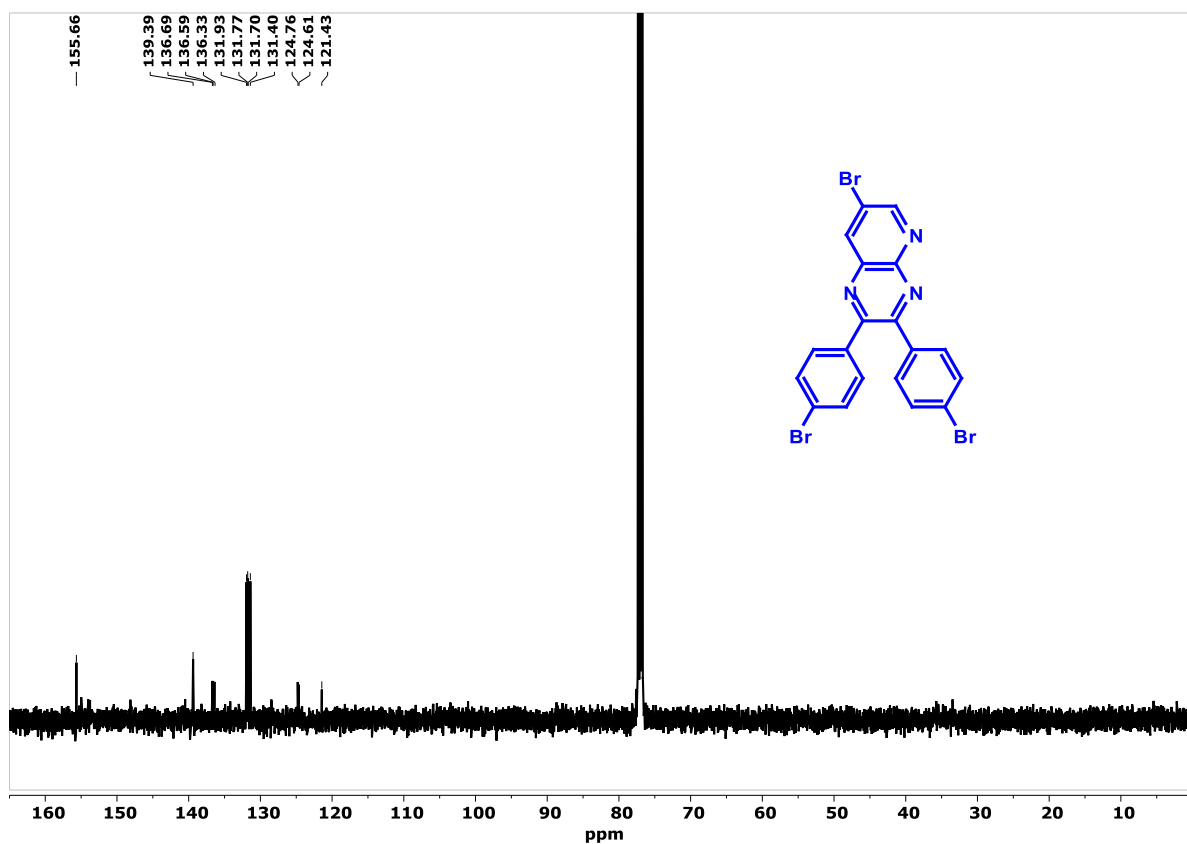
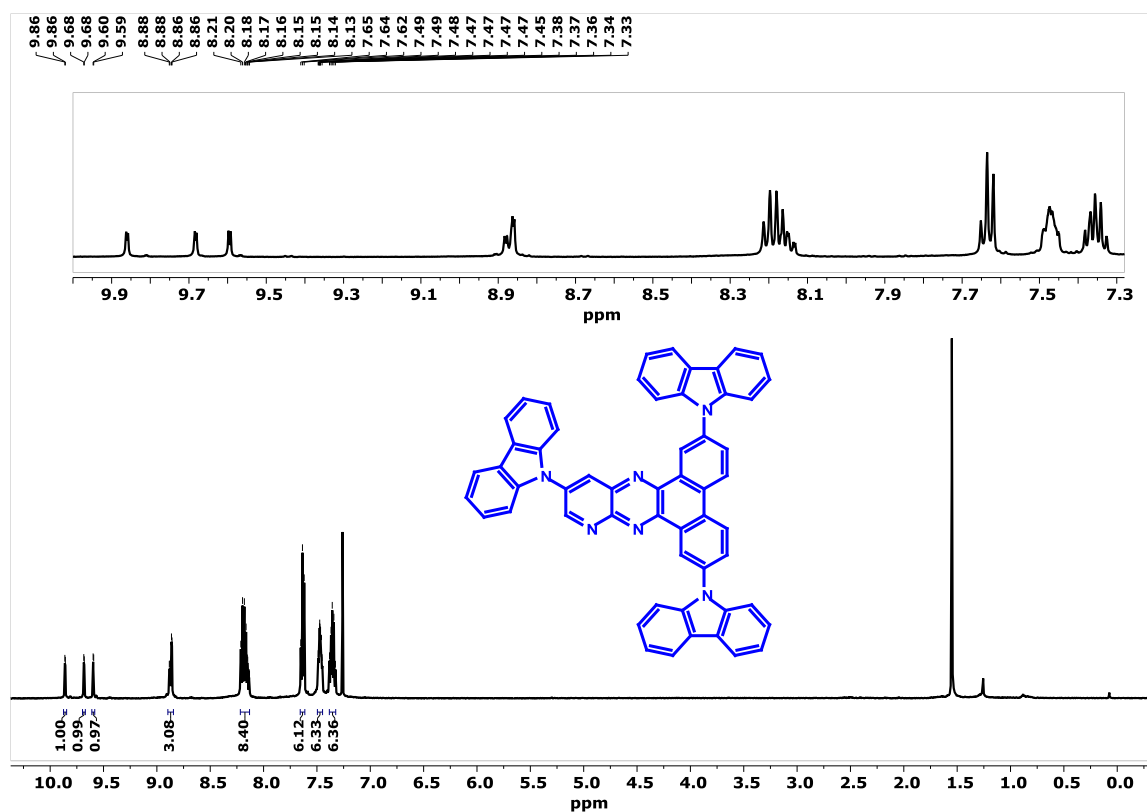
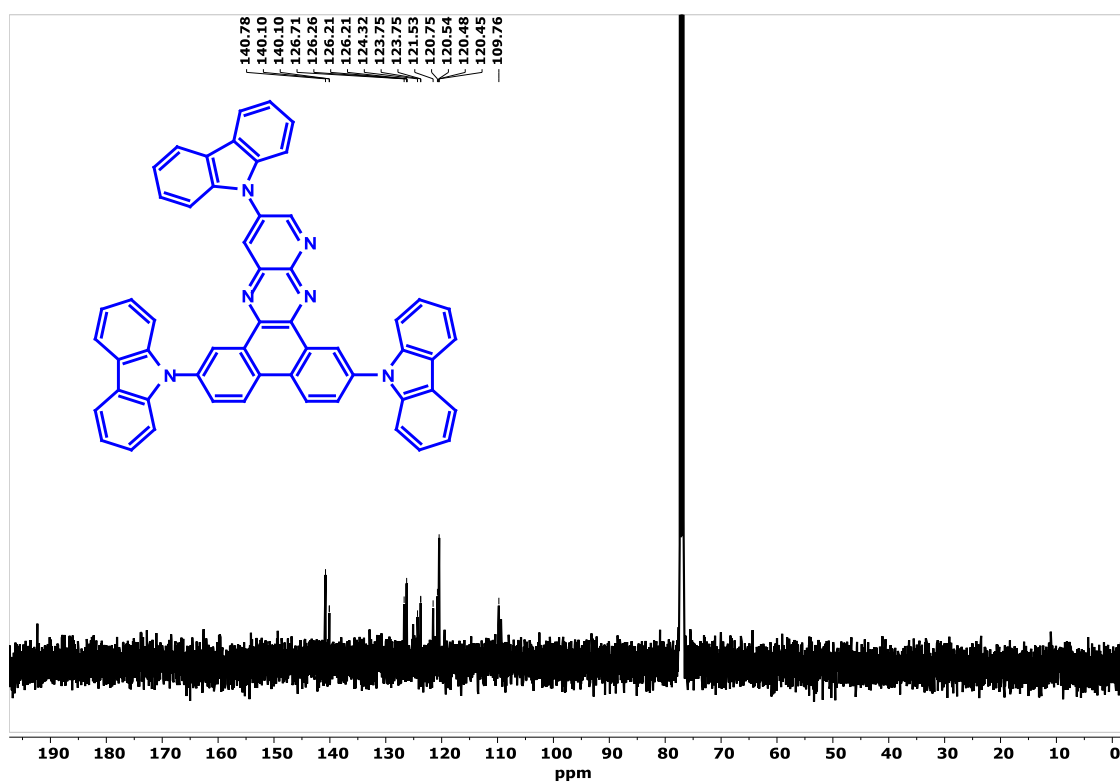


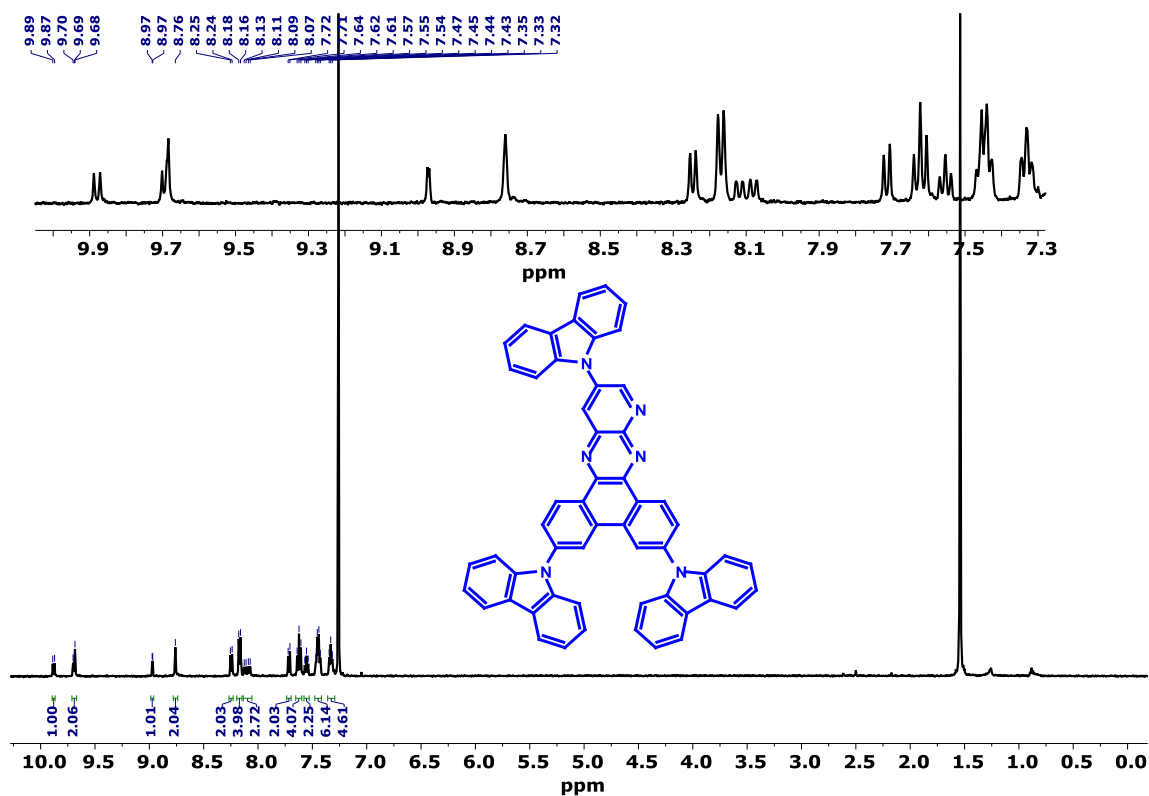
Fig. S55 <sup>13</sup>C NMR spectrum of 7-bromo-2,3-bis(4-bromophenyl)pyrido[2,3-*b*]pyrazine (PZV) in CDCl<sub>3</sub>.



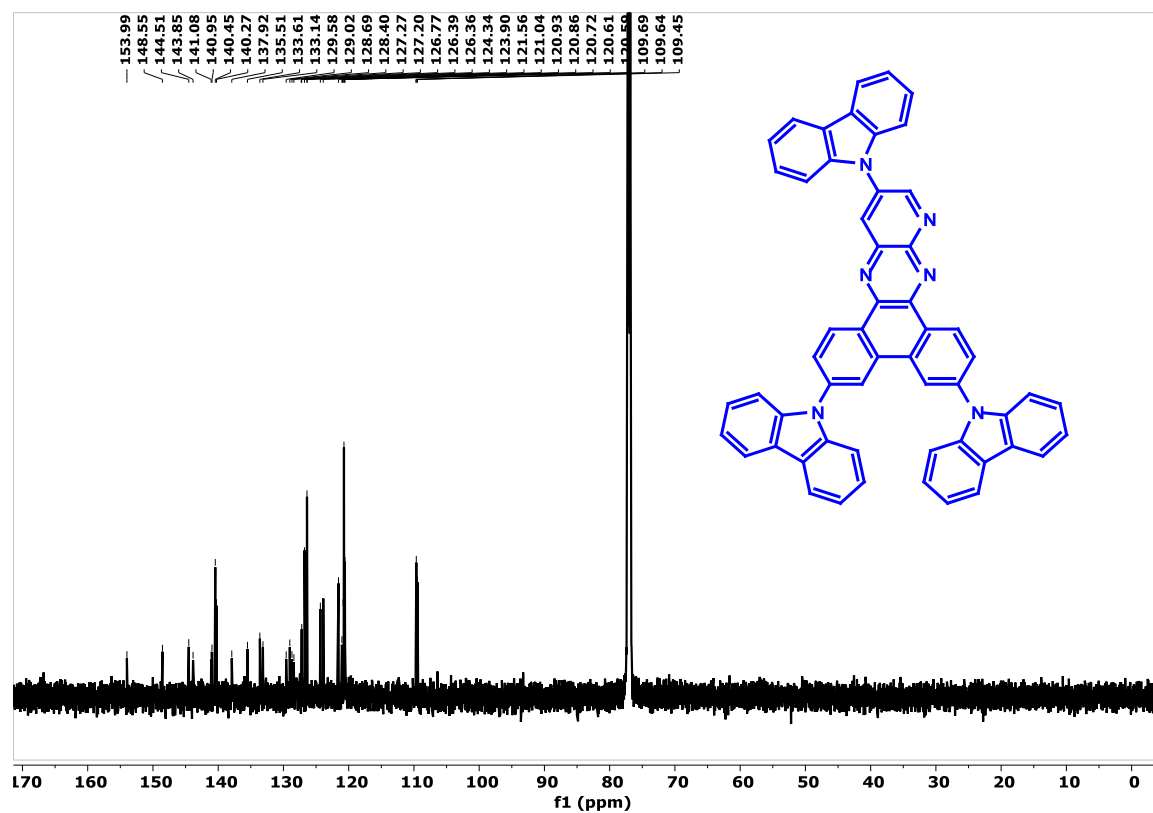
**Fig. S56** <sup>1</sup>H NMR spectrum of 2,7,12-tri(9H-carbazol-9-yl)dibenzo[*f,h*]pyrido[2,3-*b*]quinoxaline (PQTCz) in CDCl<sub>3</sub>.



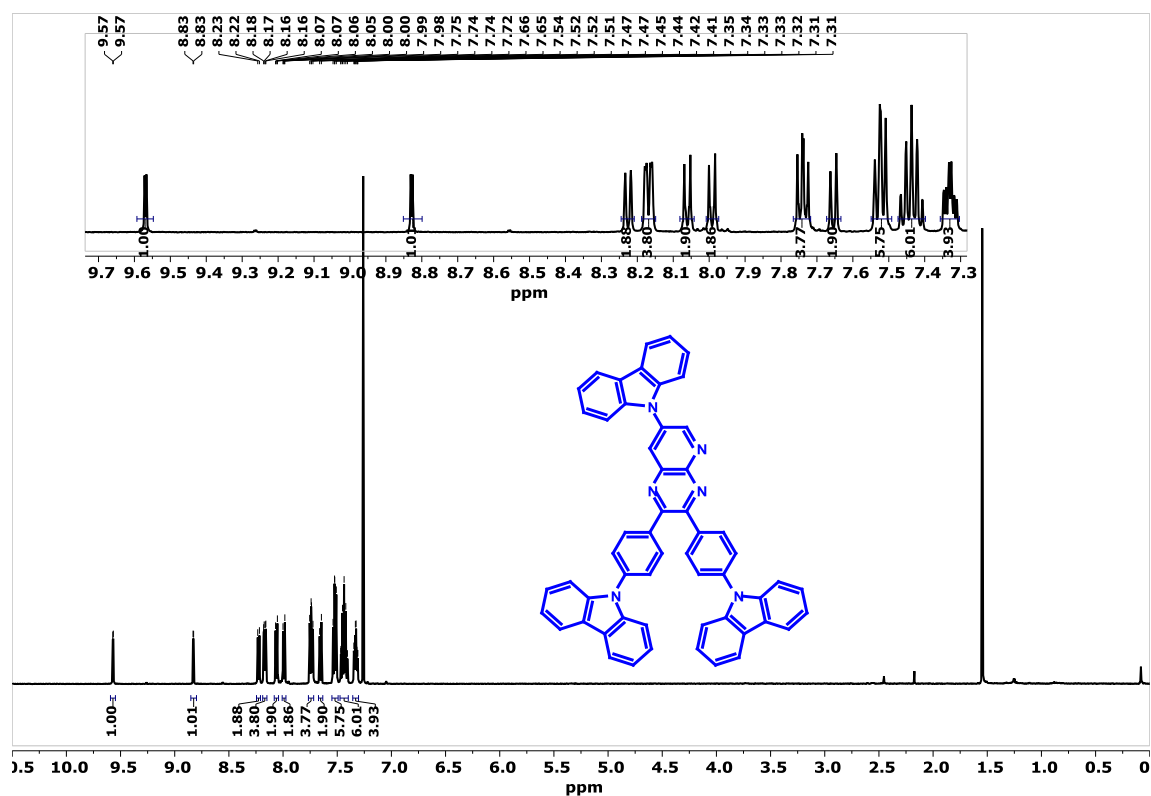
**Fig. S57** <sup>13</sup>C NMR spectrum of 2,7,12-tri(9H-carbazol-9-yl)dibenzo[*f,h*]pyrido[2,3-*b*]quinoxaline (PQTCz) in CDCl<sub>3</sub>.



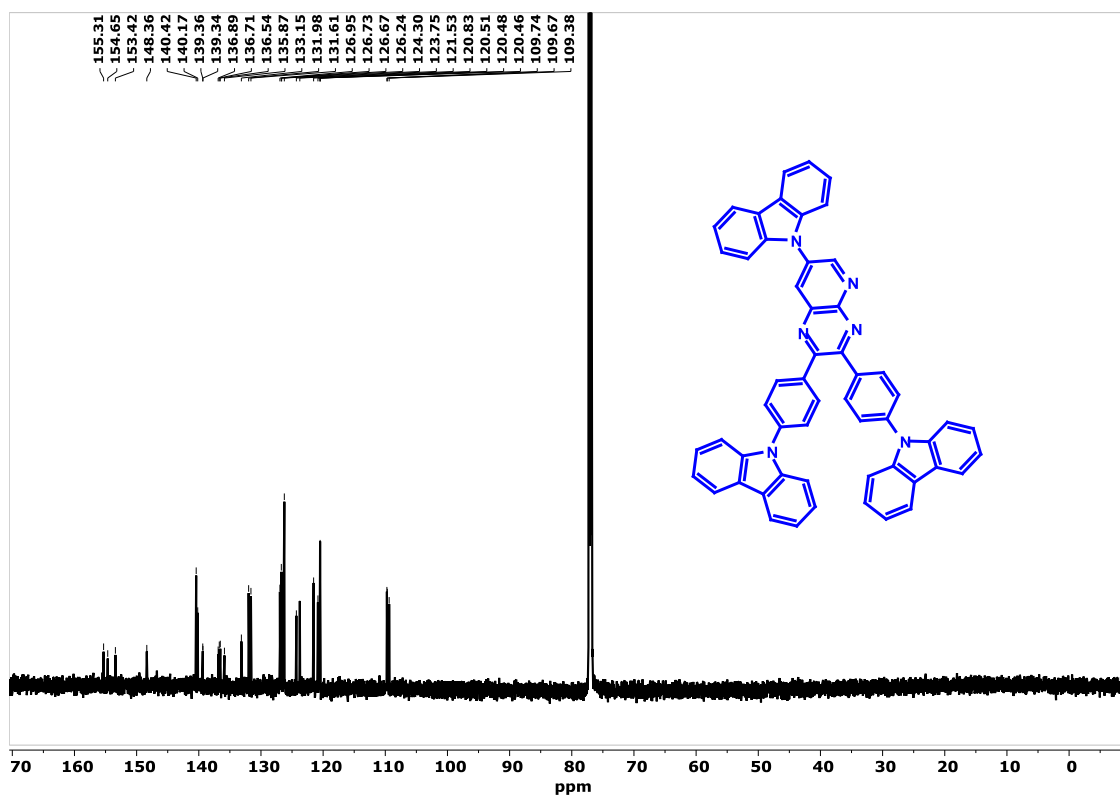
**Fig. S58** <sup>1</sup>H NMR spectrum of 3,6,12-tri(9H-carbazol-9-yl)dibenzo[*f,h*]pyrido[2,3-*b*]quinoxaline (PQVCz) in CDCl<sub>3</sub>.



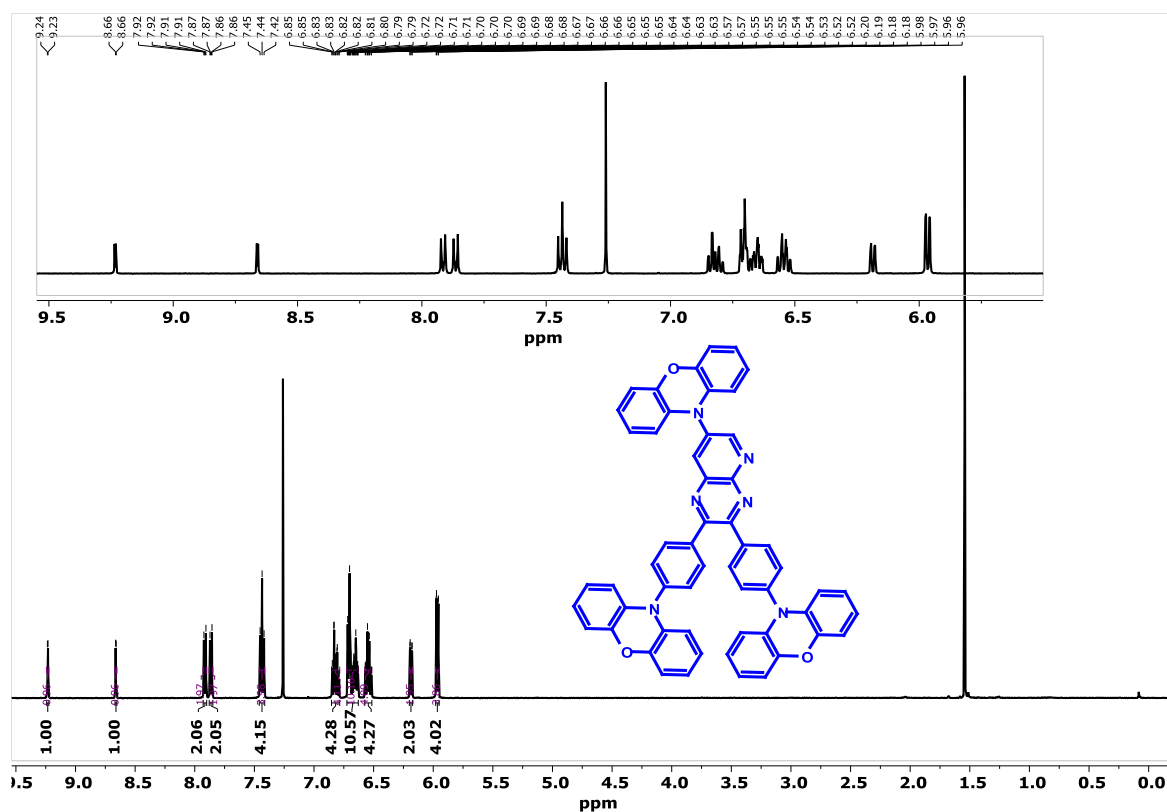
**Fig. S59** <sup>13</sup>C NMR spectrum of 3,6,12-tri(9H-carbazol-9-yl)dibenzo[*f,h*]pyrido[2,3-*b*]quinoxaline (PQVCz) in CDCl<sub>3</sub>.



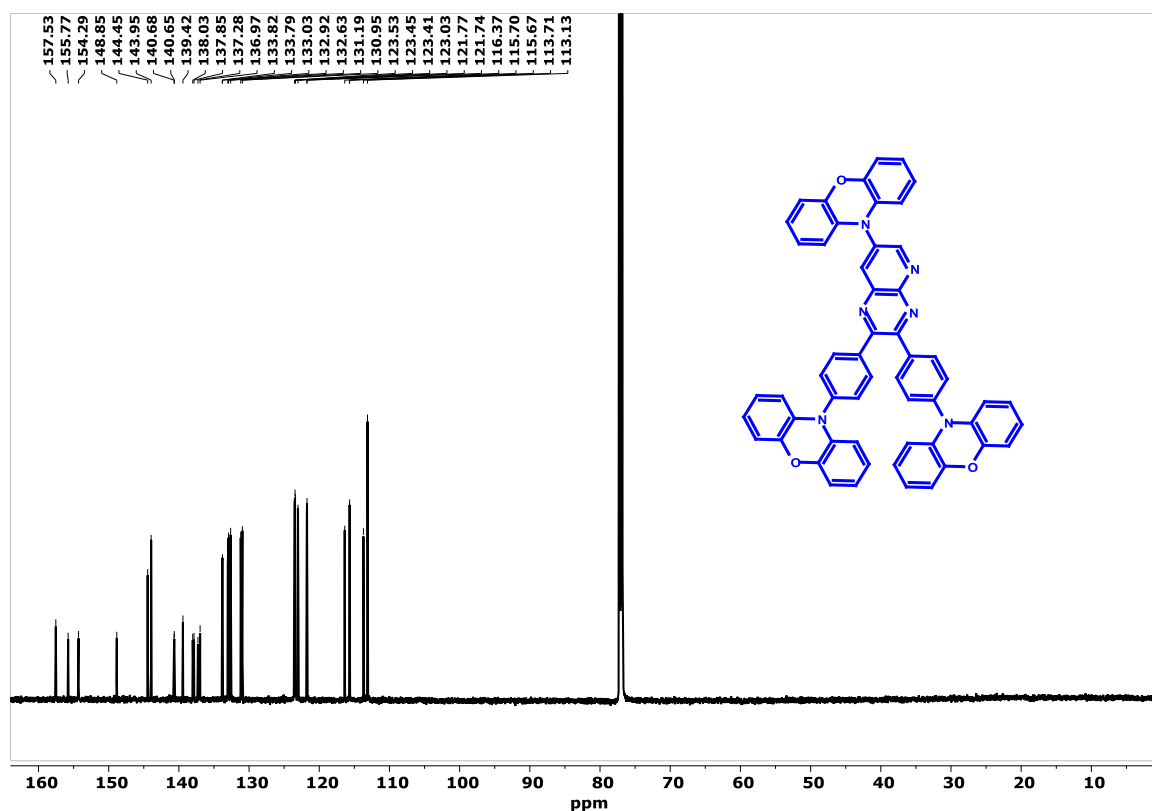
**Fig. S60** <sup>1</sup>H NMR spectrum of 9,9'-((7-(9H-carbazol-9-yl)pyrido[2,3-b]pyrazine-2,3-diyl)bis(4,1-phenylene))bis(9H-carbazole) (PZVCz) in CDCl<sub>3</sub>.



**Fig. S61** <sup>13</sup>C NMR spectrum of 9,9'-((7-(9H-carbazol-9-yl)pyrido[2,3-b]pyrazine-2,3-diyl)bis(4,1-phenylene))bis(9H-carbazole) (PZVCz) in CDCl<sub>3</sub>.



**Fig. S62** <sup>1</sup>H NMR spectrum of 10,10'-((7-(10H-phenoxazin-10-yl)pyrido[2,3-*b*]pyrazine-2,3-diyl)bis(4,1-phenylene))bis(10H-phenoxazine) (PZVPO) in CDCl<sub>3</sub>.



**Fig. S63** <sup>13</sup>C NMR spectrum of 10,10'-((7-(10H-phenoxazin-10-yl)pyrido[2,3-*b*]pyrazine-2,3-diyl)bis(4,1-phenylene))bis(10H-phenoxazine) (PZVPO) in CDCl<sub>3</sub>.

# Display Report

## Analysis Info

Analysis Name D:\Data\NEW USER DATA 2017\2019\FEB\07 feb\Dr.A.Patra-TBR.d  
Method tune\_wide\_APCI\_23.06.m  
Sample Name TBR  
Comment  
Acquisition Date 2/7/2019 3:14:59 PM  
Operator RUCHI  
Instrument micrOTOF-Q II 10330

## Acquisition Parameter

|             |            |                       |           |                  |           |
|-------------|------------|-----------------------|-----------|------------------|-----------|
| Source Type | APCI       | Ion Polarity          | Positive  | Set Nebulizer    | 2.5 Bar   |
| Focus       | Not active | Set Capillary         | 4000 V    | Set Dry Heater   | 200 °C    |
| Scan Begin  | 50 m/z     | Set End Plate Offset  | -500 V    | Set Dry Gas      | 4.0 l/min |
| Scan End    | 3000 m/z   | Set Collision Cell RF | 600.0 Vpp | Set Divert Valve | Waste     |

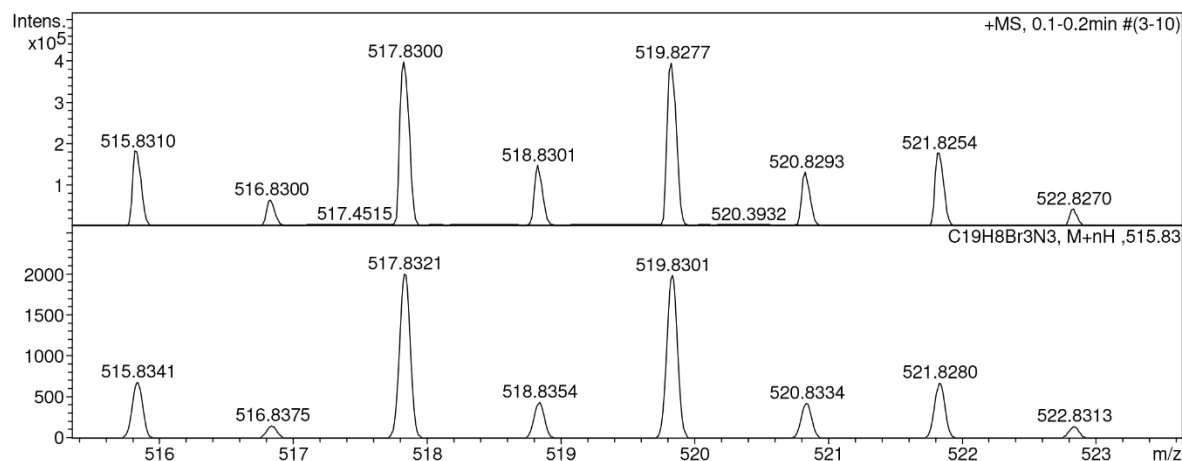
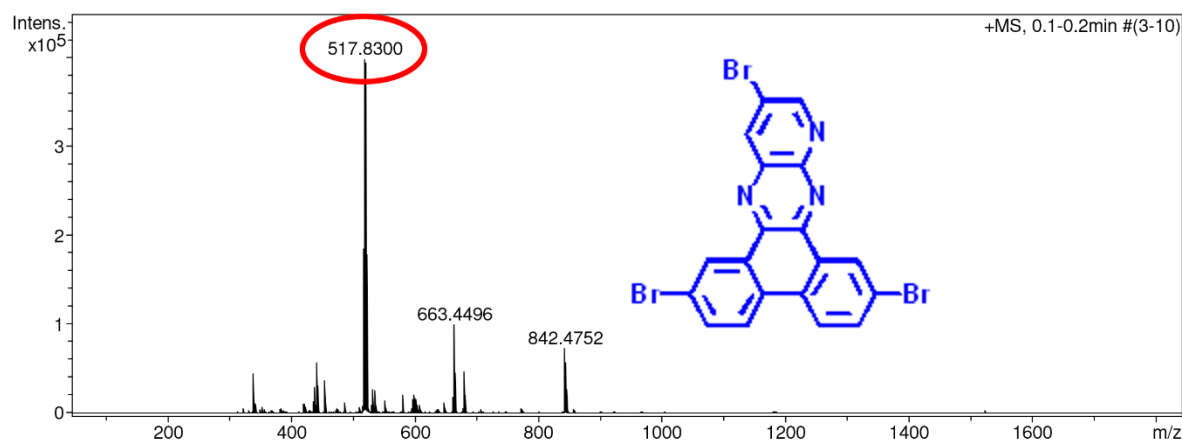
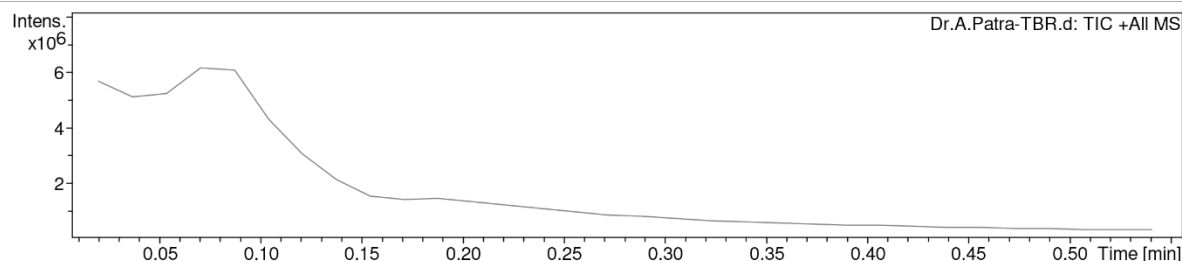


Fig. S64 HRMS (APCI) mass spectrum of PQT.

# Display Report

## Analysis Info

Analysis Name D:\Data\Data\NEW USER DATA 2017-2019-5Dec\Dr.A Patra-BS-PQV-R.d  
Method tune\_wide\_APCI\_23.06.m  
Sample Name BS-PQV-R  
Comment

Acquisition Date 12/5/2019 3:40:24 PM  
Operator RUCHI  
Instrument micrOTOF-Q II 10330

## Acquisition Parameter

|             |            |                       |           |                  |           |
|-------------|------------|-----------------------|-----------|------------------|-----------|
| Source Type | Multi Mode | Ion Polarity          | Positive  | Set Nebulizer    | 2.0 Bar   |
| Focus       | Not active | Set Capillary         | 2500 V    | Set Dry Heater   | 200 °C    |
| Scan Begin  | 50 m/z     | Set End Plate Offset  | -500 V    | Set Dry Gas      | 5.0 l/min |
| Scan End    | 3000 m/z   | Set Collision Cell RF | 300.0 Vpp | Set Divert Valve | Waste     |

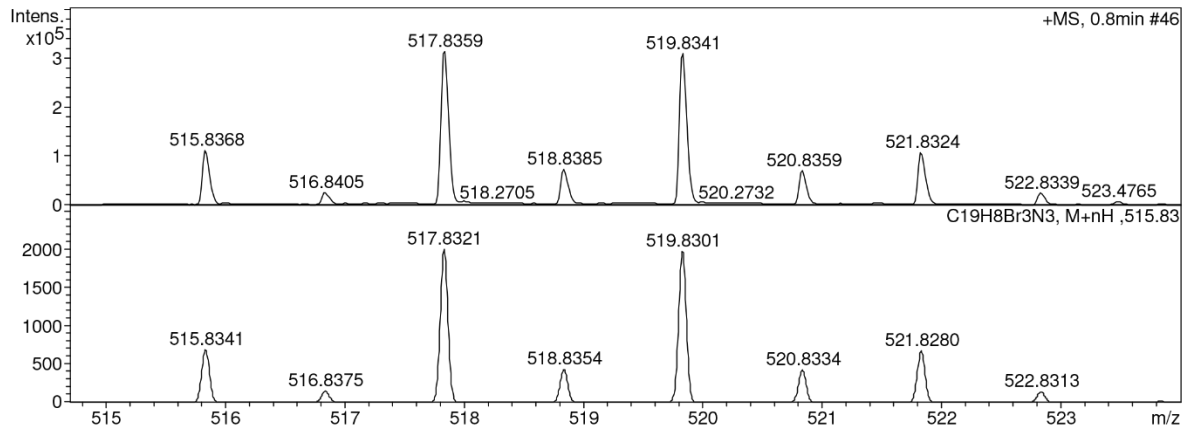
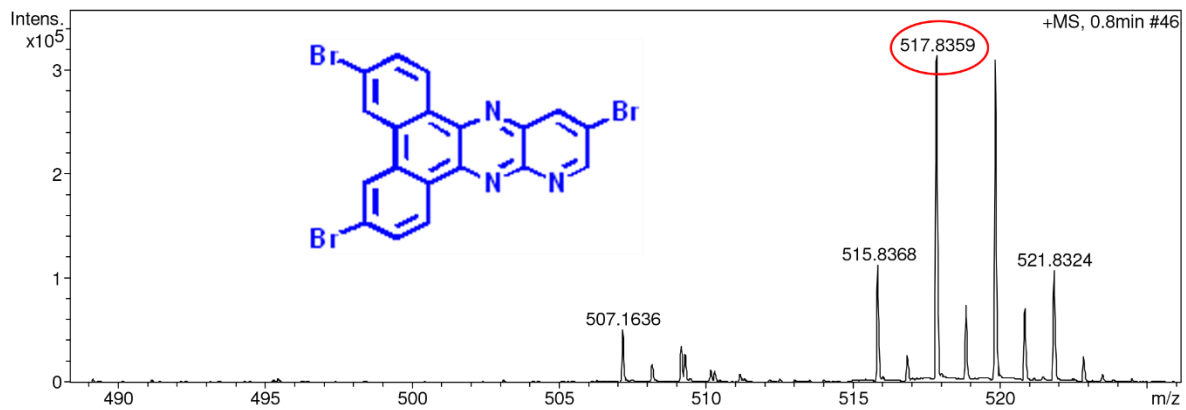
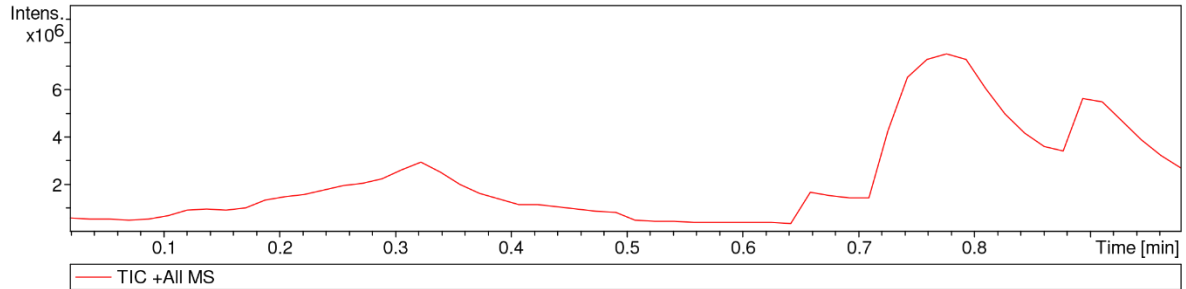


Fig. S65 HRMS (APCI) mass spectrum of PQV.



# Display Report

## Analysis Info

Analysis Name D:\Data\NEW USER DATA 2017\2019\FEB\07 feb\Dr.A.Patra-BPPZ.d  
Method tune\_wide\_APCI\_23.06.m  
Sample Name BPPZ  
Comment

Acquisition Date 2/7/2019 3:16:29 PM  
Operator RUCHI  
Instrument micrOTOF-Q II 10330

## Acquisition Parameter

|             |            |                       |           |                  |           |
|-------------|------------|-----------------------|-----------|------------------|-----------|
| Source Type | APCI       | Ion Polarity          | Positive  | Set Nebulizer    | 2.5 Bar   |
| Focus       | Not active | Set Capillary         | 4000 V    | Set Dry Heater   | 200 °C    |
| Scan Begin  | 50 m/z     | Set End Plate Offset  | -500 V    | Set Dry Gas      | 4.0 l/min |
| Scan End    | 3000 m/z   | Set Collision Cell RF | 600.0 Vpp | Set Divert Valve | Waste     |

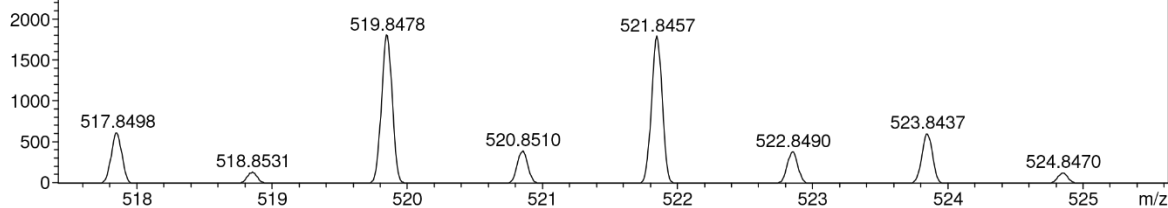
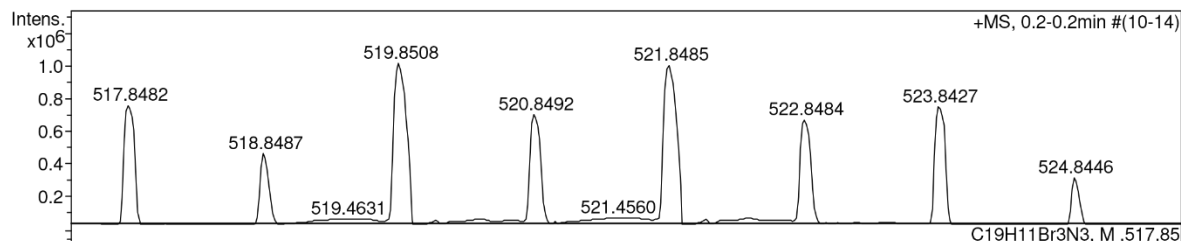
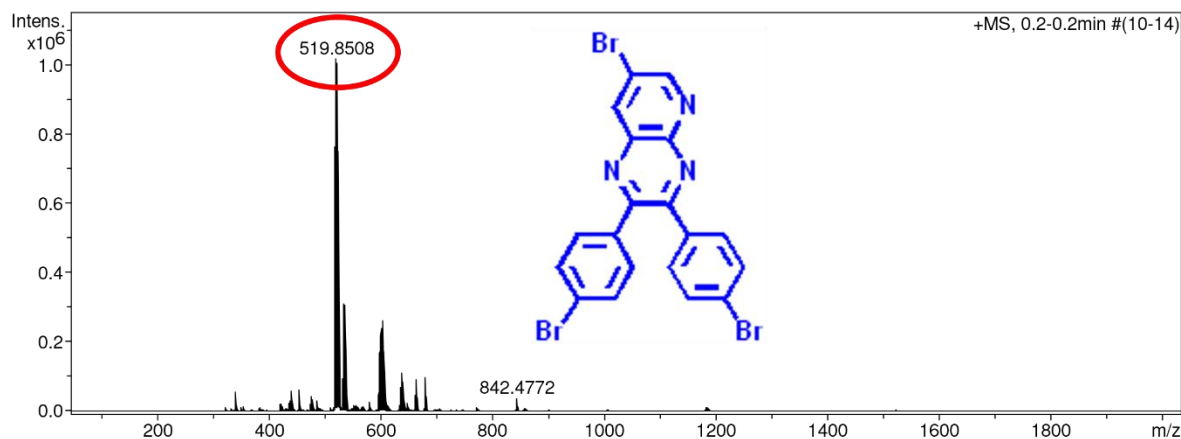
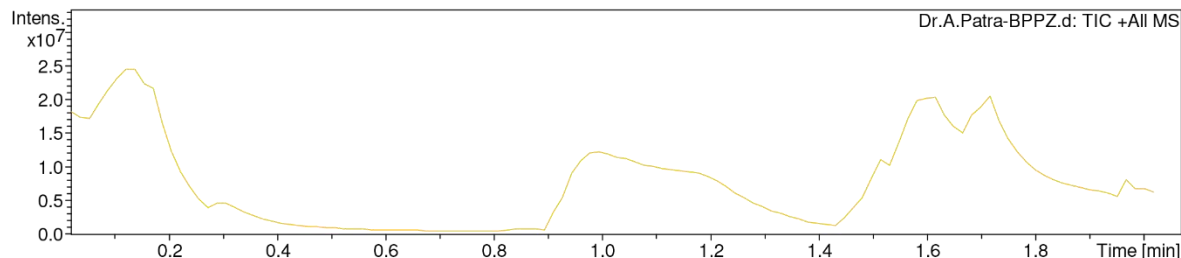


Fig. S66 HRMS (APCI) mass spectrum of PZV.

# Display Report

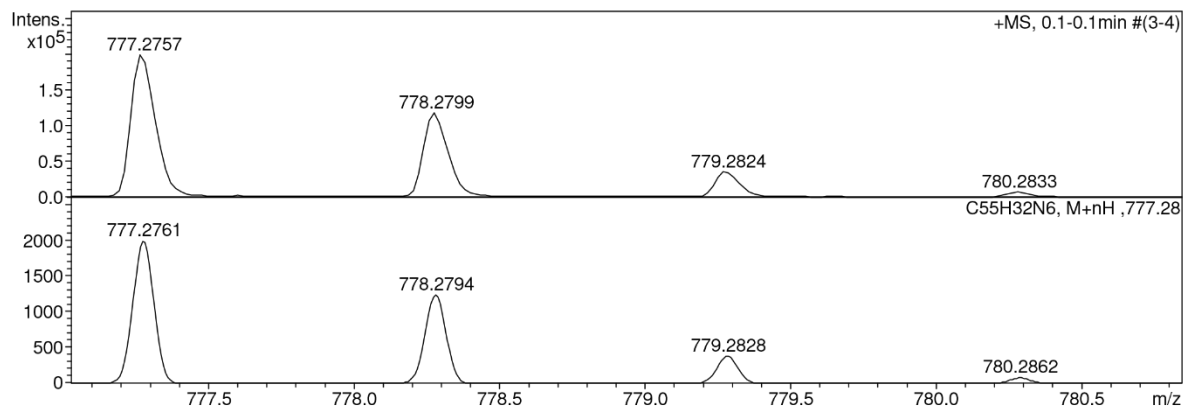
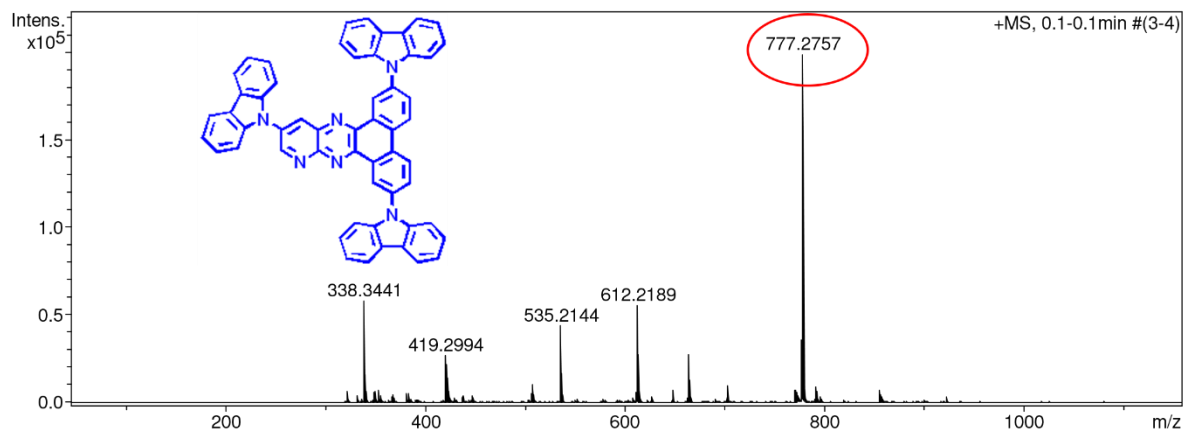
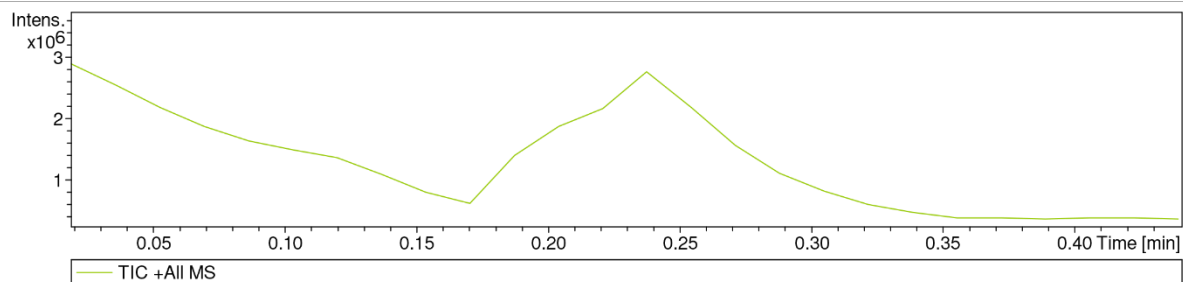
## Analysis Info

Analysis Name D:\Data\NEW USER DATA 2017\2018\NOVEMBER\8\Dr.A.Patra-AP-SS-TBRCZ-1.d  
Method tune\_wide\_APCI\_23.06.m  
Sample Name AP-SS-TBRCZ-1  
Comment

Acquisition Date 11/8/2018 3:02:39 PM  
Operator RUCHI  
Instrument micrOTOF-Q II 10330

## Acquisition Parameter

|             |            |                       |           |                  |           |
|-------------|------------|-----------------------|-----------|------------------|-----------|
| Source Type | APCI       | Ion Polarity          | Positive  | Set Nebulizer    | 2.5 Bar   |
| Focus       | Not active | Set Capillary         | 4000 V    | Set Dry Heater   | 200 °C    |
| Scan Begin  | 50 m/z     | Set End Plate Offset  | -500 V    | Set Dry Gas      | 4.0 l/min |
| Scan End    | 3000 m/z   | Set Collision Cell RF | 600.0 Vpp | Set Divert Valve | Waste     |



**Fig. S67** HRMS (APCI) mass spectrum of PQTcZ.

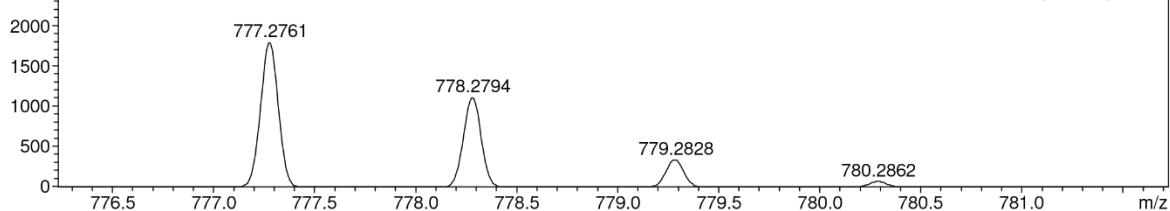
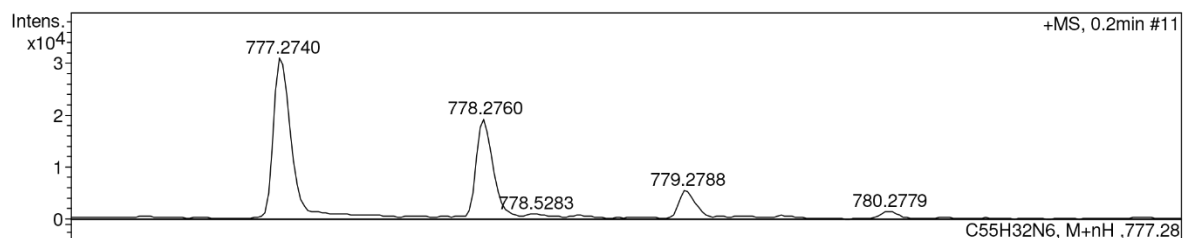
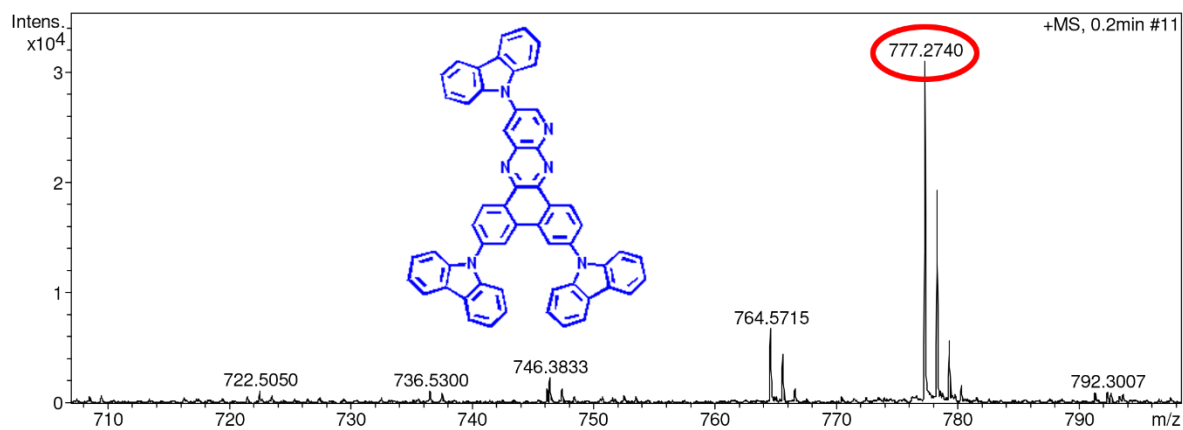
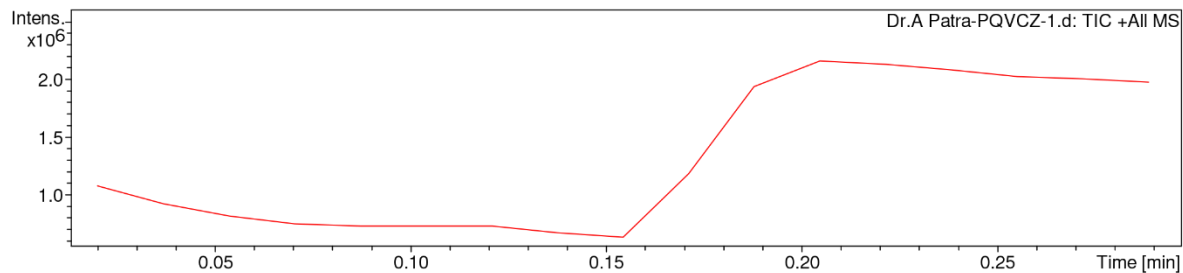
# Display Report

## Analysis Info

Analysis Name D:\Data\NEW USER DATA 2017\2019\Oct\10 OCT\Dr.A Patra-PQVCZ-1.d Acquisition Date 10/10/2019 3:48:13 PM  
Method tune\_wide\_APCI\_23.06.m Operator RUCHI  
Sample Name PQVCZ-1 Instrument micrOTOF-Q II 10330  
Comment

## Acquisition Parameter

|             |            |                       |           |                  |           |
|-------------|------------|-----------------------|-----------|------------------|-----------|
| Source Type | Multi Mode | Ion Polarity          | Positive  | Set Nebulizer    | 2.0 Bar   |
| Focus       | Not active | Set Capillary         | 2500 V    | Set Dry Heater   | 200 °C    |
| Scan Begin  | 50 m/z     | Set End Plate Offset  | -500 V    | Set Dry Gas      | 5.0 l/min |
| Scan End    | 3000 m/z   | Set Collision Cell RF | 600.0 Vpp | Set Divert Valve | Waste     |



**Fig. S68** HRMS (APCI) mass spectrum of PQVCz.

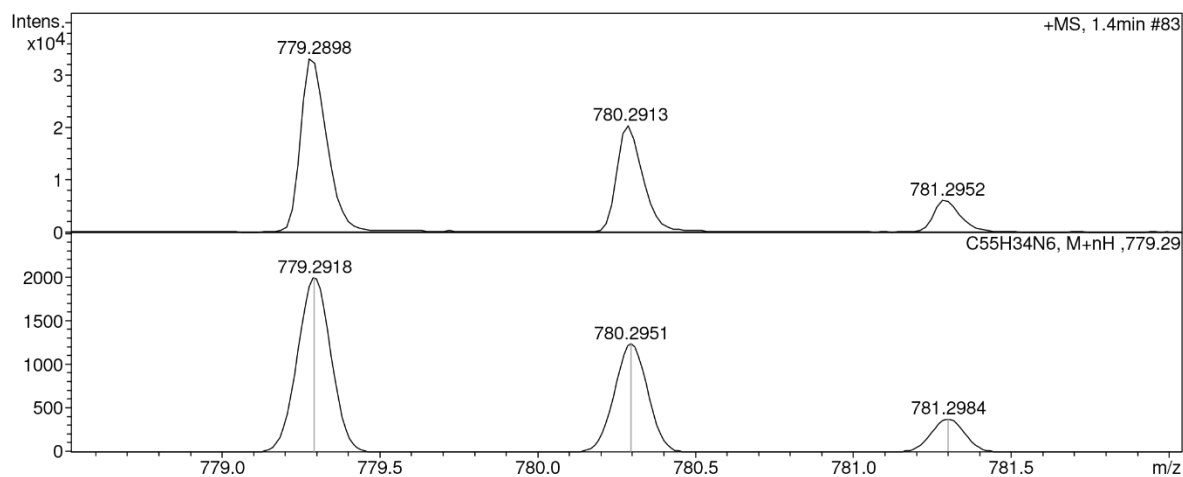
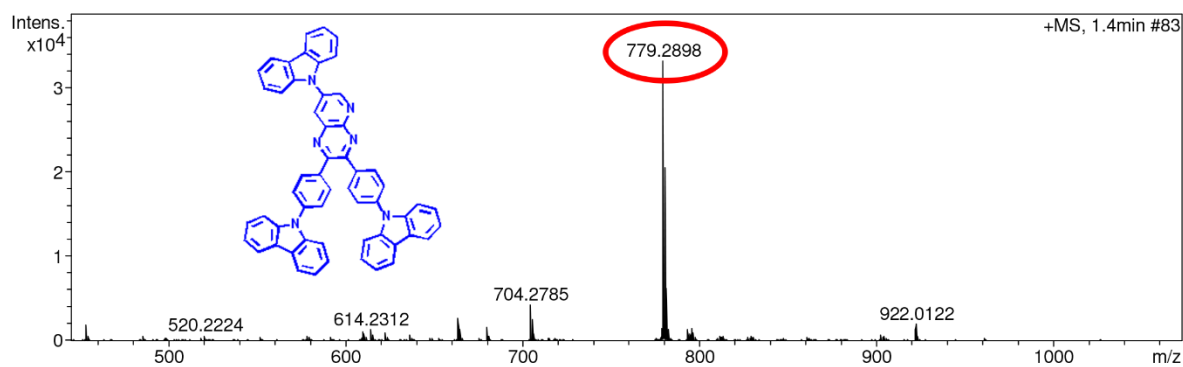
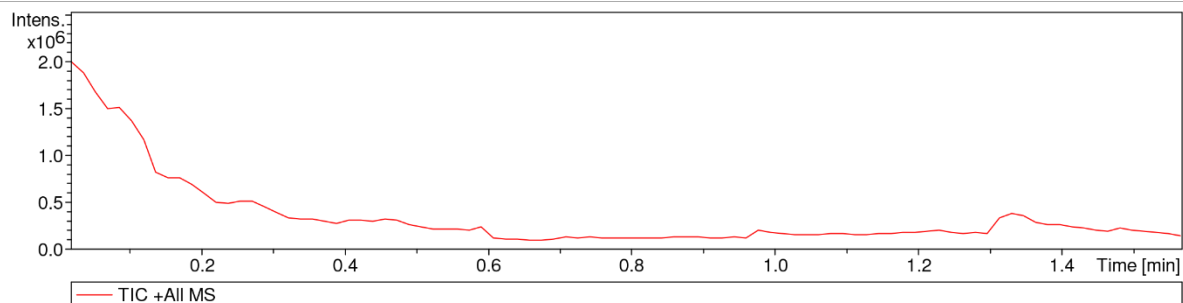
# Display Report

## Analysis Info

Analysis Name D:\Data\NEW USER DATA 2017\2019\APR\16A\Dr. A Patra-BS-PzTCz-2.d Acquisition Date 4/18/2019 11:06:14 AM  
Method tune\_wide\_APCI\_23.06.m Operator RUCHI  
Sample Name BS-PzTCz-2 Instrument micrOTOF-Q II 10330  
Comment

## Acquisition Parameter

|             |            |                       |           |                  |           |
|-------------|------------|-----------------------|-----------|------------------|-----------|
| Source Type | APCI       | Ion Polarity          | Positive  | Set Nebulizer    | 0.4 Bar   |
| Focus       | Not active | Set Capillary         | 4000 V    | Set Dry Heater   | 200 °C    |
| Scan Begin  | 50 m/z     | Set End Plate Offset  | -500 V    | Set Dry Gas      | 4.0 l/min |
| Scan End    | 3000 m/z   | Set Collision Cell RF | 600.0 Vpp | Set Divert Valve | Waste     |



**Fig. S69** HRMS (APCI) mass spectrum of PZVCz.

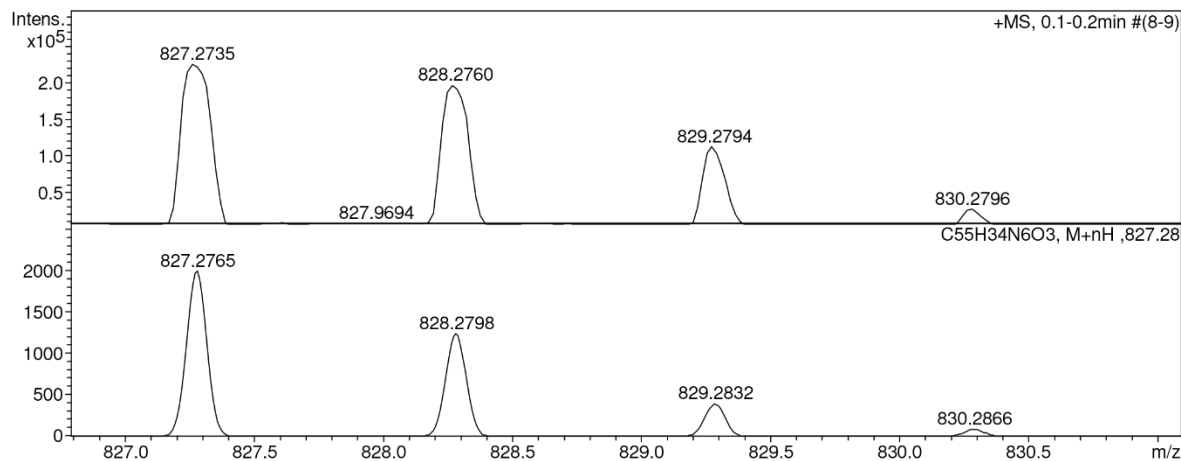
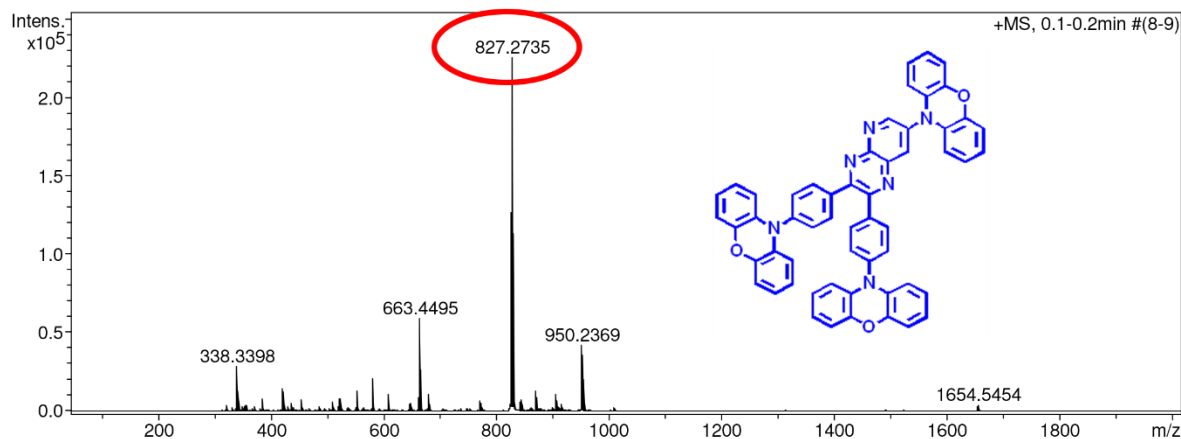
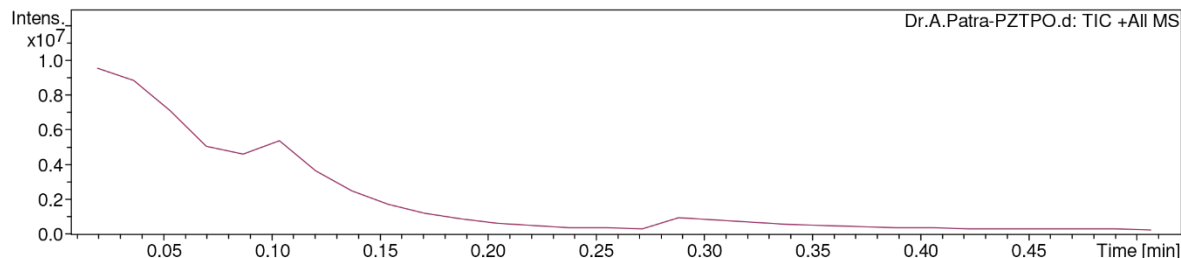
# Display Report

## Analysis Info

Analysis Name D:\Data\NEW USER DATA 2017\2019\FEB\07 feb\Dr.A.Patra-PZTPO.d Acquisition Date 2/7/2019 3:31:03 PM  
Method tune\_wide\_APCI\_23.06.m Operator RUCHI  
Sample Name PZTPO Instrument micrOTOF-Q II 10330  
Comment

## Acquisition Parameter

|             |            |                       |           |                  |           |
|-------------|------------|-----------------------|-----------|------------------|-----------|
| Source Type | APCI       | Ion Polarity          | Positive  | Set Nebulizer    | 2.5 Bar   |
| Focus       | Not active | Set Capillary         | 4000 V    | Set Dry Heater   | 200 °C    |
| Scan Begin  | 50 m/z     | Set End Plate Offset  | -500 V    | Set Dry Gas      | 4.0 l/min |
| Scan End    | 3000 m/z   | Set Collision Cell RF | 600.0 Vpp | Set Divert Valve | Waste     |



**Fig. S70** HRMS (APCI) mass spectrum of PZVPO.